Politecnico di Torino

POLYTECHNIC OF TURIN

MASTER THESIS IN MECHANICAL ENGINEERING

A.Y. 2022/2023
Graduation Session December 2023

Vertical displacements and MHD marginal stability in fusion tokamak plasmas

Author:
Gabriele TADDEI

Supervisor:
Francesco PORCELLI

"It must be splendid to command millions of people in great national ventures, to lead a hundred thousand to victory in battle. But it seems to me greater still to discover fundamental truths in a very modest room with very modest means - truths that will still be foundations of human knowledge when the memory of these battles is painstakingly preserved only in the archives of the historian."

Ludwig Boltzmann

POLYTECHNIC OF TURIN

Abstract

Mechanical Engineering
(DIMEAS) Department of Mechanical and Aerospace Engineering

MSc in Mechanical Engineering

Vertical displacements and MHD marginal stability in fusion tokamak plasmas

by Gabriele TADDEI

This vertical stability analysis is carried out on a tokamak plasma for nuclear fusion, where plasma is confined through magnetic flux surfaces that are analytically described as constant u surfaces. The first magnetic surface where plasma is contained is the elliptical surface $u = u_b$, which is then surrounded by a vacuum region, where a magnetic separatrix, $u = u_X$, is present. This latter is a magnetic flux surface with two magnetic X-points produced by additional external currents (divertor tokamak configuration), that also cause a vertical elongation of the confined plasma. Everything is then confined inside a toroidal containment chamber, that in our case study will be assumed to stand sufficiently far away from the plasma's boundary, so that it does not interfere with plasma stability.
Work [paper citation] analyzed vertical stability for the elongated confined plasma with an ideal-MHD model, where perturbations are guided by a current sheet forming on the plasma's boundary and grow with very fast time-scales. An unstable behavior for plasma localized inside the first magnetic surface, $u = u_b$, is found, where perturbation grows in time as $e^{\gamma t}$, γ as the growth rate. When plasma is instead extended up to the magnetic separatrix, the effect of the current sheet at the plasma's boundary changes from destabilizing to stabilizing. This transition in plasma's stability leads us to search a flux surface $u = u_{marg}$, where marginal stability occurs. The solution to our problem is carried out through the ideal-MHD energy principle. The stability problem is reduced to the solution of an eigenvalue problem, where γ^2 is the eigenvalue to be found and its sign determines whether our system is stable or not. Since γ^2 is a real number, consequently a positive value determines an unstable behavior of the system, whereas if negative, γ becomes purely imaginary with null real part, therefore producing stability with an oscillatory behavior in time. The problem of finding the marginal stability surface is thus reduced to search the flux surface $u = u_{marg}$ for which γ^2 is zero.
The normal mode formulation, that has been used for the problem, can be used to define the correlation between the eigenvalue γ^2 and the perturbed potential energy δW, as $\gamma^2 = \delta W(\tilde{\psi}*, \tilde{\psi})/K(\tilde{\psi}*, \tilde{\psi})$, where $\tilde{\psi}$ is the perturbed flux solution and also the eigenfunction of our eigenvalue problem. $K(\tilde{\psi}*, \tilde{\psi})$ is instead the perturbed kinetic energy. Deriving the evolution of the perturbed potential energy δW as function of u_c, starting from $u = u_b$ up to $u = u_X$, allow us to locate the marginal stability surface, $u = u_{marg}$. Unfortunately, this formulation brings to the resolution of a ill-conditioned system, causing the obtained results to have a level of accuracy decreasing with $|u| = |u_c|$; making it necessary to deal with extrapolation methods in the last part of this work in order to obtain the all $\delta W_{(u_c)}$ curve to find the marginal stability flux surface.

Acknowledgements

I start here by thanking Professor Francesco Porcelli, without whom this thesis would not have been possible. I also thank him for the time he dedicated to me and the technical and work advice he gave me during these months. I also thank Adil Yolbarsop, who dedicated precious time to clarifying any doubts I might have.
I would like to thank then my family, Alessandro, Sofia and Sonia, who have always supported me during this journey. I thank then my grandparents, those who are gone, Giocondo and Imola, and those who are still here, Giorgio and Rosa, my uncles and aunts, Andrea, Diego, Gitania, Giuliano, Mariella, Roberto and Simona, and my cousins all, Anna, Anna, Caterina, Chiara, Emma, Francesco and Tommaso.
I thank my girlfriend Sofia, who put up with me during these last years of changes and a bit of madness. It is then necessary to thank all my friends, from those of a lifetime and not, Pizzo, Edoardo, Gmailo, Filippo, Pontro, Giorgione, Giovanni, Beppe, Leonardo, Spindor, Scatt, Matteo, Cami, Sanfi, Peccho and Tommo, to those who have accompanied me in these years of study in Turin, Alex, Vigno, Giacomo, Giulio, Rachi, Maria Grazia and Stelio.
Every person I mentioned has not always been present in my life, someone has arrived later, with someone we see each other sometimes and with others it is more difficult to get together like in the old days. It is rightly so. I am, like everyone, made up of events and memories, and in each of these there is always at least one of you. In short, a person is not made up of a single thing but is the set of memories that accompany him every day and make him who he is. This is why I say thank you, because all of you are my self.

Contents

List of Figures

List of Tables

Physical Constants

Speed of Light	$c_0 = 2.997924588 \cdot 10^8 \mathrm{m\,s^{-1}}$
Vacuum Permeability	$\mu_0 = 4\pi \cdot 10^{-7} \mathrm{H\,m^{-1}}$
Vacuum Permittivity	$\epsilon_0 = 8.8541878128 \cdot 10^{-12}\ \mathrm{F\,m^{-1}}$
Electric Charge	$e = 1.602 \cdot 10^{-19}\ \mathrm{C}$
Electron Mass	$m_e = 9.1093837 \cdot 10^{-31}\ \mathrm{kg}$

List of Symbols

n	number density	cm^{-3}
T	temperature	keV(kiloelectronvolt)
B	magnetic field	T (tesla)
I	current	MA (megamperes)
a	minor radius	m
b	major semi-axis of elliptical cross section	m
R_0	major radius	m
λ_D	Debye Length	cm
τ_P	Characteristic time	s
ω_P	Plasma frequency	s^{-1}
g	Plasma paramater	
ρ	Density	$\mathrm{kg\,m}^{-3}$
v	Velocity	$\mathrm{m\,s}^{-1}$
E	Electric Field	$\mathrm{V\,m}^{-1}$
B	Magnetic Field	$\mathrm{A\,m}^{-1}$
p	Pressure	$\mathrm{N\,m}^{-2}$
γ	Adiabatic Constant	
J	Current Density	$\mathrm{A\,m}^{-2}$
V_A	Alfvén Velocity	$\mathrm{cm\,s}^{-1}$
τ_A	Alfvén Time	s
ψ	Adimensional Magnetic Flux Function	
ϕ	Adimensional Stream Flux Function	
β	Normalized Plasma Pressure	
q	Safety Factor	
e_0	Ellipticity	
ξ	Constant Displacement Amplitude	
δW	Adimensional Perturbed Potential Energy	
γ_H	Growth Rate	$\mu\mathrm{s}^{-1}$

To everyone I know.

Chapter 1

Introduction

One of the most important challenges of today is to achieve more energy as possible from renewable resources. Nuclear fusion is one of the candidates that could be the solution to suppress our need of green energy in the near future. Even though fusion of atoms' nuclei takes place around 10^{38} times per second inside the Sun and in other billions of stars in the universe, achieving this mechanism is very difficult. The high temperature/energies needed to fuse atoms and the confinement needed to maintain the process running and plasma confined inside a specific region are only two of the many problems present int today geometries that have been developed to achieve nuclear fusion inside earth's laboratories. Plasma for nuclear fusion normally consists of hydrogen nuclei and electrons in various isotopic combination. For generic plasma different models, spanning from classical particles description to statistical description as for fluids, are used to describe it. We are going here to adopt the hydromagnetic model, called **ideal-MHD** model, where MHD stands for Magneto-Hydro-Dynamic and ideal because resistivity is assumed to be infinite.
In this thesis the aspect related to stability will be taken under the lens. Plasma stability is very important in nuclear fusion, as not controlled instabilities could bring to disruption events, with the end of the fusion process and the damaging of external materials. One of the most successful configurations where plasma is magnetically confined is the tokamak geometry, where the combination of toroidal and poloidal fields gives life to a magnetic torus capable, inside which plasma is contained. An important variation of this structure is the one where divertor plates are adopted. These latter increase plasma confinement efficiency and its performances, as it allows heat and fluxes exhausted by the plasma to be located inside a particular region, as shown in figure 1.1.

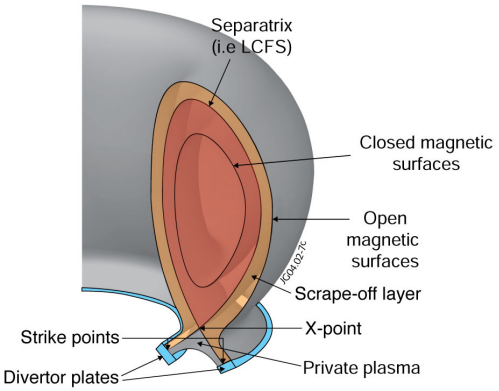

FIGURE 1.1: Divertor tokamak section [1]

[1] Figure from JET website

The external divertor plates also elongate plasma by pulling it from up and down. This elongation is directly connected to the instability problem. In fact, the resulting equilibrium of the system is intrinsically unstable against vertical displacements of the plasma column. In order to suppress this vertical instability, all shaped tokamaks require a feedback stabilization system. In case of slow-time growing instabilities this stabilization system is represented in essence by feedback currents flowing in external coils that are capable of pushing back the plasma. In case of fast-time growing perturbations, this active stabilization would take to long to stabilize the plasma column, thus is essential to provide a fast stabilization mechanism. This latter is achieved by placing a conducting wall near plasma boundary, where eddy currents are generated leading to passive stabilization of the vertical instability. An other important passive mechanism is the one that will be the main subject of our analysis and it is related to current sheets forming on plasma's boundary, and able to stabilize in some conditions the perturbed plasma column.
This thesis is a continuation of the work done in [paper], extending the analysis performed in two extremal scenarios to intermediate cases. The important result of the mentioned paper is the derivation of the growth rate γ, illustrated later on, that is a parameter to understand if the perturbed plasma will be result to be stable or not, and how fast the oscillations regarding the stability/instability of the system will be. More details about this problem will be given later on, for the moment this first chapter will be devoted to introduce plasma, in particular why and how is used for nuclear fusion.

1.1 Tokamak geometry

A lot of magnetic geometries have been proposed during the last century in order to overcome different problems raising up in nuclear fusion. Here below is reported a list [2], to understand the variety of ideas behind nuclear fusion.

Belt pinch	Reversed field pinch
Cusp	Screw pinch
Elmo bumpy torus	Spherical tokamak
Field reversed configuration	Spheromak
Force-free pinch	Stellarator
Heliac	Stuffed caulked cusp
High β stellarator	Tandem mirror
Levitated dipole	Theta pinch
Mirror	Tokamak
Octopole	Tormac
Perhapsatron	Z-pinch
Plasma focus	Z-pinch – hard-core

Of this long list two concepts have risen to the top, largely because of superior overall plasma physics performance. These are the tokamak and the stellarator. Focusing on the first one, a general overview of its internal structure is proposed in Figure 1.2. This is the original limiter configuration, in 1980s, of JET, Joint European Torus. This machine could confine a plasma within a vacuum chamber having a volume of about 10^2 m^3. The major radius of the JET toroidal chamber is $R_0 \approx 3$ m, the horizontal minor radius is $a \approx 1m$ and the vertical radius (the major semi-axis of the nearly elliptical cross-section) is $b \approx 1.8$ m . Its cross-section has a characteristic D-shape. Typical JET operations involved a toroidal magnetic field of up to 4 T and

[2] List from [4]

a plasma current of up to 5 MA (actually, the highest current achieved at JET was 7 MA, which is still today the world record current produced in a tokamak).
Plasma is contained inside the D-shaped vacuum chamber in order to maintain the hydrogen plasma extremely pure, thus minimizing energy losses due to atomic recombination radiation. The typical density of the plasma in a tokamak is of the order of 10^{19} particles per cubic meters, which is about 10^{-6} times the number of particles in a cubic meter of ordinary air. Also the pre-plasma introduction vacuum conditions must be extreme. In order to reach such extreme conditions in such a large volume, the chamber is sealed to perfection and very powerful vacuum pumps must be used.

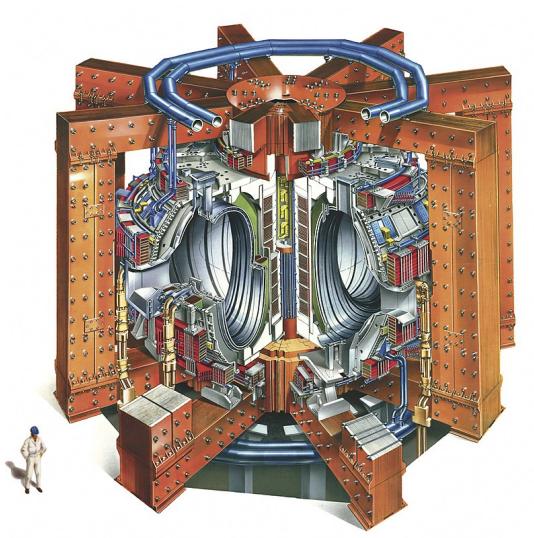

FIGURE 1.2: JET (Joint European Torus) in 1980 [3]

[4] Plasma is confined inside magnetic flux surface, where the magnetic field is obtained from two different contributions, one toroidal and one poloidal. The toroidal magnetic field is obtained with toroidal field coils, which wind around the vacuum chamber from the outside in a solenoidal fashion, figure 1.3. The poloidal field is produced by a toroidal current carried by the plasma, which in turn is induced by transformer action, with the plasma itself playing the role of the secondary transformer circuit. The primary transformer current is flowing in inner poloidal field coils through the geometrical axis of the toroidal vacuum chamber, see figure 1.4.

[4] Figure from Wikipedia JET page

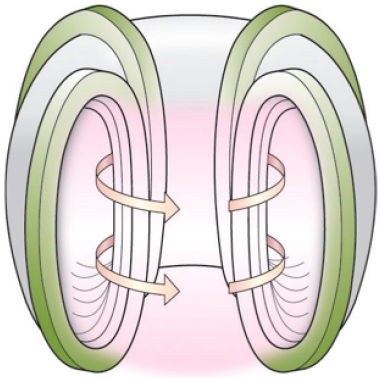

FIGURE 1.3: Toroidal field produced by external solenoidal coils [5]

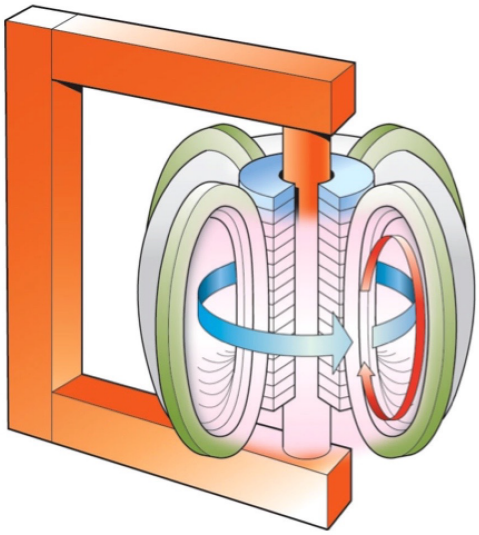

FIGURE 1.4: Poloidal field produced by current carried by the plasma [6]

Finally, outer poloidal field coils, indicated in green in figure 1.5, are necessary for plasma position and shaping, while in light blue is the resultant helical magnetic field.

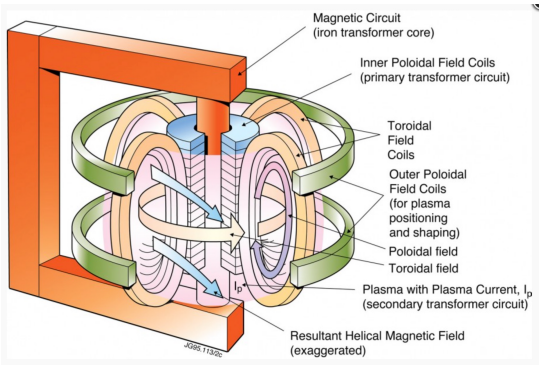

FIGURE 1.5: Tokamak magnetic field[7]

[5] Figure from professor Porcelli's notes
[6] Figure from professor Porcelli's notes

We have illustrated how a tokamak is built and how plasma is confined inside the vacuum chamber, the other important aspect is obviously the one regarding the temperature in order to achieve fusion, in particular which sources provide heat in order to arrive at proper working conditions. One form of plasma heating present in all tokamaks is Ohmic heating due to the plasma current and the finite electrical resistivity of the plasma. Indeed, a hot plasma is an excellent conductor, with a resistivity comparable with that of copper. However, in contrast with ordinary metallic conductors, as the plasma temperature is increased, plasma resistivity goes down as $\eta \propto T^{-3/2}$. Hence, in large size tokamaks such as JET, ohmic heating alone cannot bring the plasma temperature to the values that are required in a thermonuclear reactor, i.e., $10 - 20$ keV. The maximum temperature that can be achieved at JET by means of Ohmic heating alone is about 3 keV. Two main types of plasma heating employed at JET and in most tokamaks are (see figure 1.6):

- Neutral Beam Injection (NBI): beam of high-energy neutrals (normally hydrogen atoms in various isotopic forms), with kinetic energies typically in the range of 100 keV per neutral atom and beam powers of the order of tens of MW, is injected into the plasma. Once inside, the beam particles become ionized and transfer their kinetic energy to the plasma via Coulomb collisions.

- Radio-frequency heating: involves the injection into the plasma of high power electromagnetic waves. These waves have special frequencies values that match characteristic frequencies of the charged particle motion, such as the ion or the electron cyclotron frequency, or of characteristic plasma waves. In this way, a resonant interaction between the injected e.m. waves and the plasma occurs, which allows for the absorption of the e.m. wave energy by the plasma.

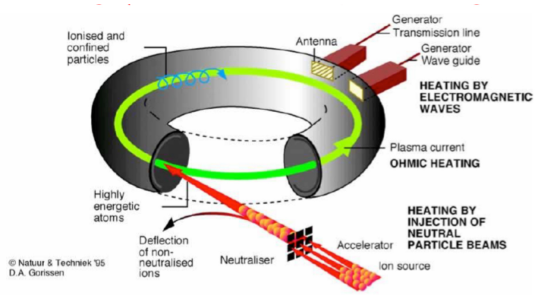

FIGURE 1.6: NBI and radio-frequency heating [8]

The last part we have to mention about tokamak's geometry is related to prevent the plasma-wall interaction. In the first generation tokamaks, the problem was dealt with by the introduction of a limiter, i.e., a material surface within the tokamak vessel that defines the edge of the plasma and thus avoids contact between the plasma and the inner wall of the vacuum chamber. However, as more and more powerful tokamaks were built, limiters could not prevent heat and particle fluxes exhausted by the plasma to reach the inner wall. The introduction of divertor configurations, that we have mentioned in the beginning of this chapter (see figure 1.1), somewhat ameliorated the problem and the resulting effect on plasma-facing components, making it tolerable in present-day tokamak facilities.

[7] Figure from professor Porcelli's notes
[8] Figure from JET website

1.2 General definition

We start here by giving the definition for a generic plasma, followed by the analysis of some important parameters.

> A plasma is a ionized gas, electrically quasi-neutral and dominated by collective phenomena.

To properly understand the given definition, a simple thought experiment will be illustrated.
Considering a fixed charged particle inside the plasma, free particles will be attracted up to a distance r where the electrostatic force starts to vanish. The accumulation of particles around our charge will produce a shielding effect, thus reducing the distance at which a free particle can feel the force produced by the fixed charge. This distance is called Debye length, λ_D, and is what is needed to define the concept of quasi-neutrality on a length scale.

$$\lambda_D = \sqrt{\frac{T}{4\pi n e^2}} \tag{1.1}$$

For a fusion tokamak plasma, where $T \sim 10$ keV and $n \sim 10^{14}$ cm^{-3} (consult **List of symbols** for unit of measures) $\lambda_D \sim 7 \cdot 10^{-3}$ cm .
An other important parameter is the plasma frequency, or the characteristic inverse time of charge separation. This is the frequency of harmonic electrons' motion produced by electric fields, that are generated by the violation of charge neutrality below Debye length scales. The characteristic time is define as

$$\tau_P = \sqrt{\frac{m_e}{4\pi n e^2}}$$

In tokamak plasma, $n_e \sim 10^{14}$ cm^{-3} and $\omega_p \sim 5.6 \cdot 10^{11}$ s^{-1}. As just said quasi-neutrality does not imply the absence of electric fields, but their divergence is almost zero

$$\nabla \cdot \mathbf{E} = 4\pi e(n_i - n_e) \approx 0$$

That implies that the plasma current must be divergence-free

$$\nabla \cdot \nabla \times \mathbf{B} = 0 = \frac{4\pi}{c}\nabla \cdot \mathbf{J} + \frac{1}{c}\nabla \cdot \mathbf{E}$$

Because $\nabla \cdot \mathbf{J} = 0$, charges cannot accumulate in the plasma. Considering also the charge continuity equation

$$\frac{\partial \rho}{\partial t} + \nabla \cdot \mathbf{J} = 0$$

with $\rho \approx 0$ at time t_0, the divergence-free condition ensures quasi-neutrality at all times.
After these important quantities have been analyzed, is now clear that the conditions for quasi-neutrality can be respected if the characteristic length L is much larger than the Debye length, $L \gg \lambda_D$, and if the plasma exists for a time τ larger then the characteristic time scale, $\tau \gg \tau_P$. This concept makes sense if the number of particles inside a Debye sphere is large, $\frac{4\pi}{3}\lambda_D^3 n$, and the inverse of such number (except for the factor $4/3\pi$) is called the **plasma parameter**:

$$g = (n\lambda_D^3)^{-1} \tag{1.2}$$

The condition $g \ll 1$ is often taken as the definition criterion for a plasma. If this condition is satisfied the inter-particle collision is weak, so a collective behavior can dominate over individual particle behavior. With these conclusions we have now a more clear understanding of what is plasma, more specifically of its definition. From now on, we will focus on illustrating the magneto-hydro-dynamic model, which will be the one used to describe a magnetically confined plasma in a divertor tokamak configuration.

Chapter 2

Ideal-MHD model

2.1 Ideal-MHD for nuclear fusion

As previously stated, we will make use of the magnetohydrodynamics (MHD), a fluid model that describes the macroscopic equilibrium and stability properties of a plasma. There are different version of the MHD model, the one that we are going to use is the **ideal-MHD** model which assumes that the plasma can be represented by a single fluid with infinite electrical conductivity and zero ion gyro radius.
MHD equilibrium and stability are necessary requirements for a fusion reactor. If an equilibrium exists but is MHD unstable the result is almost always very undesirable. There can be a violent termination of the plasma known as a major disruption. If no disruption occurs, the result is likely to be a greatly enhanced thermal transport which is highly detrimental to fusion power balance. In order to avoid MHD instabilities it is necessary to limit the regimes of operation so that the plasma pressure and current are below critical values. However, these limiting values must still be high enough to meet the needs of producing fusion power. In fact it is fair to say that the main goal of ideal MHD is the discovery of stable, magnetically confined plasma configurations that have sufficiently high plasma pressure and current to satisfy the requirements of favorable power balance in a fusion reactor.

2.1.1 Description of the model

The ideal-MHD model provides a single-fluid description of long-wavelength, low-frequency, macroscopic plasma behavior. The equations for this model are derived from the four Maxwell's equations and from equations deriving from a more fundamental kinetic model, which describes the behavior of the electron and ion distribution functions, from there some assumptions are made, based on the particular operating conditions, in order to close the system and obtain the final solutions.
One important aspect regarding the assumptions made for this model is related to the fact that plasma is collision dominated. Considering a thermonuclear plasma, it can be shown that the collision frequency for electron-electron collisions is $\nu_{coll} \sim 0.5 \cdot 10^4$ and the mean free path is $\lambda_{mfp} \sim 8$ km. That means the assumption of high collision dominance is never satisfied for a nuclear plasma. Even tough one of the main assumption of the ideal-MHD is never satisfied, this is model still describes plasma behavior surprisingly good. This is not "good luck", and the physical explanation as to deal with the fact that those parts of the MHD model that are not valid because of violation of the collision dominated assumption, are not directly involved in many if not most phenomena of interest, thus making the model correctly working for real conditions.
Ones the system is closed with the correct assumptions, the final equations describing the ideal-MHD model are:

$$\begin{aligned}
&\text{Mass} && \frac{\partial \rho}{\partial t} + \nabla \cdot (\rho \mathbf{v}) = 0 \\
&\text{Momentum} && \rho \frac{d\mathbf{v}}{dt} = \mathbf{J} \times \mathbf{B} - \nabla p \\
&\text{Energy} && \frac{d}{dt}\left(\frac{p}{\rho^{\gamma}}\right) = 0 \\
&\text{Ohm's law} && \mathbf{E} + \mathbf{v} \times \mathbf{B} = 0 \\
&\text{Maxwell} && \nabla \times \mathbf{E} = -\frac{\partial B}{\partial t} \\
& && \nabla \times \mathbf{B} = \mu_0 \mathbf{J} \\
& && \nabla \cdot \mathbf{B} = 0
\end{aligned} \tag{2.1}$$

In these equations, the electromagnetic variables are the electric field **E**, the magnetic field **B**, and the current density **J**. The fluid variables are the mass density ρ, the fluid velocity **v**, and the pressure p. Also, $\gamma = 5/3$ is the ratio of specific heats and $dx/dt = \partial/\partial t + \mathbf{v} \cdot \nabla$ is the convective derivative.
Observe that in ideal MHD the electromagnetic behavior is governed by the low-frequency, pre-Maxwell equations. The MHD fluid equations describe the time evolution of mass, momentum, and energy.
The mass equation implies that the total number of plasma particles is conserved; phenomena such as ionization, recombination, charge exchange, and unfortunately fuel depletion by fusion reactions, are negligible to a high order of accuracy on the MHD time scale.

2.2 Conservation relations

The results obtained up to now must satisfy the basic conservation laws (locally or globally). A canonical local conservation form is given by

$$\frac{\partial ()}{\partial t} + \nabla \cdot () = 0 \tag{2.2}$$

Once the mass, momentum, and energy equations can be written in this form, it is then straightforward to derive the global conservation relations. We will first start from the MHD mass equation

$$\frac{\partial \rho}{\partial t} + \nabla \cdot (\rho \mathbf{v}) = 0,$$

which is already written in the canonical form of a conservation law. So we can easily state that mass is locally conserved.

2.2.1 Momentum conservation

Starting from momentum equation in 2.1.1, and using the tensor identity $\nabla \cdot (\mathbf{AC}) = (\nabla \cdot \mathbf{A})\mathbf{C} + (\mathbf{A} \cdot \nabla)\mathbf{C}$, after some calculations we can finally write the momentum conservation law as follow:

$$\frac{\partial \rho \mathbf{v}}{\partial t} + \nabla \cdot \mathbf{T} = 0 \tag{2.3}$$

where the first term in the l.h.s of the equation represents the variation in the momentum within a volume element. This variation generated by the net flux of momentum, $\nabla \cdot \mathbf{T}$, through the boundaries of the volume element.
The term $\mathbf{T}$ contains

$$\mathbf{T} = \rho \mathbf{v}\mathbf{v} + \left(p + \frac{B^2}{2\mu_0} \right) \mathbf{I} - \frac{1}{\mu_0} \mathbf{B}\mathbf{B}$$

where, $\rho \mathbf{v}\mathbf{v}$ is represents the Reynolds stress and is not important in studies of plasma stability, where the equilibrium flows are assumed to be small or zero. The remain contribution includes the effect of the plasma pressure and magnetic field. If we consider a orthogonal coordinates system, where one coordinate is aligned with along $\mathbf{B}$, these contributions can be rewritten as

$$\mathbf{T_B} = \begin{bmatrix} p_\perp & 0 & 0 \\ 0 & p_\perp & 0 \\ 0 & 0 & p_\parallel \end{bmatrix} \tag{2.4}$$

where

$$p_\perp = p + \frac{B^2}{2\mu_0} \tag{2.5}$$

$$p_\parallel = p - \frac{B^2}{2\mu_0} \tag{2.6}$$

These two contributions represent the total pressures perpendicular and parallel to the magnetic field, respectively. In equations 2.5, the contribution coming from particles pressure acts isotropically perpendicular and parallel to the field. On the contrary, the pressure coming from the magnetic field produces a tension along the magnetic field lines (negative contribution $-B^2/2\mu_0$), while produces pressure perpendicular to the field line (positive contribution $B^2/2\mu_0$). This anysotropic behavior is essential in understanding the equilibrium and the stability properties of the magnetic geometry of fusion interest.

2.2.2 Conservation of energy

Passing from MHD's model equations 2.1.1 to the energy conservation equation requires several steps, that we will not show here for the sake of simplicity. The final result is written in the canonical form as

$$\frac{\partial w}{\partial t} + \nabla \cdot \mathbf{s} = 0 \tag{2.7}$$

where

$$w = \frac{1}{2}\rho v^2 + \frac{p}{\gamma - 1} + \frac{B^2}{2\mu_0} \tag{2.8}$$

$$\mathbf{s} = \left(\frac{1}{2}\rho v^2 + \frac{p}{\gamma - 1} \right) \mathbf{v} + p\mathbf{v} + \frac{1}{\mu_0} \mathbf{E} \times \mathbf{B} \tag{2.9}$$

Here w is the total energy, composed by the kinetic, internal and magnetic energies. The quantity $\mathbf{s}$ is comprised of the net flux of kinetic plus internal energy, the mechanical work done on the plasma through compression, and the flux of electromagnetic energy as given by the Poynting vector.

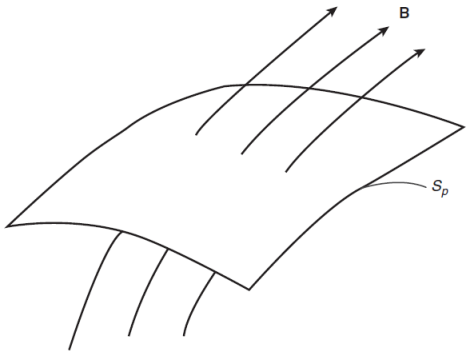

FIGURE 2.1: Magnetic flux passing through a surface S_p with normal vector $\mathbf{n}$ [1]

2.2.3 Global conservation

With the results just obtained, has been shown that ideal-MHD equations can be written in a local conservation form, in which each term has a simple physical explanation. It is also possible to integrate the equations in order to obtain a global conservation form over an appropriate volume. The global conservation laws for the ideal-MHD model are exact and are valid for general, non-linear, multidimensional, time-dependent situations. The specific forms of the global laws, as well as the choice of the appropriate integration volume, depend on the boundary conditions to be applied. Particular attention must be paid when dealing with systems comprehensive of external coils, because energy is no more conserved as it can be provided or extracted from the system. Anyway, also in this case it is still possible to derive a relatively simple energy balance relation for the system.

2.3 "Frozen-in" law

One last important law valid for the ideal-MHD fluid model concern the magnetic flux, and deals with is conservation. This one is of fundamental importance, in particular for the equilibrium and stability analysis, because is one of main parts that differ the ideal-MHD from other MHD models. The result that we are now going to derive, which is a consequence of the perfect conductivity Ohm's law, is that the magnetic flux contained within an arbitrary open surface area moving with the plasma does not change; that is, the flux is "frozen" into the plasma. We start by defining the magnetic flux ψ passing through an open area S_p in the plasma, as shown in figure 2.1, as

$$\psi = \int_{S_p} \mathbf{B} \cdot \mathbf{n}\, dS \tag{2.10}$$

Assuming that this plasma surface is moving with velocity $\mathbf{v}$, as it moves the change in the flux passing through this area is given by

$$\frac{d\psi}{dt} = \int_{S_p} \frac{\partial \mathbf{B}}{\partial t} \cdot \mathbf{n}\, dS - \oint \mathbf{v} \times \mathbf{B} \cdot d\mathbf{l}$$

[1] Figure from [4]

where $d\mathbf{l}$ is the arc length along the perimeter of the surface. Substituting for $\partial\mathbf{B}/\partial t$ from Faraday's law and then converting the surface integral into a line integral by applying Stokes' theorem yields

$$\frac{d\psi}{dt} = -\oint(\mathbf{E} + \mathbf{v} \times \mathbf{B}) \cdot d\mathbf{l}$$

Clearly, if the plasma obeys the ideal-MHD Ohm's law then

$$\frac{d\psi}{dt} = 0 \tag{2.11}$$

Since the derivation of equation 2.11 applies to any arbitrary surface area, it immediately follows that by setting S_p equal to the entire cross section of the plasma, the total flux contained within an ideal-MHD plasma is conserved.
The conservation of flux relation has very important implications about the structure of the magnetic field. This follows because any allowable physical velocity $\mathbf{v}$ of the plasma requires that neighboring fluid elements remain adjacent to one another; fluid elements are not allowed to tear or break into separate pieces. Since the magnetic lines move with the plasma, the field line topology must thus be preserved during any physically allowable MHD motion. This is a very strict requirement on the structure of the magnetic fields.

Chapter 3

Ideal-MHD equilibrium and stability

3.1 Equilibrium in a one-dimensional configuration

Before analyzing the stability of our model is necessary to define the equilibrium configuration, in particular for a tokamak plasma. We refer here as an equilibrium state for a plasma the condition in which $d\boldsymbol{v}/dt = 0$ is satisfied, that is much stronger than only saying $\partial\boldsymbol{v}/\partial t = 0$, i.e. the fluid is not only stationary (not depending on time) but also static ($\boldsymbol{v} = 0$). The ideal-MHD equations 2.1.1, can thus be rewritten as

$$\boldsymbol{J} \times \boldsymbol{B} = \nabla p \tag{3.1}$$
$$\nabla \times \boldsymbol{B} = \mu_0 \boldsymbol{J} \tag{3.2}$$
$$\nabla \cdot \boldsymbol{B} = 0 \tag{3.3}$$

Equilibrium is achieved by balancing the magnetic force $\boldsymbol{J} \times \boldsymbol{B}$ with the pressure gradient force ∇p. The study of the force balance is referred to as **magnetostatics**. Taking the scalar multiplication of equation 3.1 with $\boldsymbol{B}\cdot$ and with $\boldsymbol{J}\cdot$ brings to

$$\boldsymbol{B} \cdot \nabla p = 0 \tag{3.4}$$
$$\boldsymbol{J} \cdot \nabla p = 0 \tag{3.5}$$

From the first relation of 3.4 we can conclude that for a well-confined equilibrium and an axisymmetric configuration, the pressure is maximum near the center of the poloidal cross section and is not varying around the toroidal direction. For such profiles the contours of constant pressure are nested toroidal surfaces (see figure 3.1). These surfaces, with p = constant, are usually referred to as magnetic flux surfaces or simply just flux surfaces. A similar conclusion can be obtained for the second relation, which implies that the current lines also lie on the surfaces of constant pressure; making the important point that the current flows between and not across flux surfaces. Even though $\boldsymbol{B}$ and $\boldsymbol{J}$ lie on constant p contours they are usually not parallel or perpendicular. Even though magnetic confinement equilibria of fusion interest are intrinsically toroidal, it is possible to develop a physical intuition about the nature of these equilibria by considering at first one-dimensional configurations with cylindrical symmetry, i.e. such that p and B depend only on the radial coordinate. The actual toroidal configuration, in the limit of very large aspect ratio, $R_0/a \to \infty$, realized in the case of low-β tokamak machines,can be analyzed with a simplified model composed of a cylinder of length L, with periodic boundary conditions at its

[1] Figure from [4]

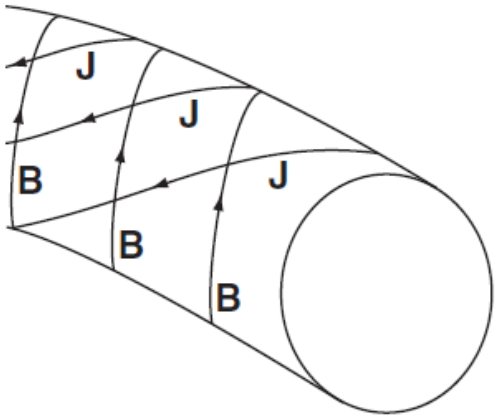

FIGURE 3.1: Toroidal flux surface showing magnetic lines and current lines lying on the surface. [1]

bases.
Here β is the normalized plasma pressure and is a global plasma parameter whose value is critical for a fusion reactor. It is expressed as:

$$\beta = \frac{\text{plasma pressure}}{\text{magnetic pressure}} \tag{3.6}$$

3.1.1 MHD safety factor

This quantity is typically used to describe 2D axisymmetric configurations such as the tokamak, and is a qualitative indicator of stability. High q are better and obviously preferable, while low q express a worst behavior of stability. It is expressed as:

$$q = \frac{2\pi}{l} \tag{3.7}$$

where l is the rotational transform. We have previously introduced how the shape of the magnetic field lines for a tokamak. It is important to consider that magnetic field line trajectories must be distinguished in three classes: rational, ergodic, and stochastic. In the first one lines exactly closed on themselves after a finite number of toroidal circuits; in the second they do not close, but instead wrap around indefinitely covering the entire constant pressure contour. Lastly, the field line wanders around and actually fills a volume, creating a region of stochasticity.
If the rotational transform is a rational fraction of 2π, then the line of the magnetic field is closed, while if it is not, the line is ergodic. The rotational transform plays an important role in both equilibrium and stability, and is defined as

$$l = \lim_{N\to\infty} \frac{1}{N} \sum_{1}^{N} \Delta\theta_n \tag{3.8}$$

where $\Delta\theta$ is the difference in the angle produced by a complete revolution of a magnetic field line. So, The rotational transform is the average value of the angle $\Delta\theta$ after an infinite number of transits

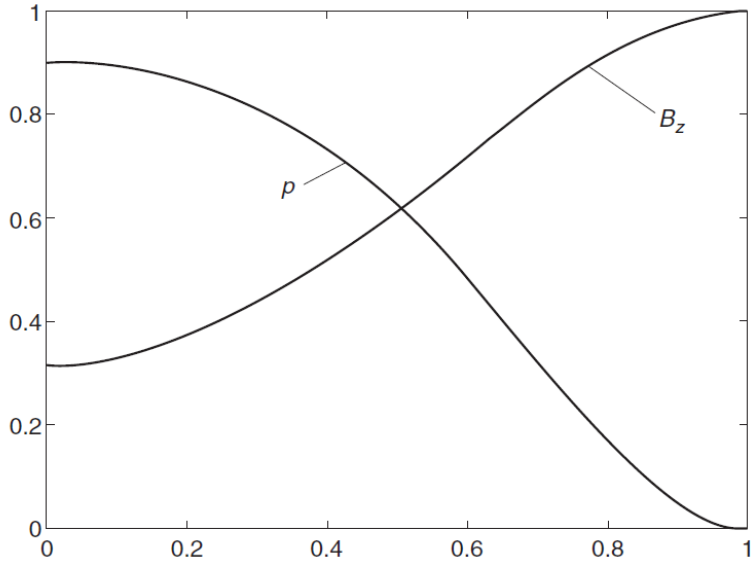

FIGURE 3.2: θ-pinch axial magnetic field profile, with given $p(r)$ [2]

3.1.2 θ-pinch configuration

The simplified model of the cylinder can be analyzed with two different configurations. The first one is the θ-pinch, which represents the one-dimensional analog of the toroidal configuration with purely toroidal field. Here the magnetic field, $\boldsymbol{B} = B_z(r)\boldsymbol{e_z}$, is directed along the cylinder axis and is applied externally. The magnetic field also induces a large diamagnetic current in the θ direction, $\boldsymbol{J} = J_\theta(r)\boldsymbol{e_\theta}$, from this the origin of the θ-pinch name.
The curvature vector

$$\boldsymbol{k} = \boldsymbol{n}/R \tag{3.9}$$

is equal to zero, since the field lines are straight. In this case equation 3.1 reduces to

$$\frac{d}{dr}\left(p + \frac{B_z^2}{8\pi}\right) = 0 \tag{3.10}$$

where d/dr is the derivative w.r.t. the radial direction. The solution to the previous equation is

$$p + \frac{B_z^2}{8\pi} = constant = \frac{B_0^2}{8\pi} \tag{3.11}$$

where B_0 is the applied magnetic field. Equation 3.11 indicates that at any local value of r the sum of the local particle pressure plus local magnetic pressure is a constant, equal to the externally applied magnetic pressure. Thus, in a θ-pinch, the magnetic tension force is zero and the gradient of the magnetic pressure provides radial confinement. Because the solution contains one free, unspecified function, one must specify the plasma pressure or the axial magnetic field to obtain the other. For example a profile for $p(r)$, consistent with the experimental observations, can be chosen and then the axial magnetic field that is necessary for radial force balance is derived accordingly to equation 3.11.

[2] Figure from [4]

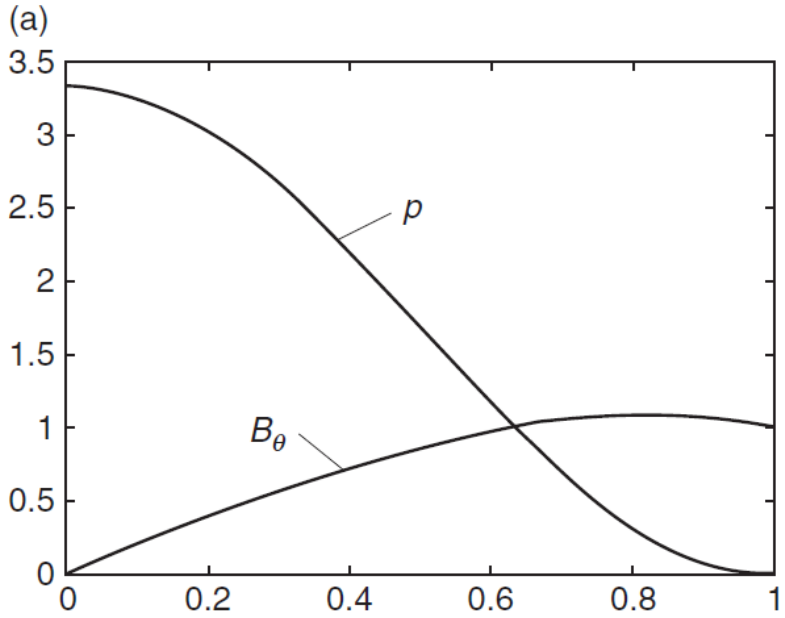

FIGURE 3.3: Equilibrium profiles for a Z-pinch: Bennett pinch solution. Pressure, axial current density and poloidal magnetic field [3]

3.1.3 Z-pinch configuration

In this case, the magnetic field is chosen to be purely poloidal, given by

$$\boldsymbol{B} = B_\theta(r)\boldsymbol{e_\theta} \tag{3.12}$$

and produced by an axial current, $J_z(r)$, carried by the plasma itself. With this consideration, equation 3.1becomes

$$\frac{d}{dr}\left(p + \frac{B_\theta^2}{8\pi}\right) + \frac{B_\theta^2}{4\pi} = 0 \tag{3.13}$$

A standard solution to the previous equation is the so called Bennet pinch:

$$B_\theta(r) = \frac{2I_0 r}{r^2 + r_0^2} \tag{3.14}$$

$$p(r) = \frac{I_0^2}{\pi}\frac{r_0^2}{(r^2 + r_0^2)^2} \tag{3.15}$$

where r_0 is the characteristic radial scale distance of the plasma and I_0 is the total plasma current. The axial current density is

$$J_z(r) = \frac{1}{2} I_0 p(r)$$

so I_0 and $p(r)$ have the same radial profile. As in the previous case, also the Z-pinch equilibrium problem contains a free function. For instance, one can specify the pressure profile $p(r)$ and derive the corresponding $B_\theta(r)$ and $J_z(r)$ profiles that satisfy radial force balance.

[3] Figure from [4]
[4] Figure from [4]

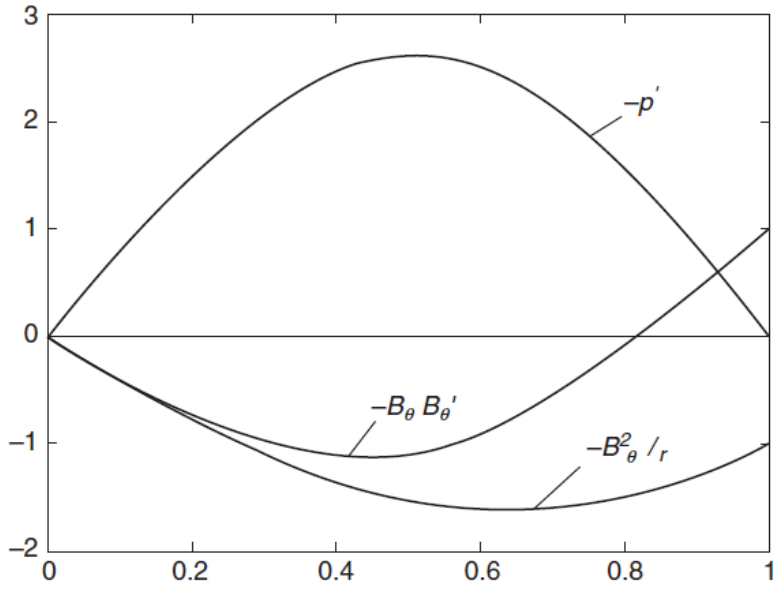

FIGURE 3.4: Comparison between the force terms related to plasma pressure, magnetic pressure and magnetic tension [4]

3.1.4 General screw pinch

The so-called general screw pinch is a cylindrical confinement configuration that combines the features of the θ-pinch and the Z-pinch. The magnetic field for a general screw pinch is thus written as

$$\boldsymbol{B}(r) = B_z(r)\boldsymbol{e_z} + B_\theta(r)\boldsymbol{e_\theta} \tag{3.16}$$

If we assume that the axial magnetic field component is stronger than the poloidal component, and more precisely that

$$\frac{B_\theta}{B_z} \sim \frac{a}{R_0} = \frac{1}{A} \tag{3.17}$$

then the general screw pinch can mimic a straight tokamak, that is, a toroidal plasma configuration in the limit of large aspect ratio. Here R_0 is the major radius of the torus, and a is the minor radius, while the aspect ratio is R_0/a. There are, however, well known limits,related to the ideal-MHD stability of the plasma, which must be satisfied for the straight tokamak to be physically plausible. The first is a limit on the total axial current that the plasma can carry, known as Kruskal-Shafranov limit:

$$q(a) = \frac{aB_z}{R_0 B_\theta} > 1 \tag{3.18}$$

where both the magnetic field values are evaluated at $r = a$. The second is a limit on the maximum plasma beta, the so-called Troyon limit:

$$\beta < \beta_T = 0.028\frac{I}{aB_z} \tag{3.19}$$

where the plasma current I is expressed in Mega-Ampere, the minor radius a in meters and the magnetic field in Tesla.

Respecting the previous limitations, the force balance relation for the straight tokamak is

$$\frac{d}{dr}\left(p + \frac{B_z^2 + B_\theta^2}{8\pi}\right) + \frac{B_\theta^2}{4\pi} = 0 \tag{3.20}$$

In this case equation 3.20 contains two unkowns, that must be defined in order to obtain the last one. For instance, one can specify the plasma pressure and the axial magnetic field, and obtain the poloidal magnetic field and hence the axial current density profile consequently.

3.2 Equilibrium in a two-dimensional configuration

The previous section treated the equilibrium of a one dimensional configuration, where the general screw pinch is able to represent the low-β straight tokamak case. A more general case is to solve the equilibrium problem in a two-dimensional axisymmetric toroidal geometry. This case will not be explained here, because it will be not the case of our interest.

3.3 Ideal-MHD Stability

Since ideal-MHD model is used, so no dissipation from resistivity is present, we will refer as a stability condition the state in which the perturbed system oscillates around the equilibrium position, with the oscillations not growing in time. This equilibrium state can also be represented through a marginal stability or neutral stability, it represents the stability boundary between stability and instability.
With this definition in mind we can start by analyze stability for an infinite homogeneous plasma immersed in a unidirectional magnetic field (taken along the z direction). This is obviously a very simple case, and its stability actually corresponds to a determination of the basic waves that can propagate in an MHD plasma and, as such, forms a basic foundation upon which one can develop intuition that can be applied to more realistic magnetic geometries.

3.3.1 Linearized MHD equations

Starting from the system of solutions for the equilibrium condition, which is:

$$\begin{aligned} \boldsymbol{B} &= B_0 \boldsymbol{e_z} \\ p &= p_0 \\ \rho &= \rho_0 \\ \boldsymbol{J} &= 0 \\ \boldsymbol{v} &= 0 \end{aligned}$$

where B_0, p_0, and ρ_0 are constants. We will then introduce a first order perturbation for all the solutions, indicated with the subscript 1, as

$$\begin{aligned} \boldsymbol{v} &= \tilde{\boldsymbol{v}}_1 \\ p &= p_0 + \tilde{p}_1 \\ \boldsymbol{B} &= \boldsymbol{B}_0 + \tilde{\boldsymbol{B}}_1 \\ \boldsymbol{J} &= \boldsymbol{J}_0 + \tilde{\boldsymbol{J}}_1 \end{aligned}$$

All quantities are linearized about this background state, with

$$Q(\boldsymbol{r}, t) = Q_0(\boldsymbol{r}) + \tilde{Q}_1(\boldsymbol{r}, t) \tag{3.21}$$

Here $Q_0(\boldsymbol{r})$ is representative of the equilibrium, $\tilde{Q}_1(\boldsymbol{r}, t)$ is instead the first order perturbation, with $\tilde{Q}_1/Q_0 \ll 1$.
When substituting into the MHD equations it is convenient to express all perturbed quantities in terms of a vector $\tilde{\boldsymbol{\xi}}(\boldsymbol{r}, t)$, defined by

$$\boldsymbol{v}_1 = \frac{\partial \tilde{\boldsymbol{\xi}}}{\partial t} \tag{3.22}$$

The vector $\tilde{\boldsymbol{\xi}}$ represents the displacement of the plasma away from its equilibrium position. Expressing all the perturbed quantities in terms of this displacement vector we end obtain

$$\rho_0 \frac{\partial^2 \tilde{\boldsymbol{\xi}}}{\partial t^2} = \boldsymbol{F}(\tilde{\boldsymbol{\xi}}) \tag{3.23}$$

where $\boldsymbol{F}(\tilde{\boldsymbol{\xi}})$ is a linear differential operator, called the force operator, acting on $\tilde{\boldsymbol{\xi}}$. It is given by

$$\boldsymbol{F}(\tilde{\boldsymbol{\xi}}) = \boldsymbol{J}_0 \times \tilde{\boldsymbol{B}}_1 + \tilde{\boldsymbol{J}}_1 \times \boldsymbol{B}_0 - \nabla \tilde{p}_1 \tag{3.24}$$

Since the coefficients of $\boldsymbol{F}$ are are constant in time and space (homogeneous equilibrium), we can look for solutions of the type

$$\tilde{\boldsymbol{\xi}}_1 = \boldsymbol{\xi}_1 e^{-i(\omega t - \boldsymbol{k}\cdot\boldsymbol{r})} \tag{3.25}$$

with $\boldsymbol{k} = k_\perp \boldsymbol{e_y} + k_\parallel \boldsymbol{e_z}$, where $\perp$ and $\parallel$ refer to perpendicular and parallel components to the equilibrium field, respectively.
From the linearized equations of motion is possible to compute the eigenvalue ω. The final system of equations can be written as $\boldsymbol{M} \cdot \tilde{\boldsymbol{\xi}} = 0$, where

$$\boldsymbol{M} = \begin{bmatrix} \omega^2 - k_\parallel^2 V_A^2 & 0 & 0 \\ 0 & \omega^2 - k_\perp^2 (V_S^2 + V_A^2) - k_\parallel V_A^2 & -k_\perp k_\parallel V_S^2 \\ 0 & -k_\perp k_\parallel V_S^2 & \omega^2 - k_\parallel^2 V_S^2 \end{bmatrix}$$

Setting the determinant equal to zero, we end up with

$$\omega^2 = k_\parallel^2 V_A^2 \tag{3.26}$$

$$\omega^2 = \frac{1}{2} k^2 (V_A^2 + V_S^2) \left[1 \pm (1 - \alpha^2)^{1/2} \right] \tag{3.27}$$

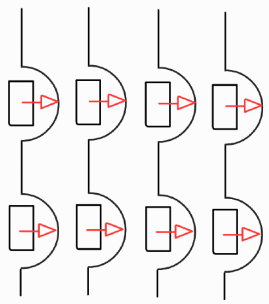

FIGURE 3.5: Shear Alfvén wave, producing a restoring elastic force on the magnetic field [5]

where $V_A = (B_0/\mu_0\rho_0)^2$ is the Alfvén velocity and $V_S = (\gamma p_0/\rho_0)^2$ is the adiabatic sound speed. Also

$$\alpha = 4\frac{k_\parallel^2}{k^2}\frac{V_S^2 V_A^2}{(V_S^2+V_A^2)^2}$$

The obtained results are called **dispersion relations**, as they relate the the wave frequency to the wave number k.
Three different solutions are present in 3.26 and since $0 \leq \alpha \leq 1$, each corresponds to a purely oscillatory solution, i.e. $Im(\omega) = 0$. Thus, we have demonstrated that an homogeneous plasma immersed in a straight magnetic field configuration is exponentially stable. This is not surprising since the system is in thermodynamic equilibrium and there are no sources of free energy available to drive instabilities.
Always considering 3.26, we are now going to analyze three different cases, each of which will corresponds to a type of perturbation propagating inside the plasma.

3.3.2 The shear Alfvén wave

Considering the first branch of the dispersion relation, $\omega_a^2 = \omega^2 = k_\parallel V_A^2$, is known as the shear Alfvén wave and is independent of $k_\perp$ even when $k_\perp^2 \gg k_\parallel^2$. This wave is purely transversal, thus causing the magnetic field to bend, as shown in figure 3.5. It is polarized such that the perturbed magnetic field and velocity are aligned and perpendicular to both $\boldsymbol{B}_0$ and k. Furthermore, the relation $\nabla \cdot \tilde{\boldsymbol{\xi}} = 0$ holds, this mode is then incompressible and produces no density or pressure fluctuations. Plasma is carried with the magnetic perturbation by $\boldsymbol{E} \times \boldsymbol{B}_0/B^2$.
The shear Alfvén wave describes a basic oscillation between perpendicular plasma kinetic energy and perpendicular magnetic energy; that is, a balance between inertial effects and the magnetic tension due to field line bending.

3.3.3 The fast magnetosonic wave

The second branch of the dispersion relation corresponding to the $+$ sign in the second equation of 3.26 describes the fast magnetosonic wave, ω_f^2. From a calculation we can find the relation $\omega_f^2 \geq \omega_a^2$. This is a wave in which both the magnetic field and plasma are compressed so that $\nabla \cdot \tilde{\boldsymbol{\xi}} \neq 0$ (see figure 3.6). In the limit $\beta \sim V_S^2/V_A^2 \ll 1$, the fast magnetosonic wave reduces to the compressional alfvén wave

$$\omega_f^2 \approx (k_\perp^2 + k_\parallel^2)V_A^2 \tag{3.28}$$

[5] Figure reproduced by this thesis author, taken from professor Porcelli's notes

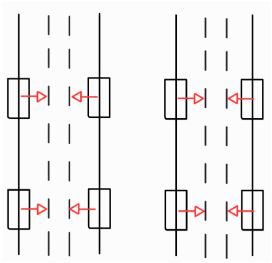

FIGURE 3.6: Fast Magneto-Acoustic wave producing plasma and magnetic field compression [6]

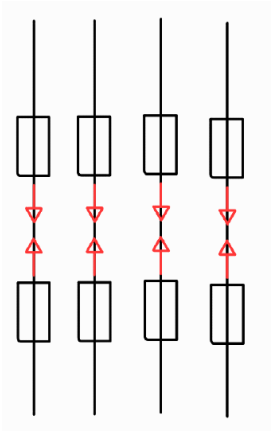

FIGURE 3.7: Acoustic wave, responsible for plasma compression [7]

This compressional Alfvén wave describes a basic oscillation between perpendicular plasma kinetic energy and parallel plus perpendicular magnetic energy. In other words, there is a balance between inertial effects and compression plus tension of the field lines.

3.3.4 The slow magnetosonic wave

The third branch of the dispersion relation corresponds to the slow magnetosonic wave, ω_s^2 . This wave always satisfies $\omega_s^2 \leq \omega_a^2$. As in the fast magnetosonic branch the wave is polarized so that both the plasma pressure and the magnetic field are compressed, so also in this case $\nabla \cdot \tilde{\boldsymbol{\xi}} \neq 0$. However, for the slow magneto sonic wave it is the plasma rather than magnetic field that is primarily compressed, in fact, in the low-β limit, $\beta \sim V_S^2/V_A^2 \ll 1$, the slow magnetosonic wave reduces to a sound wave,

$$\omega_s^2 \approx k_\parallel^2 V_S^2 \tag{3.29}$$

In this limit the mode is nearly longitudinal, see Figure 3.7, hence the sound wave describes a basic oscillation between parallel plasma kinetic energy and plasma internal energy; that is, between inertial effects and plasma compression.

[6] Figure reproduced by this thesis author, taken from professor Porcelli's notes
[7] Figure reproduced by this thesis author, taken from professor Porcelli's notes

3.4 Force operator $F(\xi)$ and normal mode formulation

A more efficient way to investigate linear stability is to reformulate equation 3.23 as a normal mode problem. We can express the perturbed quantity $\tilde{Q}$ as

$$\tilde{Q}_1 = Q_1(\boldsymbol{r})e^{-i\omega t}$$

Upon substituting these relations into the momentum equation, one finds

$$-\omega^2 \rho_0 \boldsymbol{\xi} = \boldsymbol{F}(\boldsymbol{\xi}) \tag{3.30}$$

where the force operator is now expressed as

$$\boldsymbol{F}(\boldsymbol{\xi}) = \frac{1}{\mu_0}(\nabla \times \boldsymbol{B}_0) \times \boldsymbol{B}_1 + \frac{1}{\mu_0}(\nabla \times \boldsymbol{B}_1) \times \boldsymbol{B}_0 + \nabla(\boldsymbol{\xi} \cdot \nabla p_0 + \gamma p_0 \nabla \cdot \boldsymbol{\xi}) \tag{3.31}$$

where $\boldsymbol{B}_1 = \nabla \times (\boldsymbol{\xi} \times \boldsymbol{B}_0)$. Equation 3.30 represents the normal mode formulation of the linearized MHD stability problem for general three-dimensional equilibria. In this approach only appropriate boundary conditions on , are required. It then can be solved as an eigenvalue problem for the eigenvalue ω^2.
Equation 3.30 is a linear differential equation, whose coefficients depend on the equilibrium quantities $p_0(\psi)$, $\boldsymbol{B}_0(\psi, \theta)$, but not on time t neither on the toroidal angle ϕ. Thus, we can search solutions of the type

$$\boldsymbol{\xi}(\boldsymbol{r}, t) = \sum_q \sum_n a_q b_b \boldsymbol{\xi}_{qn}(\psi, \theta) e^{-i(\omega_q t - n\phi)}$$

where each n and q components are decoupled. The linearized equation of motion reduces to a partial differential equation for ψ and θ for each $\boldsymbol{\xi}_{qn}$ component, written as

$$-\rho_0 \omega_q^2 \boldsymbol{\xi}_{qn} = \boldsymbol{F}(\boldsymbol{\xi}) \tag{3.32}$$

The differential operator 3.24 has some important properties, that are:

- self-adjoint: The operator $\boldsymbol{F}$ is equal to its adjoint, i.e. its coonjugate tranpose. To demonstrate this property it is necessary to show that for any two arbitrary vectors $\boldsymbol{\xi}(\boldsymbol{r})$ and $\boldsymbol{\eta}(\boldsymbol{r})$ both satisfying the same well posed boundary conditions, the following relation holds:

  $$\int \boldsymbol{\eta} \cdot \boldsymbol{F}(\boldsymbol{\xi})\, d\boldsymbol{r} = \int \boldsymbol{\xi} \cdot \boldsymbol{F}(\boldsymbol{\eta})\, d\boldsymbol{r}$$

  This is the definition of self-adjointness – switching $\boldsymbol{\xi}(\mathbf{r})$ and $\boldsymbol{\eta}(\mathbf{r})$ leaves the integrals unchanged. Here $\boldsymbol{\xi}(\mathbf{r})$ and $\boldsymbol{\eta}(\mathbf{r})$ are known also as "trial functions", because they do not in general satisfy the actual eigenvalues equation.

- Eigenvalues ω_q^2 are real
- Eigenfunctions $\boldsymbol{\xi}_{qn}$ form a complete orthogonal set

3.5 Stability of the "Straight Tokamak"

The straight tokamak model provides a simple but surprisingly reliable description of the basic MHD instabilities that can arise in a large aspect ratio, circular cross section, low-pressure tokamak. To put the analysis in perspective one should keep in

mind that, in general, experimental tokamak performance seriously degrades when either the current or pressure becomes too large. The straight tokamak is surprisingly accurate in describing the effects of large current. It is not very reliable with respect to pressure-driven limitations because the effects of toroidicity tend to dominate and are obviously not included in the straight tokamak model. The specific tokamak operational limits can be sumarized here as:

- Sawtooth oscillations - internal $m = 1$ mode
- Current-driven disruptions - external low m modes
- Density-driven disruptions - external low m modes
- Resistive wall modes - external low m modes
- Edge Localized Modes (ELMs) - external high m modes

Here m is the poloidal number and we will refer to n as the toroidal number.
It is worth emphasizing that each of the above phenomena are macroscopic in nature and readily observed experimentally. Even though each of these requires non-linear equations and more complicated models to be studied, at the initiation each one of these phenomena is driven by an ideal-MHD instability. In the next chapter a brief description of ELMs will be given, motivated by the fact that there are promising evidences that vertical displacements (the main topic of this thesis) could be the cause of ELMs origins in divertor Tokamak plasma.

3.6 Variational formulation and Energy Principle

We have previously introduce the normal mode formulation, that is a very important method in order to simplify differential equations and to seek out solutions through separation of variables. Furthermore, it is also the starting point to introduce the variational formulation, which is an alternate but entirely equivalent integral representation of the linearized MHD partial differential equations.
Considering equation 3.30

$$-\gamma^2 \rho \boldsymbol{\xi} = \boldsymbol{F}(\boldsymbol{\xi})$$

one can form the dot product with $\boldsymbol{\xi}^*$ (complex conjugate of $\boldsymbol{\xi}$) and then integrate over the plasma volume. This yields

$$\gamma^2 = \frac{\delta W(\boldsymbol{\xi}^*, \boldsymbol{\xi})}{K(\boldsymbol{\xi}^*, \boldsymbol{\xi})} \tag{3.33}$$

where

$$\delta W(\boldsymbol{\xi}^*, \boldsymbol{\xi}) = -\frac{1}{2} \int \boldsymbol{\xi}^* \cdot \boldsymbol{F}(\boldsymbol{\xi})\, d\boldsymbol{r} \tag{3.34}$$

$$K(\boldsymbol{\xi}^*, \boldsymbol{\xi}) = \frac{1}{2} \int \rho |\xi|^2\, d\boldsymbol{r} \tag{3.35}$$

Here, the unimportant numerical factor of "1/2" has been added to both terms so that $\gamma^2 K$ is proportional to the kinetic energy of the plasma $\rho \boldsymbol{v}_1^2/2$. The variational principle states that any allowable trial function $\boldsymbol{\xi}(\boldsymbol{r})$ that produces an extremum (i.e., maximum, minimum, or saddle point) in the value of γ^2 is an actual eigenfunction of the ideal MHD normal mode equations with eigenvalue $\gamma^2 = \delta W(\boldsymbol{\xi}^*, \boldsymbol{\xi})/K(\boldsymbol{\xi}^*, \boldsymbol{\xi})$.

Also, $\delta W(\boldsymbol{\xi}^*, \boldsymbol{\xi})$ represents the change in potential energy associated with the perturbation and is equal to the work done against the force $\boldsymbol{F}(\boldsymbol{\xi})$ in displacing the plasma by an amount $\boldsymbol{\xi}$.
After this first step we can now introduce the energy principle, a very simple, intuitive and powerful tool to understand whether a given MHD configuration is stable or not. The statement that will be illustrated in the following is valid both for a plasma bounded by a perfectly conducting wall and for a plasma surrounded by a vacuum region, separating it by the conducting wall. In the latter case the principle is better known as *"The extended energy principle"*. The physical basis for the Energy Principle is the fact that energy is exactly conserved in the ideal MHD model. As a consequence the particular extremum corresponding to the most negative eigenvalue of γ^2 actually represents the absolute minimum in potential energy δW. The energy principle states

> An equilibrium is stable if and only if
>
> $$\delta W(\boldsymbol{\xi}^*, \boldsymbol{\xi}) \geq 0 \tag{3.36}$$
>
> for all allowable trial displacements (i.e., $\boldsymbol{\xi}$ bounded in energy and satisfying appropriate boundary conditions) [8].

That means we can analyze the sign of δW to understand if our ideal MHD configuration is stable or unstable, without considering the actual value of the growth rate γ^2 and so without analyzing the full variational integral or normal-mode equations. The more general expression of δW is usually written in two different ways, the first one is an explicit form while the second is the intuitive form. Here will be reported only the intuitive form, as we will have to deal with a reduced version due to simplifications introduced by the low-β tokamak limit. The intuitive form of δW is

$$\delta W = \int_{fluid} d^3x \Big[\Gamma p |\nabla \cdot \boldsymbol{\xi}|^2 + \frac{B^2}{4\pi} \big| \nabla \cdot \boldsymbol{\xi}_\perp + 2\boldsymbol{\xi}_\perp \cdot \boldsymbol{\varkappa} \big|^2 \tag{3.37}$$

$$- 2(\boldsymbol{\xi}_\perp^* \cdot \nabla p)(\boldsymbol{\xi}_\perp \cdot \boldsymbol{\varkappa}) - \frac{J_\parallel}{c} (\boldsymbol{\xi}_\perp^* \times \boldsymbol{e}_\parallel) \cdot \boldsymbol{Q}_\perp \Big] \tag{3.38}$$

where $\boldsymbol{Q}_\perp$ is the perpendicular component of $\boldsymbol{Q} = \nabla \times (\boldsymbol{\xi} \times \boldsymbol{B})$. The first three terms are all positive and so always stabilizing terms. The last two (with the minus sign) are possible sources of instabilities, where the first term is the pressure gradient/curvature driven term and the second one represents instead the source driven by the parallel current $J_\parallel$.

[8] Quote from "Ideal MHD", Jeffrey P. Freidberg

Chapter 4

Ideal-MHD vertical displacements

4.1 Vertical Displacements and ELMs

ELMs phenomena typically occur during H-mode operation of a tokamak, which is a regime characterized by improved energy confinement. Even though this type of confinement is an advantage, an H-mode tokamak also has substantial pressure and current edge gradients, which can drive high m MHD instabilities, known as "edge localized modes" or "ELMs" for short. Experimentally, ELMS appear as short, periodic, bursts of particles and energy that are ejected from the plasma. On the positive side each ELM ejects impurities in addition to plasma particles. Preventing the build-up of impurities improves performance in present experiments and is crucial in reactor plasmas where they can dilute the basic D-T fuel. On the negative side the loss of plasma from too many ELMs reduces the time-averaged particle density and temperature, thereby degrading the overall high confinement properties of H-mode operation. Thus, ELMs are responsible for the degradation of plasma confinement and are often associated with the termination of high performance discharges.
This modes are important features of a divertor Tokamak configuration, see figure 1.1, which is adopted in order to improve the confinement and to reduce the effects of plasma-wall interactions. On the other side, divertor geometry produces an elongation on the plasma section, which is prone to an instability. This latter can be initiated by a plasma axisymmetric mode, with toroidal mode number $n = 0$, leading to vertical displacement events (VDEs) where the entire plasma shifts vertically until it touches the vacuum chamber. Uncontrolled VDEs must be avoided as they lead to disruption events, with the termination of the fusion process.
In [8] is argued that axisymmetric perturbations that are resonant at the X point(s) of a magnetic divertor separatrix may play a role in the understanding of Edge Localized Modes in tokamak experiments. In this chapter will be illustrated the analytic theory of resonant axisymmetric X-point modes, starting from more simple scenarios. After the introduction of an heuristic model to understand the stability mechanism, the first case where plasma will be confined inside an elliptical flux surface, which is located inside the separatrix and surrounded by vacuum, will be presented. Afterwards, plasma's boundary will be extended up to the last closed magnetic flux surface, i.e. the magnetic separatrix, and the main results obtain in [12] will be explained. Based on these results from these two first scenarios, the analysis will be further extended to intermediate cases, where the plasma's boundary will be located between the two previously illustrated surfaces.

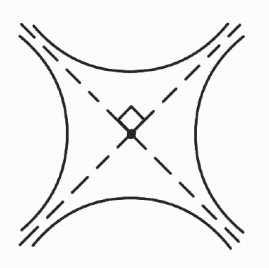

FIGURE 4.1: Hyperbolic structure of X-point

4.2 X-Points topology and current sheets

The divertor configuration that will be used here, is composed by nested magnetic flux surfaces that are bounded by a separatrix, magnetically confining plasma inside. The last closed magnetic surface is called **magnetic separatrix**, and contains two X-points. These are points on the magnetic field lines where the poloidal component of the magnetic field vanishes, $B_p = 0$, and the magnetic confinement is purely toroidal. Near the X-points the the field structure is hyperbolic in nature, as shown in figure 4.1. X-points plays an essential role in plasma stability and one of the first work to analyze this aspect is [Paper citation]. We are in particular concerned about vertical displacements, i.e. axysimmetric perturbations with toroidal mode number $n = 0$. This perturbation is resonant at the X-points, in the sense that, regardless of its poloidal modulation, is constant along the toroidal field line going through the X-point. This resonant condition is analytically expressed as

$$\boldsymbol{B}_{eq} \cdot \nabla \chi = 0 \tag{4.1}$$

, where χ is a generic axysimmetric perturbation and $\boldsymbol{B}_{eq}$ the equilibrium magnetic field. This is trivially fulfilled at the X-points as the only component that is still present is the toroidal one, which is always perpendicular to any such axysimmetric perturbation's gradient $\nabla \chi$.
The resonant nature of these type of perturbations allows for a non-rigid displacement which peaks in the X-point region, while plasma's centroid is instead not significantly displaced. We here means by **non-rigid** a displacement characterized by a deformation that can be expressed through a combination of different poloidal numbers m. This non-rigid displacement could thus be the cause of the Edge Localized Modes. At the separatrix, perturbations grow on the Alfvén time-scale, which is indeed a very fast rate and way shorter than the time response of external feedback stabilization systems. Furthermore, it has been observed experimentally that at plasma's boundary a current sheet always form, and its presence influence the stability of the perturbed system. We will see that current sheets forming on plasma's edge will affect plasma's behavior in different ways, depending on the scenario.

4.3 Heuristic model

In this section we present the heuristic model, derived in [12], in order to understand the instability mechanism, driven by current sheet forming on plasma's boundary. An important result will also be posed under our attention, related to the current

[1]Figure from "Analytic theory of ideal-MHD vertical displacements in tokamak plasmas", A. Yolbarsop, F. Porcelli, W. Liu, R. Fitzpatrick

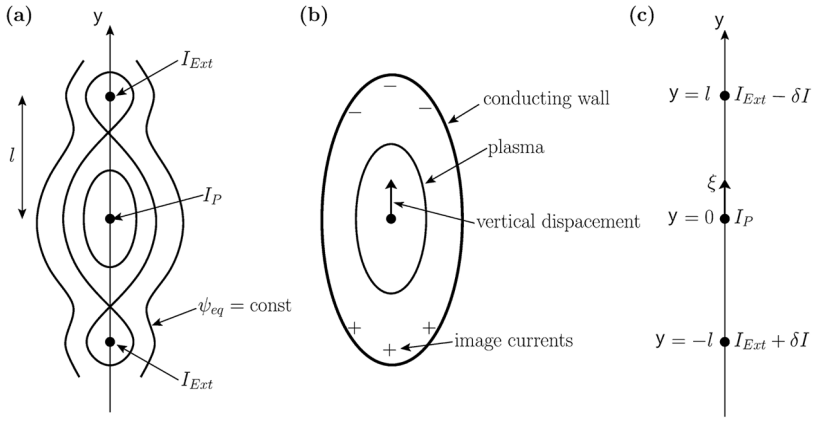

FIGURE 4.2: Schematic of the heuristic model for vertical instability [1]

profile, that will be essential for the following sections.
In figure 4.2(a) are shown three wires, with current flowing on the z direction, outside of the sheet and perpendicular to the reader. The central wire, with current I_P, represents the plasma current and is in equilibrium at $y = 0$, while the other two external wires I_{Ext} are used to create the magnetic field for a divertor configuration. The external wires are fixed in space, while the plasma wire is free to move along the y direction. This configuration mimics the straight tokamak configuration, with the (important) exception that here no current are allowed to flow on the plasma's boundary.
The equation of motion for the plasma wire is (in c.g.s. units):

$$\mu\ddot{y} = \frac{4I_P I_{Ext}}{c^2}\frac{y}{l^2 - y^2} \tag{4.2}$$

where μ is the linear mass density, c is the speed of light, and an over-dot signifies the time derivative. We neglect self and mutual induction currents. Thus, I_P and I_{Ext} remain constant as the plasma wire is displaced. For small $y \ll l$, the solution of equation 4.2 is:

$$y = y_0 e^{\gamma_H t} \tag{4.3}$$

where y_0 is an initial displacement, and

$$\gamma_H = \frac{1}{l}\sqrt{\frac{4I_P I_{Ext}}{\mu c^2}} \tag{4.4}$$

is an inertial growth rate.
At this stage, no particular relation exists between the currents I_P and I_{Ext} and the distance l. However, if instead of a plasma wire we consider a diffused plasma column with a uniform current density extending, on the Oxy cross-section, up to an elliptical magnetic surface with minor semi-axis a and major semi-axis b contained within the magnetic separatrix, called **convenient elliptical surface**,the growth rate of the vertical displacement becomes:

$$\gamma_H = \left(\frac{b-a}{a+b}\right)^{1/2}\left(\frac{1}{a^2+b^2}\right)^{1/2}\frac{2I_P}{(\mu c^2)^{1/2}} \tag{4.5}$$

Therefore, the relevant growth rate depends only on the plasma current I_P and

on the parameters a and b but does not depend on the distance l, nor on the value of the external currents. This is an important concept in order to set the current profile in the realistic model of the next section.
Introducing the ellipticity parameter:

$$e_0 = \frac{b^2 - a^2}{b^2 + a^2} \tag{4.6}$$

If we assume e_0 to be small, the growth rate is expressed as

$$\gamma_H = \frac{e_0^{1/2} V_A}{a} \tag{4.7}$$

where $V_A = B_{p(a)}/(4\pi\rho_m)^{1/2}$ is the Alfvén velocity based on the poloidal magnetic field, with ρ_m the volume mass density. The inverse of γ_H for a hydrogen plasma is $\gamma_H^{-1} \approx 1\mu s$. This is indeed a very fast growth time, of the order of the characteristic Alfvén time.
This instability behavior, together with γ_H value, agree with those obtained by the more detailed normal mode analysis of the next section. This result is no longer valid when plasma boundary will be extended up to the separatrix, where current sheets through X-points will be triggered, influencing the behavior of the plasma stability.
One final consideration can be made if we place a perfectly conducting wall near plasma's boundary. In this way, when the plasma current is displaced from its equilibrium position, image currents are induced at the wall, as shown in figure 4.2(b). The sign of these currents is such that the corresponding forces oppose the motion of the plasma wire, thus producing a stabilizing effect on plasma, that will result in a oscillatory motion with a characteristic frequency:

$$\omega_H = \pm\sqrt{D-1}\gamma_H$$

where D is a dimensionless proportionality constant, depending on the wall geometry and being $D \gg 1$ for a stable plasma.

4.4 Realistic models

Carrying with use the important result related to the current profile independence for the plasma growth rate, it is possible to set up a more realistic model starting from its equilibrium conditions. We will first describe the model's parameters and how the the equilibrium equations describing the system will be linearized with the introduction of a first order perturbation. Then the first scenario, where plasma is confined inside an elliptical flux surface, will be described and then the results from the second one will be illustrated, in order to set up the ground for the next chapters.

4.4.1 Plasma equilibrium

The model that will be adopted is the standard reduced ideal MHD model, where reduction is based on the low-β tokamak ordering, remembering that β = (plasma pressure)/(magnetic pressure).
We will now identify two important quantities, through which plasma is described: the magnetic flux function, denoted as ψ and the stream function, written as ϕ. The magnetic field is composed by the usual union of a toroidal component, $B_z\boldsymbol{e}_z$, created by currents flowing in external coils, and a poloidal component, written as $\boldsymbol{B}_p =$

$\boldsymbol{e}_z \times \nabla\psi$, thus the overall magnetic field is:

$$\boldsymbol{B} = \boldsymbol{e}_z \times \nabla\psi + B_z \boldsymbol{e}_z \tag{4.8}$$

, while the plasma flow is

$$\boldsymbol{v} = \boldsymbol{e}_z \times \nabla\phi \tag{4.9}$$

We assume that all the quantities are independent of the z coordinate and the toroidal magnetic field is nearly constant.
Space and time are here normalized as $\hat{r} = r/r_0$, where

$$r_0 = [2a^2b^2/(a^2+b^2)]^{1/2} \tag{4.10}$$

is an equilibrium scale length and $\hat{t} = t/\tau_A$, where $\tau_A = (4\pi\rho_m)^{1/2}/B_p'$ is the relevant Alfvén time and B_p' the radial derivative of the poloidal magnetic field at the magneitc axis. The dimensionless fields are normalized as $\hat{\psi} = \psi/(B_p' r_0^2)$, $\hat{\phi} = \phi(\tau_A/r_0^2)$; the normalized plasma density is $\hat{\rho} = \rho_m/\rho_{m0}$, with ρ_{m0} the density on the magnetic axis. In order to simplify the notation over-hats are dropped in the following.
Referring to [10], the reduced ideal-MHD equations are written as

$$\frac{\partial\psi}{\partial t} + [\phi, \psi] = 0 \tag{4.11}$$

$$\frac{\partial}{\partial t}\nabla\cdot(\rho\nabla\phi) + \frac{1}{2}[\rho, (\phi)^2] + U[\phi, \rho] + [\phi, U] = [\psi, \boldsymbol{J}] \tag{4.12}$$

where the bracket notation defines $[\chi, \eta] = \boldsymbol{e}_z \cdot \nabla\chi \times \nabla\eta$, with χ and η two generic scalar fields. The other parameters are: ρ is non-constant mass density, $\boldsymbol{J} = \nabla^2\psi$ is the normalized current density and $U = \nabla^2\phi$ is the normalized flow vorticity.
Based on definition given in the previous chapter, at equilibrium fields are time independent and plasma flows are absent, thus equations 4.11 and 4.12 are reduced as

$$[\psi_{eq}, \boldsymbol{J}_{eq}] = 0 \tag{4.13}$$

The general solution of 4.13 satisfies:

$$\boldsymbol{J} = \boldsymbol{J}_{eq}(\psi_{eq}) = \nabla^2\psi_{eq} \tag{4.14}$$

One of the important results of the heuristic model, is that vertical instability does not depend on details of the equilibrium current density profile, $\boldsymbol{J}_{eq}$, but on the finite ellipticity, e_0, and on the total current carried by plasma, $\boldsymbol{I}_P$. Therefor is better to choose a flat equilibrium current density profile, such that all the plasma current is uniformly distributed within a region delimited by the convenient elliptical surface. This surface, corresponding to $\mu = \mu_b$, is a special surface since it is the only elliptical surface that is also a flux surface; in fact, constant flux surfaces are not represented by confocal ellipses, exception made for $\mu = \mu_b$.
The equilibrium current can be defined as $\boldsymbol{J}_{eq} = 2H(\mu_b - \mu)$, where H is the Heaviside unit step function (see Appendix A). The area of this region is $S = \pi ab$, hence $\boldsymbol{I}_P = \pi ab\boldsymbol{J}_{eq}$. Because the equilibrium current is a function of ψ and satisfies equation 4.14, we can also take $\boldsymbol{J}_{eq} = 2H(\psi_b - \psi_{eq})$, where ψ_b is the value of the equilibrium flux at the convenient elliptical surface, $\mu = \mu_b$. Analytic work is better performed by using elliptical coordinates. The usual Cartesian coordinates can then

be expressed as

$$x = A\sinh(\mu)\cos(\theta); \qquad y = A\cosh(\mu)\sin(\theta), \tag{4.15}$$

with $A = \sqrt{b^2 - a^2}$; a and b correspond to the two semi-axis of the convenient elliptical surface, $\mu = \mu_b$, and are expressed as $a = A\sinh(\mu_b)$, $b = A\cosh(\mu_b)$.
For $\mu < \mu_b$, the solution of $\nabla^2\psi^-_{eq} = 2$ that satisfies the regularity condition at the magnetic axis, and that reduces to a constant at the flux surface $\mu = \mu_b$, in Cartesian coordinates is given by:

$$\psi^-_{eq}(x,y) = \frac{1}{2}\left(\frac{x^2}{2} + \frac{y^2}{2}\right) \tag{4.16}$$

(This conditions and solutions of this equilibrium are derived in [paper citation]. Here, and in the following, we take the subscript "$-$" to indicate the representation of scalar fields in the region inside the convenient elliptical surface. In this region, the equilibrium magnetic flux surfaces are nested ellipses with constant elongation, $k = b/a$. As we stated above, confocal ellipses with $\mu = const$ are not flux surfaces, except for the special one corresponding to $\mu = \mu_b$.
For $\mu > \mu_b$, the solution of the vacuum equation $\nabla\psi^+_{eq} = 0$, subject to the boundary conditions that the equilibrium magnetic flux $\psi_{eq}(\mu,\theta)$ and its normal derivative $\partial\psi_{eq}/\partial n = \boldsymbol{n}\cdot\nabla\psi_{eq}$ be continuous across the surface $\mu = \mu_b$, is best obtained in elliptical coordinates:

$$\psi^+_{eq} = \frac{1}{2} + \alpha^2\{\mu - \mu_b + \frac{1}{2}e_0\sinh[2(\mu-\mu_b)]\cos(2\theta)\}, \tag{4.17}$$

with $\alpha^2 = ab/r_0^2 = (1-e_0^2)^{-1/2}$. The subscript "$+$" indicates the representation of scalar fields in the region outside the convenient elliptical surface. The special flux surface defined by $\psi_{eq} = \psi_X = \mu_b\alpha^2$ is the magnetic separatrix, with X-points located at $\mu = \mu_X = 2\mu_b, \theta = \theta_X = (\pm\pi/2)$.

4.4.2 Linearization

We want now to normalize the equations of our model, in order to properly conduct an analysis when the plasma is weakly perturbed. This is done by introducing a small perturbation in the flux function and in the stream function equilibrium quantities trough a first order term. Any perturbation of plasma can be stable or unstable, as described in the previous chapter.
The general solution can be expressed throw an equilibrium term and an exponential one, as

$$\psi(\mu,\theta,t) = \psi_{eq}(\mu,\theta) + \tilde{\psi}(\mu,\theta)e^{\gamma t} \tag{4.18}$$

$$\phi(\mu,\theta,t) = \tilde{\phi}(\mu,\theta)e^{\gamma t} \tag{4.19}$$

, where the $\tilde{\psi}$ and $\tilde{\phi}$ represent perturbed functions.
Using first order perturbed quantities 4.18 inside equation 4.11 and 4.12, we obtain the linearized model

$$\gamma\tilde{\psi} + [\tilde{\phi}, \psi_{eq}] = 0 \tag{4.20}$$

$$\gamma\nabla\cdot(\rho_{eq}\nabla\tilde{\phi}) = [\tilde{\psi}, \boldsymbol{J}_{eq}] + [\psi_{eq}, \tilde{\boldsymbol{J}}] \tag{4.21}$$

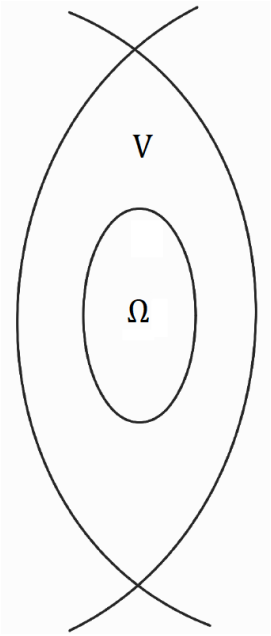

FIGURE 4.3: Equilibrium magnetic structure for the limiter tokamak scenario

4.4.3 Limiter tokamak scenario

In this section we present the results produced by the stability analysis in the scenario where the plasma boundary is extended up to the convenient elliptical region, $\mu = \mu_b$. In figure 4.3 it is shown a section of the plasma, where Ω indicates the region within which plasma is confined and V the vacuum region surrounding plasma.

To find a solution we first simplify equation 4.21, by assuming that the vorticity $\nabla^2\tilde{\phi}$ vanishes. Furthermore, we are now considering Ω region without its boundary, that means we have no variation of the equilibrium current due to the assumption of a flat current distribution, leading to $[\tilde{\psi}, \boldsymbol{J}_{eq}]$ being zero. The perturbed flux now satisfies

$$[\psi_{eq}, \tilde{\boldsymbol{J}}] = 0, \tag{4.22}$$

where two possibilities now arise. The first one is that $\tilde{\boldsymbol{J}} = \tilde{\boldsymbol{J}}(\psi_{eq})$, while the other one is that $\tilde{\boldsymbol{J}} = 0$. To avoid additional calculations the second case is considered. Making use of elliptical coordinates the final expression is now written as

$$\nabla^2\tilde{\psi}^- = h^{-2}(\partial_\mu^2 + \partial_\theta^2)\tilde{\psi}^- = 0 \tag{4.23}$$

where $h = |\nabla\mu| = |\nabla\theta|$ is the metric element to pass from Cartesian to elliptical coordinates. We have also make use here, and in the following, of the short-hand notation $\partial_\mu = \frac{\partial}{\partial\mu}$.
From [6] it is known that the general solution for 4.23 can be written as a summation, over odd numbers of product of exponential functions of $m\mu$ and sinusoidal functions of $m\theta$. In this same paper has also been demonstrated that the most dangerous mode is the one corresponding to $m = 1$, that is odd in θ and even in μ. Our solution will be then

$$\tilde{\psi}^- = \psi_1 A \cosh(\mu)\sin(\theta) = \psi_1 y, \tag{4.24}$$

where ψ_1 is a constant amplitude. Using equation 4.20 in Cartesian coordinates

$$\gamma\tilde{\psi} + \frac{y}{b^2}\partial_x\tilde{\phi} - \frac{x}{a^2}\partial_y\tilde{\phi} = 0 \tag{4.25}$$

Using solution 4.27 we find

$$\tilde{\phi}^- = \gamma\xi A\cosh(\mu)\sin(\theta) = \gamma\xi x, \tag{4.26}$$

where we have introduced the constant displacement amplitude ξ, and $\psi_1 = \xi/b^2$. Since $\nabla^2\tilde{\psi} = 0$ the initial assumption of vanishing vorticity is satisfied. Solution 4.24 can be rewritten as

$$\tilde{\psi}^-(\mu,\theta) = -\frac{\xi}{b}\frac{\cosh(\mu)}{\cosh(\mu_b)}\sin(\theta) \tag{4.27}$$

Furthermore, the perturbed solution 4.26 correspond to a rigid shift in the vertical direction, as the one observed in the previous chapter with the heuristic model. It has been widely demonstrated and observed experimentally, that a current sheet always form at plasma's boundary. At the elliptical boundary, $\mu = \mu_b$, the perturbed solutions for the magnetic flux must respect the continuity condition, in fact $\tilde{\psi}^+(\mu_b,\theta) = \tilde{\psi}^-(\mu_b,\theta) = -\xi/b\sin(\theta)$, see next section for $\tilde{\psi}^+(\mu,\theta)$ solution. The same is not true for their derivative, this discontinuity gives rise to the current sheet at the elliptical boundary, expressed as

$$\tilde{\boldsymbol{J}}(\mu,\theta) = \tilde{j}_b(\theta)\delta(\mu-\mu_b) = h^{-2}\left(\partial_\mu\tilde{\psi}^+ - \partial_\theta\tilde{\psi}^-\right)_{\mu_b}\delta(\mu-\mu_b), \tag{4.28}$$

where $\delta(x)$ is the Dirac delta function (Appendix B). Considering the metric element as $h^2(\mu,\theta) = A^2(\cosh(2\mu)+\cos(2\theta))/2$, the term $\tilde{j}_b(\theta)$ is then expressed as

$$\tilde{j}_b(\theta) = \frac{2(a+b)}{b^2(a^2+b^2)}\frac{\xi\sin(\theta)}{1+e_0\cos(2\theta)} \tag{4.29}$$

Considering now the equation of motion 4.21 we can see how all of the three terms contain the delta function $\delta(\mu-\mu_b)$, so it is possible to integrate over a narrow layer of infinitesimal width at the elliptical boundary. Multiplying by h^2 and integrating we have

$$\lim_{\delta\mu\to0}\int_{\mu_b-\delta\mu}^{\mu_b+\delta\mu} h^2\gamma\nabla\cdot(\rho\nabla\tilde{\phi})\,d\mu = \lim_{\delta\mu\to0}\left\{\int_{\mu_b-\delta\mu}^{\mu_b+\delta\mu} h^2[\tilde{\psi},\boldsymbol{J}_{eq}]\,d\mu + \int_{\mu_b-\delta\mu}^{\mu_b+\delta\mu} h^2[\psi_{eq},\tilde{\boldsymbol{J}}_{eq}]\,d\mu\right\} \tag{4.30}$$

The l.h.s of 4.30 is solved as

$$\lim_{\delta\mu\to0}\int_{\mu_b-\delta\mu}^{\mu_b+\delta\mu} h^2\gamma\nabla\cdot(\rho\nabla\tilde{\phi})\,d\mu = \tag{4.31}$$

$$= \gamma\lim_{\delta\mu\to0}\int_{\mu_b-\delta\mu}^{\mu_b+\delta\mu}\{\partial_\mu(\rho\partial_\mu\tilde{\phi}) + \partial_\theta(\rho\partial_\theta\tilde{\phi})\}\,d\mu = \tag{4.32}$$

$$= -\gamma\rho(\partial_\mu\tilde{\phi})_{\mu_b^-} \tag{4.33}$$

The first integral on the r.h.s is instead

$$\lim_{\delta\mu\to 0}\int_{\mu_b-\delta\mu}^{\mu_b+\delta\mu} h^2[\tilde{\psi}, \boldsymbol{J}_{eq}]\, d\mu = \tag{4.34}$$

$$= \lim_{\delta\mu\to 0}\int_{\mu_b-\delta\mu}^{\mu_b+\delta\mu} h^2\nabla\cdot(J_{eq}\boldsymbol{e_z}\times\nabla\tilde{\psi})\, d\mu = J_{eq}(\partial_\theta\tilde{\psi}^-_{\mu_b}) \tag{4.35}$$

While the last one is

$$\lim_{\delta\mu\to 0}\int_{\mu_b-\delta\mu}^{\mu_b+\delta\mu} h^2[\psi_{eq}, \tilde{\boldsymbol{J}}]\, d\mu = \tag{4.36}$$

$$= \lim_{\delta\mu\to 0}\int_{\mu_b-\delta\mu}^{\mu_b+\delta\mu} h^2\nabla\cdot(\tilde{\boldsymbol{J}}\boldsymbol{e_z}\times\nabla\psi_{eq})\, d\mu = \tag{4.37}$$

$$= \frac{d}{d\theta}\left[\tilde{j}_{b(\theta)}(\partial_\mu\psi_{eq})_{\mu_b}\right] \tag{4.38}$$

In all these integrals the bracket term has been transformed as

$$\begin{aligned}[\chi,\eta] &= \boldsymbol{e}_z\cdot\nabla\chi\times\nabla\eta \\ &= \nabla\cdot[(\boldsymbol{e}_z\times\nabla\chi)\nabla\eta]\end{aligned} \tag{4.39}$$

Balancing the three terms

$$-\gamma\frac{\partial\tilde{\phi}}{\partial\mu}\bigg|_{\mu_b} = \boldsymbol{J}_{eq}\frac{\partial\tilde{\psi}^-}{\partial\theta}\bigg|_{\mu_b} + \frac{d}{d\theta}\left[\tilde{j}_b(\theta)\frac{\partial\psi_{eq}}{\partial\mu}\bigg|_{\mu_b}\right] \tag{4.40}$$

Computing each of these three terms leads to a proportionality factor of $\cos(\theta)$ on both sides of the equality. Substituting then the expressions for $\tilde{\phi}$ and $\tilde{\psi}$ the dispersion relation is obtained, written as

$$\gamma^2 = (1-e_0)\left(1+e_0-\sqrt{1-e_0^2}\right)\tau_A^{-2} \tag{4.41}$$

with the ellipticity parameter $0 \le e_0 \le 1$. In the limit of small ellipticity, the growth rate reduces to $\gamma \approx e_0^{1/2}\tau_A^{-1}$, in full agreement with the heuristic case of the previous chapter, and for any arbitrary value of e_0 the plasma results in an unstable behavior.

4.4.4 Divertor tokamak scenario

In this section are presented the most important results for the more realistic case where the plasma boundary is extended up to the magnetic separatrix, i.e. the last closed magnetic surface, $u = u_X$. A uniform density profile is assumed, dropping to zero at the separatrix, $\rho_{eq}(\psi_{eq}) = H(\psi_X - \psi_{eq})$. While for the current the same profile is adopted, expressed as $J_{eq} = 2H(\psi_b - \psi_{eq})$. Figure 4.4 shows regions Δ and Ω where plasma is contained (current only flowing through Ω). V-regions represent the different vacuum zones, while u and v will be explained in a moment.
The solutions valid in this case are:

- Rigid shift solution 4.26 valid up to the magnetic separatrix
- The perturbed flux 4.27 is still valid but only in region Ω, since in region Δ, the flux ψ_{eq} takes a different form

[2]Figure from "Analytic theory of ideal-MHD vertical displacements in tokamak plasmas", A. Yolbarsop, F. Porcelli, W. Liu, R. Fitzpatrick

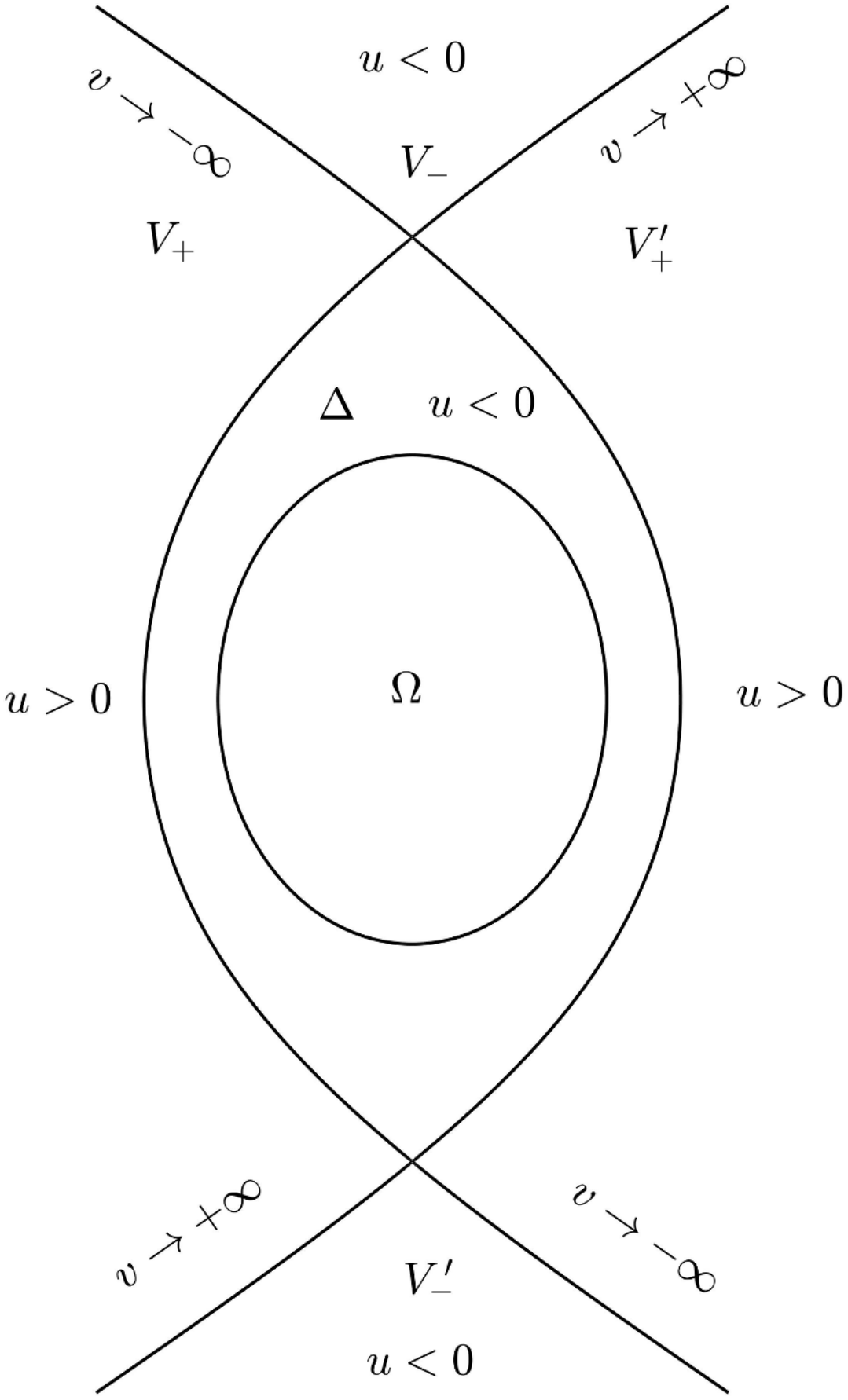

FIGURE 4.4: Equilibrium magnetic structure [2]

This latter can be expressed, inside region Δ, in elliptical coordinates as

$$\tilde{\psi}_\Delta(\mu,\theta) = \frac{\xi}{b}\frac{\sinh(\mu - 2\mu_b)}{\sinh(\mu_b)}\sin(\theta) \tag{4.42}$$

While in vacuum region as

$$\tilde{\psi}_V(\mu,\theta) = \frac{\xi}{b}\sum_{m,odd}^{\infty} g_m e^{-m(\mu-\mu_b)}\sin(m\theta) \tag{4.43}$$

The coefficients g_m will be evaluated later on, for now we only express this last solution using more convenient coordinates, in order to simplify calculations.
We here introduce flux coordinates, the ones represented in figure 4.4, defined as

$$u = \alpha^{-2}[\psi^+_{eq}(\mu,\theta) - \psi_X] \tag{4.44}$$

$$\nu = \theta - \frac{\pi}{2} + \frac{e_0}{2}\cosh[2(\mu-\mu_b)]\sin(2\theta) \tag{4.45}$$

where ψ^+_{eq} is given by 4.17. The set of (u,ν) coordinates is harmonic and orthogonal in regions Δ and $V_\pm$, satisfying $\nabla^2 u = 0$ and $\partial_\theta u = -\partial_\mu \nu$; but inside region Ω this orthogonality doesn't hold anymore. The convenient elliptical boundary, that we remember has the special characteristic of being also a flux surface, corresponds to $(u = u_b, \nu)$, or $(u = -\mu_b + (e_0/2)\sinh(2\mu_b), \nu = \theta - \frac{\pi}{2} + \frac{e_0}{2}\sin(2\theta))$. While the separatrix corresponds to coordinates $(u = 0, \nu)$ and the X-points to $(u = 0, \nu = \{0, \pm\pi\})$.
With these coordinates the solution 4.43 is expressed as

$$\tilde{\psi}_V(\mu,\theta) = \frac{\xi}{b}\sum_{m,odd}^{\infty}\{a_m e^{-mu} + b_m e^{mu}\}\cos(m\nu) \tag{4.46}$$

where a_m and b_m are fully determined by:

$$a_m = -\frac{e^{mu_b}}{2m}\sum_{j=\pm1}\left(\frac{b}{a}+j\right)J_{\frac{m-j}{2}}\left(\frac{me_0}{2}\right) \tag{4.47}$$

$$b_m = \frac{e^{-mu_b}}{2m}\sum_{j=\pm1}\left(\frac{b}{a}-j\right)J_{\frac{m-j}{2}}\left(\frac{me_0}{2}\right) \tag{4.48}$$

with $J_v(x)$ the first order Bessel functions, see appendix C.
If we expand the vacuum solution in the different V-regions from figure 4.4, it is possible to obtain the asymptotic relations for the perturbed flux in all of the four zones surrounding the X-points. The perturbed current density along the separatrix, in the vicinity of the X-points, can be determined from

$$\tilde{\boldsymbol{J}}(u,\nu) = |\nabla u|^2(\partial_u^2 + \partial_\nu^2)\tilde{\psi} \tag{4.49}$$

Since the current sheet vanishes everywhere except on the separatrix, 4.49 can be expressed through the Dirac delta as

$$\tilde{\boldsymbol{J}}(u,\nu) = j_X(\nu)\delta(u) \tag{4.50}$$

Expanding $j_X(\nu)$ near the X-point, and then integrating again equation 4.21 over a narrow layer around $u = 0$ gives the final dispersion relation

$$\gamma^2 = -2\sqrt{\frac{\pi a}{2b}}\left(q + \frac{p}{2}\right)(1 - e_0^2)^{1/2} e_0^{3/2} \omega_A^2 \tag{4.51}$$

where $\omega_A = \tau_A^{-1}$. For the solution where $q = -p/2$, the $n = 0$ mode is neutrally stable with $\gamma = 0$ and no current sheet develops at the magnetic separatrix. This solution can be considered merely as a redefinition of the equilibrium, with the current-carrying plasma shifted vertically by a distance ξ and the equilibrium current density modified by current sheets located at the elliptical flux surface $\mu = \mu_b$. Instead, for the solution $q = +p/2$, a current sheet develops at the separatrix and is sufficient to neutrally stabilize the $n = 0$ mode, which in this case oscillates with a real frequency:

$$\omega = \pm i\gamma \tag{4.52}$$

Thus, we have shown that when plasma is extended up to the separatrix, the instability of the first scenario is no more present and the system becomes indeed stable, oscillating with a finite natural frequency. This passive stabilization effect can be justified by considering the nature of the current sheets forming along the separatrix. We will return more specifically over this balancing aspect in the next chapters.

Chapter 5

Perturbed solutions harmonics analysis

In the previous chapter has been shown that the stability behavior of plasma changes from unstable, when it is constrained inside the elliptical surface $u = u_b$, to stable, when plasma's boundary is instead extended up to the magnetic separatrix, $u = u_x$. The reason behind this change in stability is that the current sheets localized along the last magnetic closed surface have the same effect of a passive stabilization device.
With this background, it is reasonable to conjecture the existence of a generic flux surface, $u = u_c$, located between u_b and the separatrix u_x, such that when plasma is slightly perturbed nothing happens, and so where marginal stability occurs. Thus, we want to find the surface, which will be called from now on **marginal stability surface** or **marginal stability flux surface**, where the growth rate is zero, $\gamma = 0$. The first steps to solve this problem will be illustrated in chapter 6, while here, a more accurate analysis of the perturbed solutions in region Δ, see figure 5.1, will be performed. In particular on the behavior of the different odd harmonics of the perturbed flux solution, $\tilde{\psi}(u_c, \nu)$, for the case where plasma's boundary is confined inside a generic flux surface, $u = u_c$, located inside the two main cases of the previous chapter, i.e. $u_b < u_c < u_X$.

5.1 Analysis of Δ region

In figure 5.1 is represented region Δ, which is now located between the elliptical surface (contour of region Ω), and region V', that is the vacuum region between the plasma boundary $u = u_c$ and the magnetic separatrix. We have basically made a step back w.r.t. the previous chapter, where region Δ was instead extended up to the magnetic separatrix, u_X. We can still use solution 4.26 up to the flux surface u_c, while 4.27 is only valid inside In region Ω. For region Δ we can keep on using solution 4.42.
To perform calculations more easily, flux coordinates introduced in chapter 4 will be used. Thus the solution for the perturbed flux in region Δ, $\tilde{\psi}_\Delta$ is given by:

$$\tilde{\psi}_\Delta(u, \nu) = \frac{\xi}{b} \sum_{m,odd}^{\infty} [a_m e^{-mu} + b_m e^{mu}] \cos(m\nu) \tag{5.1}$$

[1]Figure from "Analytic theory of ideal-MHD vertical displacements in tokamak plasmas", A. Yolbarsop, F. Porcelli, W. Liu, R. Fitzpatrick

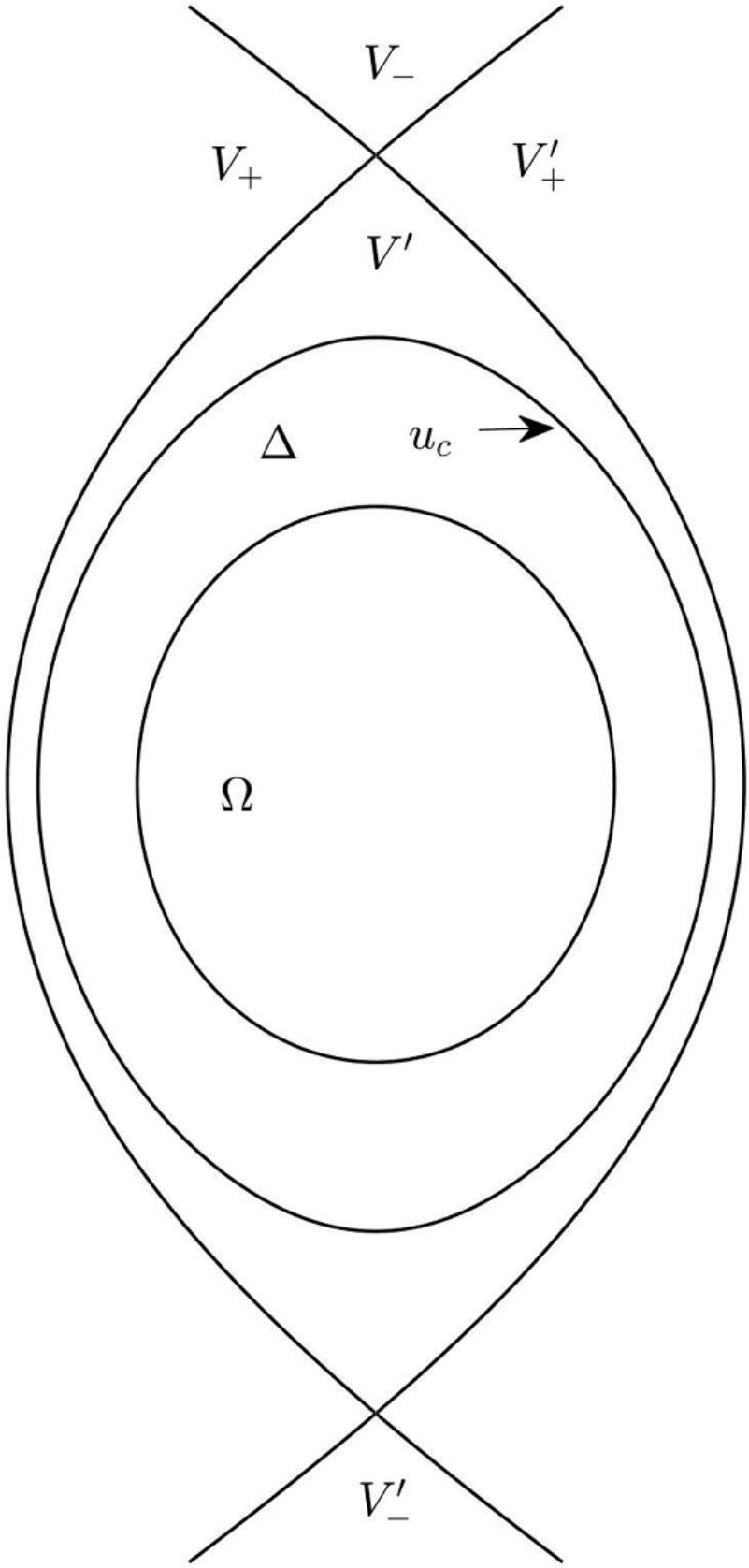

FIGURE 5.1: Equilibrium magnetic structure for the case where the plasma boundary, $u = u_c$, is located inside the separatrix [1]

Let's know identify as λ_m the coefficients, functions of $u = u_c$, as

$$\lambda_m(u_c) = a_m e^{-mu_c} + b_m e^{mu_c} \tag{5.2}$$

, where u_c is the generic flux surface contouring region Δ. On the plasma boundary $u = u_c$ the perturbed flux can thus be written in the more compact form as

$$\tilde{\psi}_\Delta(u_c, v) = \frac{\xi}{b} \sum_{m,odd}^{\infty} \lambda_m(u_c) \cos(mv) \tag{5.3}$$

The λ_m coefficients depend on the ellipticity parameter e_0. This dependence can also be expressed in terms of the convenient elliptical surface, which we recall here to be:

$$u_b = \alpha^{-2}[\psi^+_{eq}(\mu_b, \theta) - \psi_X] = \frac{\alpha^{-2}}{2} - \alpha^{-2}\psi_X$$

where $\psi_X = \mu_b \alpha^2$ and $\alpha^2 = (1 - e_0^2)^{-1/2}$. The relation between the ellipticity e_0 and u_b is then

$$u_b = \frac{(1 - e_0^2)^{1/2}}{2} - \mu_b \qquad \text{or} \qquad u_b = \frac{\tanh(2\mu_b)}{2} - \mu_b \tag{5.4}$$

We are going now to focus on the harmonics' behavior. The perturbed solution $\tilde{\psi}_\Delta(u_c, v)$ must be continuous inside region Δ, and the infinite series related to it must converge. Thus, considering the infinite converging series:

$$\sum_{m,odd}^{\infty} \{\lambda_{m(u_c)} \cos(mv)\} \tag{5.5}$$

then its coefficients, in our case λ_ms, tend to zero $(\lambda_m \to 0)$ as $m \to \infty$. Which is written also as

$$\lim_{m\to\infty} \lambda_m = 0 \tag{5.6}$$

This result can also be confirmed by their asymptotic behavior. The analytic derivation has been done in [12], and we report here the final result only, that is

$$\lambda_m \sim (p/m^{3/2}) e^{mu_c} \tag{5.7}$$

The Fourier spectrum extended up to $m_{max} \sim |u_c|^{-1}$, but since we don't know precisely which is the last term of the series to vanish, is reasonable to proceed to truncate the summation at a certain m_{max} value, and analyze if the terms of the series still represent an important contribution inside the odd terms summation or not.
Furthermore, since the number of harmonics of the perturbation goes as $\sim 1/|u_c|$ the solution thus becomes divergent at the X-points. This problem should be solved if a finite, not negligible, resistivity is instead taken into account.
Here below are shown the graphs representing in blue the Fourier coefficients from expression 5.2, for fixed values of $u = u_c$ and e_0, while in red the values obtained from the asymptotic formula 5.7. For $e_0 = 0.05$ we can see from 5.2, 5.5 and 5.8 that a good order to represent the important harmonics contribution is $3/|u_c|$, so will be taken as the maximum number for the series truncation in the case of $e_0 = 0.05$. Analyzing the series with $e_0 = 0.1$ this number is no more sufficient to correctly represent the approximated series, thus it is necessary to extend the series up to $m_{max} = 6/|u_c|$. For the last case, $e_0 = 0.2$, the truncation value is $m_{max} = 10/|u_c|$, as shown in figures 5.4, 5.7 and 5.10.

We can see how a larger value of the ellipticity e_0 means a larger number of harmonics needed to represent the perturbed solution for a given value of u_c.

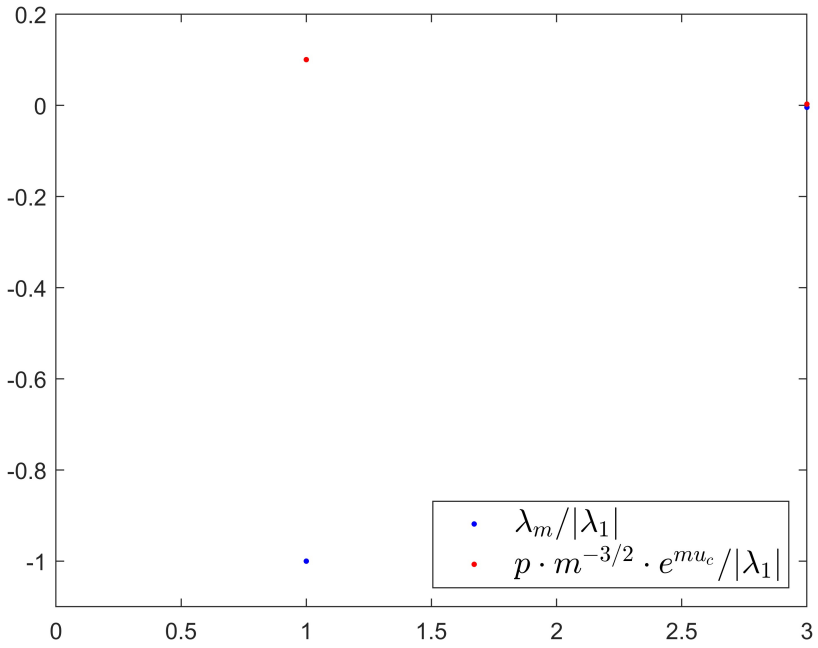

FIGURE 5.2: Lambda harmonics and its asymptotic behavior, for $e_0 = 0.05, u_c = -1.0$

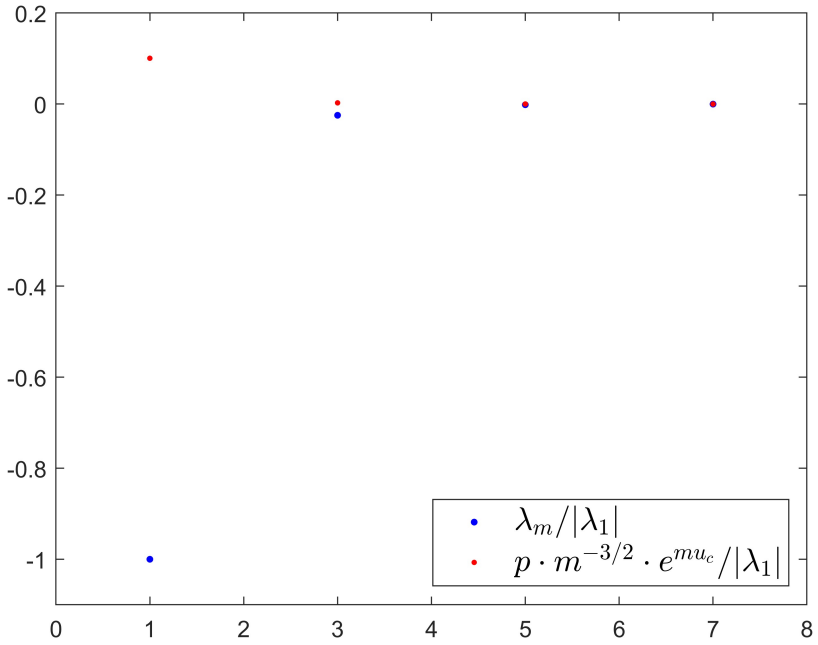

FIGURE 5.3: Lambda harmonics and its asymptotic behavior, for $e_0 = 0.1; u_c = -1.0$

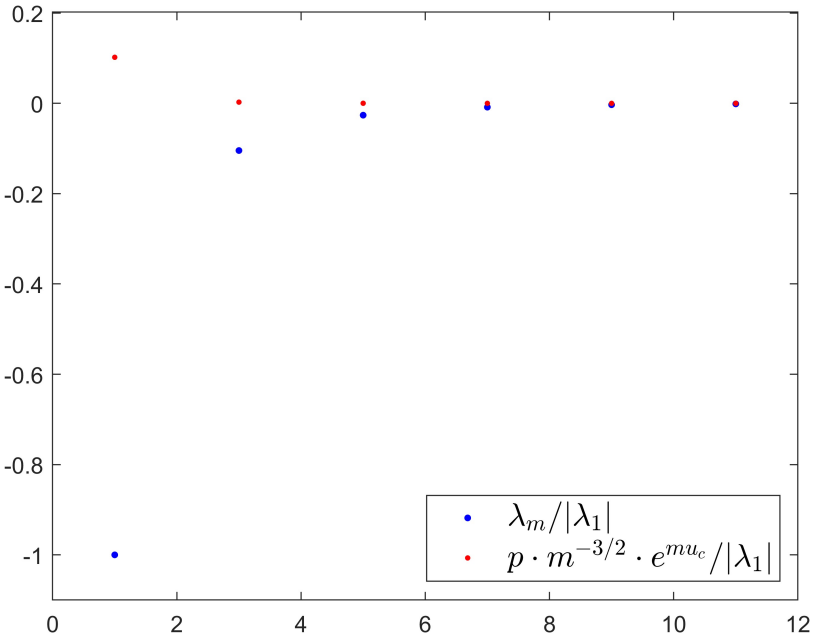

FIGURE 5.4: Lambda harmonics and its asymptotic behavior, for $e_0 = 0.2; u_c = -1.0$

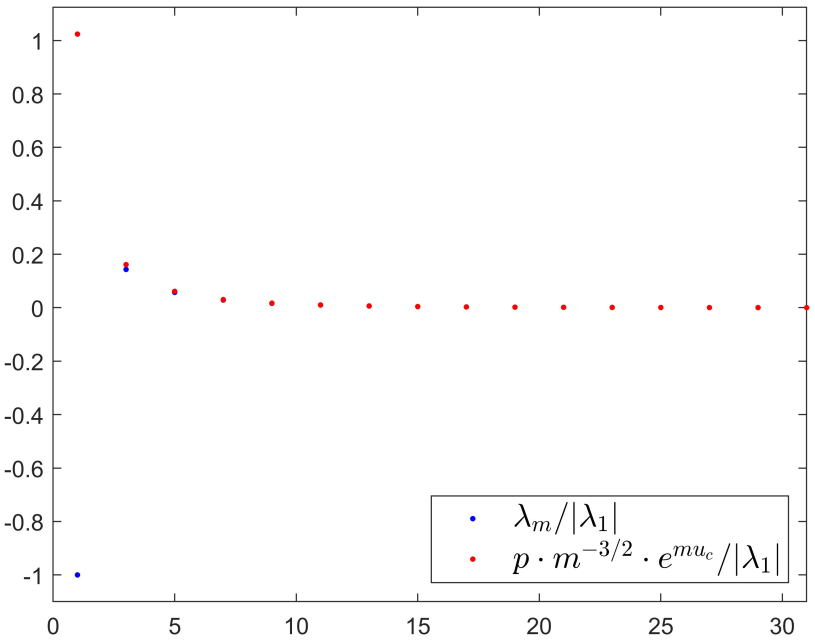

FIGURE 5.5: Lambda harmonics and its asymptotic behavior, for $e_0 = 0.05; u_c = -0.1$

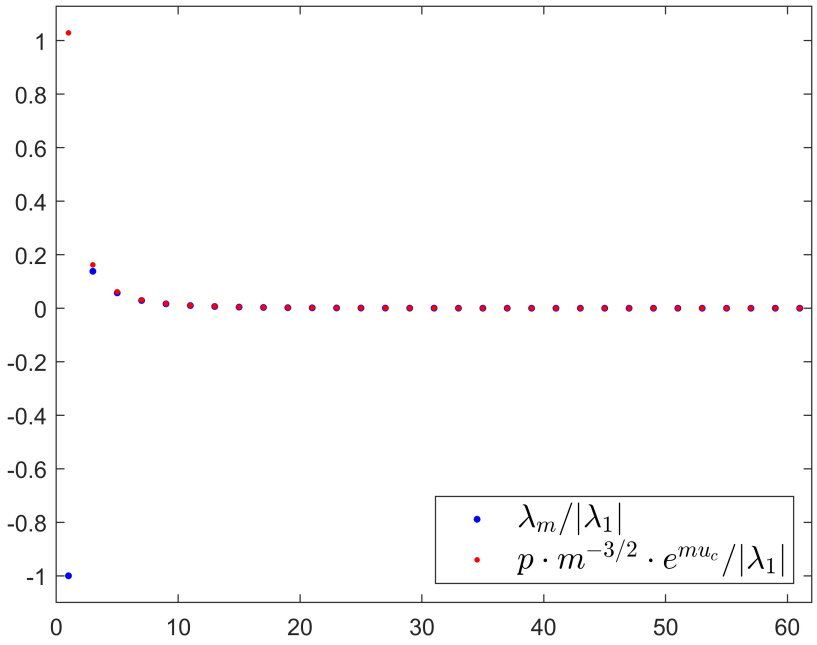

FIGURE 5.6: Lambda harmonics and its asymptotic behavior, for $e_0 = 0.1; u_c = -0.1$

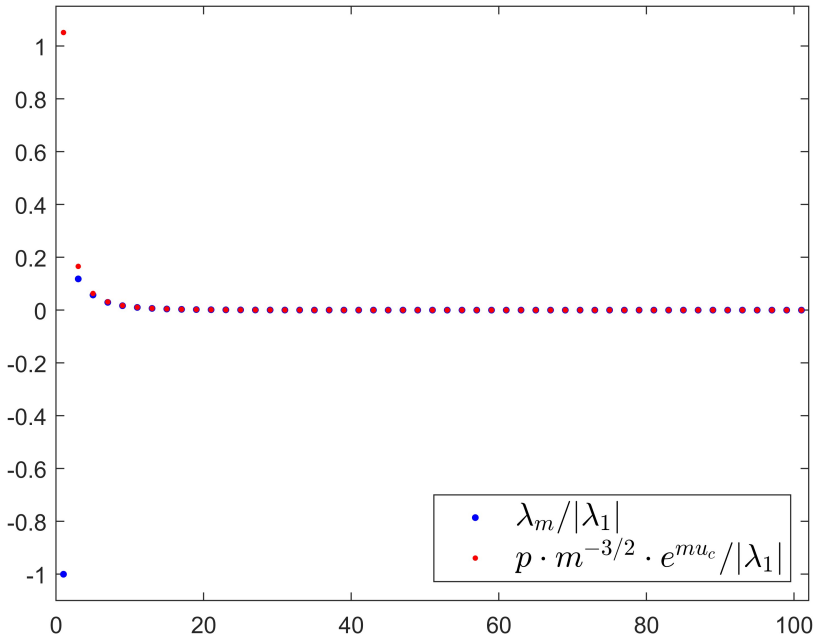

FIGURE 5.7: Lambda harmonics and its asymptotic behavior, for $e_0 = 0.2; u_c = -0.1$

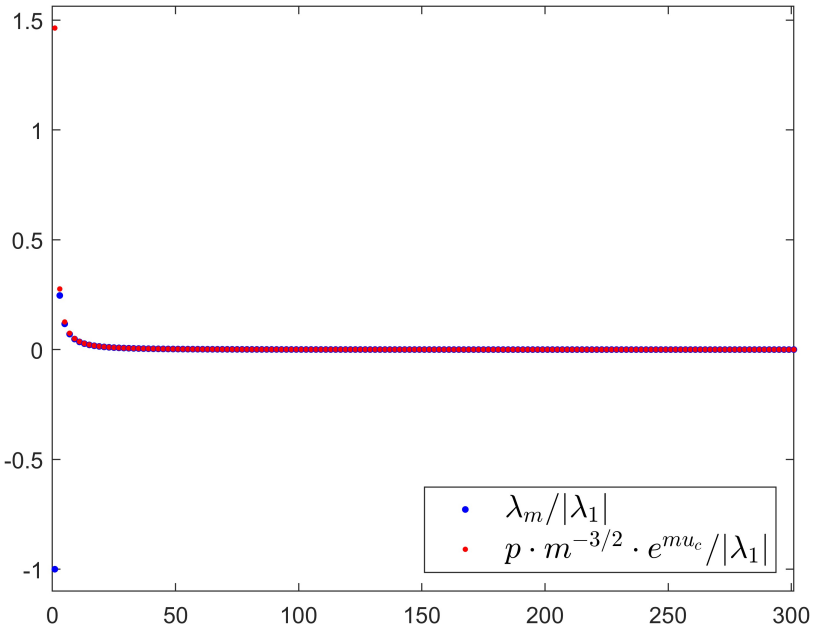

FIGURE 5.8: Lambda harmonics and its asymptotic behavior, for $e_0 = 0.05; u_c = -0.01$

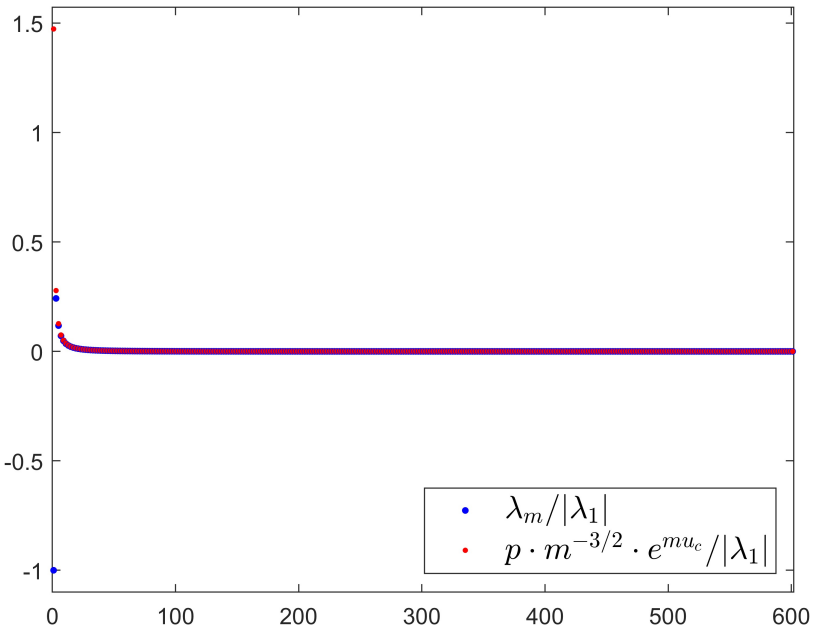

FIGURE 5.9: Lambda harmonics and its asymptotic behavior, for $e_0 = 0.1; u_c = -0.01$

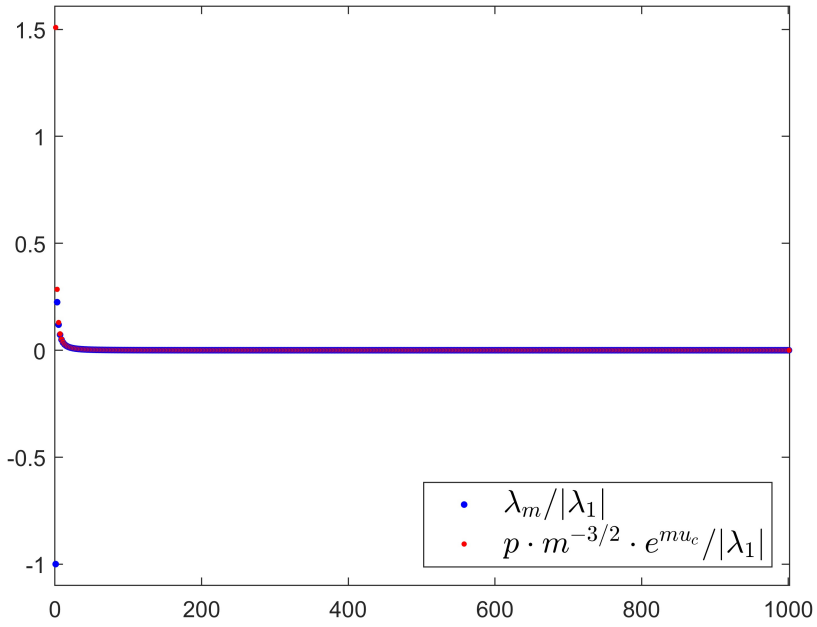

FIGURE 5.10: Lambda harmonics and its asymptotic behavior, for $e_0 = 0.2; u_c = -0.01$

As m increases the two type of points overlap each other, thus confirming the asymptotic behavior for λ_m, given by 5.7.
Following also the results presented in the previous chapter, related to the perturbed solutions 4.26 and 4.27, it is possible to conclude that for values of $|u_c| \geq 1$ the behavior of the perturbed stream and magnetic flux solutions are dominated by the first harmonic only in the coordinate ν, which can thus be approximated in the elliptical angle θ. For these values of $|u_c|$ has been analytically shown that the system ends up being ideal-MHD unstable, when an external source of stabilization is not present. When instead $|u_c| < 1$ more and more Fourier harmonics become important in the spectrum of $\tilde{\psi}_\Delta$, thus changing the nature of the dispersion relation.
This concept is the fundamental one of our analysis and the motivation behind this thesis. By increasing the number of harmonics in the Fourier spectrum the system arrive to be ideal-MHD stable at the separatrix, $u_c = 0$, also in the absence of a nearby conducting wall.
In the next chapter will see how the choice of the truncation value m_{max} will affects the numerical computation, in particular how this choice will result to be the base of a problem based on compromise, between accuracy and the minimum computable value of $u = u_c$ that can be achieved.

Chapter 6

δW analysis of vertical stability

This chapter will be devoted to the analysis of the perturbed potential energy δW, as a function of u_c, that has been introduced in chapter 4 together with the energy principle statement. This is the first step in the definition of the system that will be used in the next chapter for the computational procedure to find u_{marg}.

6.1 Energy principle for kink modes

In chapter 3 the Energy Principle has been introduced, which is a very powerful tool in order to study stability for an ideal-MHD plasma. In the general case the principle is stated with the use of trial functions, we are now going to use instead $\tilde{\psi}$ and $\tilde{\phi}$ as they are the actual solutions of the problem. Given the expression 3.37 for the perturbed energy, we can easily state that this expression for δW is quiet complicated in a general scenario, but is possible to simplify it in specific cases. Where are going to use here the expression for δW obtained by G. Laval, R. Pellat and J. S. Soule in [6], for the case of axysimmetric toroidal mode $n = 0$. The equation is derived by making use of the incompressibility condition, $\nabla \cdot \boldsymbol{\xi} = 0$, and of the equilibrium expansion of a low-β straight tokamak at the lowest order. The final expression is:

$$2\delta W = \int_\tau \left[\tilde{\boldsymbol{B}}^2 - \tilde{\boldsymbol{\xi}} \cdot \boldsymbol{J}_0 \times \tilde{\boldsymbol{B}}\right] d\tau \tag{6.1}$$

where τ identifies the region from the origin up to the external wall. This big region can be divide into three parts as shown in figure 6.1; J is the region inside the elliptical boundary, $u = u_b$, D is the region between the elliptical boundary and the generic flux surface, $u = u_c$, and E is the vacuum region between the generic surface and the magnetic separatrix. The energy expression is thus divided as follows:

$$\begin{aligned}\delta W &= \delta W_J + \delta W_D + \delta_E \\ &= \frac{1}{2}\int_J [\tilde{\boldsymbol{B}}^2 - \tilde{\boldsymbol{\xi}} \cdot \boldsymbol{J}_0 \times \tilde{\boldsymbol{B}}]\, dr^3 + \frac{1}{2}\int_D \tilde{\boldsymbol{B}}^2\, dr^3 + \frac{1}{2}\int_E \tilde{\boldsymbol{B}}^2\, dr^3\end{aligned}$$

In the last two integrals the contribution coming from the current is not present, because of the flat profile chosen in 4. Paying attention to the notation, we use here the subscript "$-$" for quantities inside region J, while for regions outside we use "$+$". We also use "in", in addition to "$+$", to express that we are working in region D, that lies inside the magnetic separatrix. While for the region outside of this latter, region E, we make use of "out" to identify the quantities.
Starting from region J, we have made use of $\boldsymbol{J}_0 = J_{eq}\boldsymbol{e_z}$, also we recall that inside Ω the relation $\nabla^2 J_{eq} = 2$ must hold, while the perturbed magnetic field is expressed as

$$\tilde{\boldsymbol{B}} = \boldsymbol{e_z} \times \nabla\tilde{\psi} \tag{6.2}$$

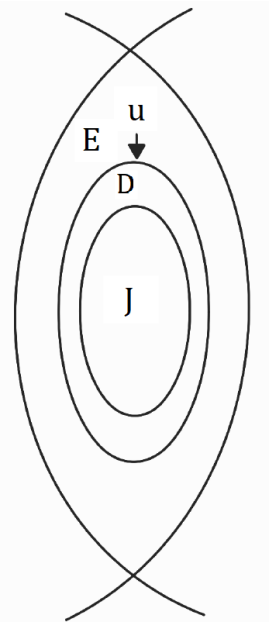

FIGURE 6.1: Regions inside the magnetic structure

Substituting everything inside the integral we arrive at:

$$\delta W_J = \frac{1}{2}\int_J [\tilde{\boldsymbol{B}}^2 - \tilde{\boldsymbol{\xi}} \cdot \boldsymbol{J}_0 \times \tilde{\boldsymbol{B}}]\, d\boldsymbol{r} \tag{6.3}$$

$$= -\frac{\pi}{2}\xi_1^2 \frac{\cosh(\mu_b)}{\sinh(\mu_b)} \tag{6.4}$$

where $\xi_1 = \xi/b$. In region D:

$$\begin{aligned}\delta W_D &= \frac{1}{2}\int_D \tilde{\boldsymbol{B}}^2\, d\boldsymbol{r} \\ &= \frac{1}{2}\int_D (\boldsymbol{e}_z \times \nabla\tilde{\psi}_{in}^+)^2\, d\boldsymbol{r} \\ &= \frac{1}{2}\int_D \nabla\cdot(\tilde{\psi}_{in}^+ \nabla\tilde{\psi}_{in}^+)\, d\boldsymbol{r}\end{aligned}$$

using Gauss divergence theorem we have

$$\begin{aligned}&= \frac{1}{2}\int_{S_D} \tilde{\psi}_{in}^+ \nabla\tilde{\psi}_{in}^+ \cdot\, d\boldsymbol{s} \\ &= -\frac{1}{2}\int_{\psi_b} \tilde{\psi}_{in}^+ \nabla\tilde{\psi}_{in}^+ \cdot\, d\boldsymbol{s} + \frac{1}{2}\int_{\psi_c} \tilde{\psi}_{in}^+ \nabla\tilde{\psi}_{in}^+ \cdot\, d\boldsymbol{s}\end{aligned}$$

where S_D is the surface around the elliptical boundary region. It's important to notice that $S_D = \psi_b + \psi_c$, where the last two are the flux surfaces at u_b and u_c.

In regione E:

$$\begin{aligned}\delta W_E &= \frac{1}{2}\int_E \tilde{\boldsymbol{B}}^2\, d\boldsymbol{r} \\ &= -\frac{1}{2}\int_{\psi_c} \tilde{\psi}^+_{out}\nabla\tilde{\psi}^+_{out}\cdot\, d\boldsymbol{s}\end{aligned}$$

The final expression for the perturbed energy outside the elliptical boundary is

$$\delta W_D + \delta W_E = -\frac{1}{2}\int_{\psi_b} \tilde{\psi}^+_{in}\nabla\tilde{\psi}^+_{in}\cdot\, d\boldsymbol{s} + \frac{1}{2}\int_{\psi_c}\left[\tilde{\psi}^+_{in}\nabla\tilde{\psi}^+_{in} - \tilde{\psi}^+_{out}\nabla\tilde{\psi}^+_{out}\right]\cdot\, d\boldsymbol{s} \tag{6.5}$$

The calculation for the first integral will be done using elliptical coordinate, while for the second one flux coordinates will be used. We start by rewriting the integral, knowing that a general change of coordinates transforms the gradient as

$$\nabla\Psi_{(q_1,q_2,q_3)} = \sum_i \frac{1}{h_i}\boldsymbol{q}_i\frac{\partial\Psi}{\partial q_i} \tag{6.6}$$

while a general surface integral transforms as

$$\begin{aligned}\int \boldsymbol{V}\, d\boldsymbol{s} = &\int V_1 h_2 h_3\, dq_2\, dq_3 + \int V_2 h_3 h_1\, dq_3\, dq_1 \\ &+ \int V_3 h_1 h_2\, dq_1\, dq_2\end{aligned} \tag{6.7}$$

Remembering that $h = h_\theta = h_\mu$ and that we are working in an elliptical section of the overall torus, our first integral will be written as

$$\begin{aligned}\int_{\psi_b} \tilde{\psi}^+_{in}\nabla\tilde{\psi}^+_{in}\cdot\, d\boldsymbol{s} = & \\ &= \int_{\psi_b}(\tilde{\psi}^+_{in}\nabla\tilde{\psi}^+_{in})_1 h\, d\theta + \int_{\psi_b}(\tilde{\psi}^+_{in}\nabla\tilde{\psi}^+_{in})_2 h\, d\mu \\ &= \int_{\psi_b}(\tilde{\psi}^+_{in}\frac{\partial\tilde{\psi}^+_{in}}{\partial\mu})\frac{1}{h}h\, d\theta + \int_{\psi_b}(\tilde{\psi}^+_{in}\frac{\partial\tilde{\psi}^+_{in}}{\partial\theta})\frac{1}{h}h\, d\mu\end{aligned} \tag{6.8}$$

Considering that the second integral is automatically zero for that type of integration, we are left with only

$$\int_{\psi_b}(\tilde{\psi}^+_{in}\frac{\partial\tilde{\psi}^+_{in}}{\partial\mu})\, d\theta \tag{6.9}$$

The expression for $\tilde{\psi}^+_{in}$ and its derivative are

$$\begin{aligned}\tilde{\psi}^+_{in} = \frac{-\xi_1}{\frac{\cosh(2\mu)}{\cosh(2\mu_b)} + e_0\cos(2\theta)}\Big\{&[1 + e_0\cosh(2(\mu-\mu_b))\cos(2\theta)]\frac{\sinh(\mu)}{\sinh(\mu_b)}\sin(\theta) \\ &- e_0\sinh(2(\mu-\mu_b))\frac{\cosh(\mu)}{\sinh(\mu_b)}\sin(2\theta)\cos(\theta)\Big\}\end{aligned} \tag{6.10}$$

$$\frac{\partial\tilde{\psi}^{+}_{in}}{\partial\mu} = -\xi_1 \frac{\frac{2\sinh(2\mu)}{\cosh(2\mu_b)}}{(\frac{\cosh(2\mu)}{\cosh(2\mu_b)} + e_0\cos(2\theta))^2}\Big\{[1+e_0\cosh(2(\mu-\mu_b))\cos(2\theta)]\frac{\sinh(\mu)}{\sinh(\mu_b)}\sin(\theta) - e_0\sinh(2(\mu-\mu_b))\frac{\cosh(\mu)}{\sinh(\mu_b)}\cos(\theta)\sin(2\theta)\Big\} - \frac{\xi_1}{\frac{\cosh(2\mu)}{\cosh(2\mu_b)} + e_0\cos(2\theta)}\Big\{2e_0\sinh(2(\mu-\mu_b))\frac{\sinh(\mu)}{\sinh(\mu_b)}\sin(\theta)\cos(2\theta) + [1+e_0\cosh(2(\mu-\mu_b)\cos(2\theta)]\frac{\cosh(\mu)}{\sinh(\mu_b)}\sin(\theta) - 2e_0\cosh(2(\mu-\mu_b))\frac{\cosh(\mu)}{\sinh(\mu_b)}\sin(2\theta)\cos(\theta) - e_0\sinh(2(\mu-\mu_b))\frac{\sinh(\mu)}{\sinh(\mu_b)}\sin(2\theta)\cos(\theta)\Big\} \quad (6.11)$$

On the elliptical boundary $\mu = \mu_b$ we obtain

$$\tilde{\psi}^{+}_{in} = -\xi_1\sin(\theta) \quad (6.12)$$

$$\frac{\partial\tilde{\psi}^{+}_{in}}{\partial\mu} = \frac{\cosh(\mu_b)}{\sinh(\mu_b)}\xi_1\sin(\theta) \quad (6.13)$$

By substituting expressions 6.12 inside equation 6.9, the first integral now becomes

$$-\frac{1}{2}\int_{\Psi_b}(\tilde{\psi}^{+}_{in}\frac{\partial\tilde{\psi}^{+}_{in}}{\partial\mu})\,d\theta = \frac{1}{2}\xi_1^2\frac{\cosh(\mu_b)}{\sinh(\mu_b)}\int_0^{2\pi}\sin(\theta)^2\,d\theta = \frac{\pi}{2}\xi_1^2\frac{\cosh(\mu_b)}{\sinh(\mu_b)} \quad (6.14)$$

Applying the same transformations, passing from Cartesian coordinates to flux ones, for the second integral in 6.5 we end up with

$$\frac{1}{2}\int_{\psi_c}\tilde{\psi}_\Delta\left[\frac{\tilde{\psi}_\Delta}{\partial u} - \frac{\tilde{\psi}_{V'}}{\partial u}\right]\cdot\,d\nu \quad (6.15)$$

Because at the generic flux surface $u = u_c$ continuity of the solution must hold, we have $\tilde{\psi}_\Delta = \tilde{\psi}_{V'}$, that is

$$a_m e^{-mu_c} + b_m e^{mu_c} = c_m e^{-mu_c} + d_m e^{mu_c} \quad (6.16)$$

The derivatives are (we neglect for the moment the factor ξ/b):

$$\left.\frac{\partial\tilde{\psi}_\Delta}{\partial u}\right|_{u_c} = \sum_{m,odd} m(-a_m e^{-mu_c} + b_m e^{mu_c})cos(m\nu) \quad (6.17)$$

$$\left.\frac{\partial\tilde{\psi}_{V'}}{\partial u}\right|_{u_c} = \sum_{m,odd} m(-c_m e^{-mu_c} + d_m e^{mu_c})cos(m\nu) \quad (6.18)$$

From equations 6.17 we obtain

$$\frac{\partial\tilde{\psi}_\Delta}{\partial u} - \frac{\partial\tilde{\psi}_{V'}}{\partial u}\bigg|_{u_c} = \sum_{m,odd} 2m\Big[(c_m - a_m)e^{-mu_c} + (b_m - d_m)e^{mu_c}\Big]cos(m\nu) \tag{6.19}$$

from 6.16 follows that

$$= \sum_{m,odd} 2m(b_m - d_m)e^{mu_c}cos(m\nu) \tag{6.20}$$

Putting everything back inside integral of 6.15

$$\begin{aligned}\frac{1}{2}\int_{\psi_c}\sum_{m,odd}^{\infty}(a_m e^{-mu_c} + b_m e^{mu_c})\Big[\sum_{m,odd}^{\infty} 2m(b_m - d_m)e^{mu_c}\Big]cos(m\nu)^2\,d\nu \\ = \sum_{m,odd}^{\infty}(a_m e^{-mu_c} + b_m e^{mu_c})\Big[m(b_m - d_m)e^{mu_c}\Big]\int_0^{2\pi} cos(m\nu)^2\,d\nu \\ = \pi\sum_{m,odd}^{\infty} m\lambda_{m(u_c)}(b_m - d_m)e^{mu_c}\end{aligned} \tag{6.21}$$

where the orthogonality of solutions $\tilde{\psi}$ allow us to retain only the term with the same index, while the ones with different indices are automatically zero. We have also make use of the expression $\lambda_{m(u_c)} = a_m e^{-mu_c} + b_m e^{mu_c}$ from [mettere referenza]. Combining equations 6.4,6.14 and 6.21 we obtain the final expression for the perturbed potential energy (reintroducing the $\xi/b = \xi_1$ factor):

$$\delta W = \xi_1^2\pi\sum_{m,odd}^{\infty} m\lambda_{m(u_c)}(b_m - d_m)e^{mu_c} \tag{6.22}$$

where the contributions coming from 6.4 and 6.14 cancel each other.
The next step is to determine coefficients c_m and d_m, to have everything that is needed to compute δW. We proceed firstly by recovering that

$$\tilde{\Psi}_\Delta(u_c,\nu) = \frac{\xi}{b}\sum_{m,odd}^{\infty}\lambda_{(u_c)}cos(m\nu) \tag{6.23}$$

$$\tilde{\Psi}_{V'}(u_c,\nu) = \frac{\xi}{b}\sum_{m,odd}^{\infty}(c_m e^{-mu} + d_m e^{mu})cos(m\nu) \tag{6.24}$$

$$\tilde{\Psi}_{V'}(\mu,\theta) = \frac{\xi}{b}\sum_{m,odd}^{\infty} g_m e^{-m(\mu-\mu_b)}sin(m\theta) \tag{6.25}$$

where the second equation express the solution of the perturbed flux inside the vacuum region before the separatrix (that we now identify with the index V'). The third equation the usual perturbed solution for plasma inside region Δ, but expressed in elliptical coordinates.
We have three unknowns, b_m, d_m and g_m, so we need three equations to solve them. We can use as first the continuity condition of $\tilde{\Psi}$ at the generic flux surface $u = u_c$, stated as

$$\tilde{\Psi}_\Delta = \tilde{\Psi}_{V'} \tag{6.26}$$

The other two equations can be found by extending the solutions all the way down

to the elliptical surface, $\mu = \mu_b$, that it is also a constant $u = u_b$ surface. Therefore, we can use the relations

$$\tilde{\Psi}_{V'}(u_b, \nu) = \tilde{\Psi}_{V'}(\mu_b, \theta) \tag{6.27}$$

$$\left.\frac{\partial \tilde{\Psi}_{V'}(u,\nu)}{\partial u}\right|_{u_b} = \left.\frac{\partial \tilde{\Psi}_{V'}(\mu,\theta)}{\partial u}\frac{\partial \mu}{\partial u}\right|_{\mu_b} \tag{6.28}$$

the second one has been derived using the well known chain rule, at $\mu = \mu_b$. With these two new equations we can close the system, to compute each coefficient for equations 6.23, 6.24 and 6.25.
Starting from 6.27, we can multiply both sides for $\cos(m\nu_b)$ and integrate over $d\nu_b$, where $\nu_b = \theta - \pi/2 + e_0/2\sin(2\theta)$. By omitting the summation sign, we get

$$\int_0^{2\pi} (c_n e^{-nu_b} + d_n e^{nu_b}) \cos(n\nu_b)\cos(m\nu_b)\, d\nu_b = \tag{6.29}$$
$$= \int_0^{2\pi} g_n \sin(n\theta)\cos(m\nu_b)\, d\nu_b$$

Because cosines are orthogonal the ones with different indices, $m \neq n$, are automatically zero, leaving contributions with the same index, $cos(m\nu_n)^2$, whose integral between zero and 2π give π. Proceeding by applying integral by parts on the r.h.s, we obtain

$$\int_0^{2\pi} g_n \sin(n\theta)\cos(m\nu_b)\, d\nu_b = \tag{6.30}$$
$$= g_n \left\{ \left[\frac{\sin(n\theta)\sin(m\nu_b)}{m} \right] \Bigg|_0^{2\pi} - \frac{n}{m}\int_{\pi/2}^{5\pi/2} \sin(m\nu_b)\cos(n\theta)\, d\theta \right\}$$
$$= -g_n \frac{n}{m}\int_{\pi/2}^{5\pi/2} \sin(m\nu_b)\cos(n\theta)\, d\theta$$
$$= -g_n \frac{n}{m}\int_{\pi/2}^{5\pi/2} \cos(n\theta)\sin[m(\theta - \frac{\pi}{2} + \frac{e_0}{2}\sin(2\theta))]\, d\theta$$
$$= -\frac{1}{2} g_n \frac{n}{m}\int_{\pi/2}^{5\pi/2} \sin[(m+n)\theta - m\frac{\pi}{2} + \frac{me_0}{2}\sin(2\theta)]$$
$$- \sin[(n-m)\theta + m\frac{\pi}{2} - \frac{me_0}{2}\sin(2\theta)]\, d\theta$$

using the change of variable, $\theta = \theta' + \pi/2$, we get

$$= -\frac{1}{2} g_n \frac{n}{m}\int_0^{2\pi} \sin[(m+n)\theta' - n\frac{\pi}{2} - \frac{me_0}{2}\sin(2\theta')] \tag{6.31}$$
$$- \sin[(n-m)\theta' + n\frac{\pi}{2} + \frac{me_0}{2}\sin(2\theta')]\, d\theta'$$

depending on the m index, the transformations for sine can be

$$\sin(\alpha + \frac{3}{2}\pi) = -\cos(\alpha) \tag{6.32}$$

$$\sin(\alpha + \frac{1}{2}\pi) = \cos(\alpha) \tag{6.33}$$

but the different sign can be incorporated inside coefficient g_n, so the final expression is

$$\frac{1}{2}g_n\frac{n}{m}\int_0^{2\pi}\cos[(m+n)\theta' - \frac{me_0}{2}\sin(2\theta')] - \cos[(n-m)\theta' + \frac{me_0}{2}\sin(2\theta')]\,d\theta' \tag{6.34}$$

These obtained are the Bessel functions of the first kind, and we can rewrite the final result as

$$c_m e^{-mu_b} + d_m e^{mu_b} = \frac{n}{m}g_n A_m^n \tag{6.35}$$

where

$$A_m^n = \sum_{j=\pm 1} jJ_{\frac{m+jn}{2}(\frac{me_0}{2})} \tag{6.36}$$

Applying the same transformation to 6.28, brings

$$\int_0^{2\pi} n(-c_n e^{-nu_b} + d_n e^{nu_b})\cos(n\nu_b)\cos(m\nu_b)\,d\nu_b = \\ = \int_0^{2\pi} -ng_n(1 + e_0 cos(2\theta))\sin(n\theta)\cos(m\nu_b)\,d\nu_b$$

$$m(-c_m e^{-mu_b} + d_m e^{mu_b})\pi = \\ = -ng_n\int_{\pi/2}^{5\pi/2}\sin(n\theta)\cos[m(\theta - \frac{\pi}{2} + \frac{e_0}{2}\sin(2\theta))]\,d\theta \\ = -\frac{1}{2}\frac{n}{m}g_n\int_{\pi/2}^{5\pi/2}\Big\{\sin[(m+n)\theta - m\frac{\pi}{2} + \frac{me_0}{2}\sin(2\theta)] \\ + \sin[(n-m)\theta + m\frac{\pi}{2} - \frac{me_0}{2}\sin(2\theta)]\Big\}\,d\theta$$

applying the same coordinate transformation, $\theta = \theta' + \pi/2$, we get

$$= -\frac{1}{2}\frac{n}{m}g_n\int_{\pi/2}^{5\pi/2}\Big\{\sin[(m+n)\theta' + n\frac{\pi}{2} - \frac{me_0}{2}\sin(2\theta')] \\ + \sin[(n-m)\theta' + n\frac{\pi}{2} + \frac{me_0}{2}\sin(2\theta')]\Big\}\,d\theta'$$

Incorporating the sing inside coefficient g_n and using Bessel function definition, we arrive at

$$-c_m e^{-mu_b} + d_m e^{mu_b} = \frac{n}{m}g_n B_m^n \tag{6.37}$$

where

$$B_m^n = \sum_{j=\pm 1} J_{\frac{m+jn}{2}(\frac{me_0}{2})} \tag{6.38}$$

Taking expressions 6.35 and 6.37, combine them to obtain

$$c_m = g_n \frac{e^{mu_b}}{2} \frac{n}{m} (A_m^n - b_m^n) \tag{6.39}$$

$$d_m = g_n \frac{e^{-mu_b}}{2} \frac{n}{m} (A_m^n + b_m^n) \tag{6.40}$$

Inserting coefficients' expressions 6.39 and 6.40, inside the continuity condition 6.26, we obtain

$$2\lambda_{m(u_c)} = e^{-m(u_c-u_b)} \sum_{n,odd}^{\infty} g_n \frac{n}{m} (A_m^n - b_m^n) \tag{6.41}$$

$$+e^{m(u_c-u_b)} \sum_{n,odd}^{\infty} g_n \frac{n}{m} (A_m^n + b_m^n) \tag{6.42}$$

This is a linear system, with unknown vector coefficients g_n, know vector $b_m = 2\lambda_{m(u_c)}$ and matrix Λ_m^n with entries $e^{-m(u_c-u_b)} \frac{n}{m}(A_m^n - b_m^n) + e^{m(u_c-u_b)} \frac{n}{m}(A_m^n + b_m^n)$. The linear system is rewritten as

$$\Lambda_m^n g_n = b_m \tag{6.43}$$

Where m is the number of rows and n is the number of columns of the matrix. Since n is actually the same index spanning the infinite series of the perturbed solutions, but in a different reference frame due to the transformation adopted above, then also the n index will be truncated at the same value of m, i.e. m_{max}. The matrix Λ_m^n will then result to be squared.

6.2 Asymptotic expansion of matrix entries

Before solving the linear system 6.43, it is better to firstly analyze matrix Λ_m^n in order to understand some computational problems that will arise later. We can compute the asymptotic behavior of its entries, along rows m and columns n. We firstly define some quantities, that will be useful for our purposes.

$$e_0 = \frac{b^2 - a^2}{b^2 + a^2} = sech(\alpha_b) \tag{6.44}$$

$$sech(\alpha_b) = sech(\alpha_b) + \tanh(\alpha_b) sech(\alpha_b)\delta + \wr(\delta^2) \tag{6.45}$$

$$= e_0(1 + \tanh(\alpha_b)\delta) + \wr(\delta^2) \tag{6.46}$$

$$(1 - e_0^2)^{1/2} = \tanh(\alpha_b) \tag{6.47}$$

where $\alpha_b = 2\mu_b$.
The first part of matrix Λ_m^n is

$$e^{-m(u_c-u_b)} \frac{n}{m} (A_m^n - b_m^n) = \tag{6.48}$$

$$= e^{-m(u_c-u_b)} \frac{n}{m} (J_{\frac{m+n}{2}} - J_{\frac{m-n}{2}} - J_{\frac{m+n}{2}} - J_{\frac{m-n}{2}})$$

$$= e^{-m(u_c-u_b)} \frac{n}{m} (-2J_{\frac{m-n}{2}}) \tag{6.49}$$

(we are omitting the argument $\frac{me_0}{2}$ for sake of simplicity). We proceed in a similar way as has been done in Appendix D of [12]. Let $\nu = (m-n)/2$ and $\nu' = (m+n)/2$, and introduce α_1 and α_2 as:

$$sech(\alpha_1) = e_0\left(1 + \frac{n}{2\nu}\right) \tag{6.50}$$

$$sech(\alpha_2) = e_0\left(1 - \frac{n}{2\nu'}\right) \tag{6.51}$$

In the limit $m \to \infty$, let us denote the deviations of α_1 and α_2 from α_b by δ_1 and δ_2 respectively, so that $\alpha_1 = \alpha_b - \delta_1$ and $\alpha_2 = \alpha_b + \delta_2$. Thus,

$$sech(\alpha_1) = \frac{1}{\cosh(\alpha_b - \delta_1)} \approx e_0(1 + \tanh(\alpha_b)\delta_1) \tag{6.52}$$

$$sech(\alpha_2) = \frac{1}{\cosh(\alpha_b + \delta_2)} \approx e_0(1 - \tanh(\alpha_b)\delta_2) \tag{6.53}$$

Comparing 6.50 - 6.53 leads to

$$\delta_1 = \frac{n}{2\nu}\coth(\alpha_b), \quad \delta_2 = \frac{n}{2\nu'}\coth(\alpha_b) \tag{6.54}$$

From [citare libro], formula (9.3.2), we now that the asymptotic expansion of the Bessel function, for $\nu \to \infty$, can be expressed as

$$J_\nu(\nu sech(\alpha)) \sim \frac{e^{\nu(\tanh(\alpha)-\alpha)}}{\sqrt{2\pi\nu\tanh(\alpha)}} \tag{6.55}$$

Analyzing the argument of the exponential

$$(\frac{m-n}{2})(\tanh\alpha_b - \alpha_b + \delta_1 - e_0^2\delta_1) + m\frac{\tanh\alpha_b}{2} - m\frac{\alpha_b}{2} - mu_c = \tag{6.56}$$

$$= m\tanh\alpha_b - m\alpha_b - n\frac{\tanh\alpha_b - \alpha_b}{2} + (\frac{m+n}{2})(\delta_1 - e_0^2\delta_1) - mu_c =$$

$$= m(\tanh\alpha_b - \alpha_b) - n\frac{\tanh\alpha_b - \alpha_b}{2} + n\frac{\coth\alpha_b - e_0^2\coth\alpha_b}{2} - mu_c =$$

$$= m(\tanh\alpha_b - \alpha_b - mu_c + n\mu_b \tag{6.57}$$

Substituting 6.57 and 6.55 inside 6.49, we get that this first part goes as

$$\sim -\frac{\sqrt{2}n}{m^{3/2}}\frac{e^{-mu_c}}{\pi\tanh\alpha_b}e^{m(\tanh\alpha_b-\alpha_b)}e^{n\mu_b} \tag{6.58}$$

The second part of matrix Λ_m^n is expressed as

$$e^{m(u_c-u_b)}\frac{n}{m}(A_m^n + B_m^n) = e^{m(u_c-u_b)}\frac{n}{m}(2J_{\frac{m+n}{2}}) \tag{6.59}$$

The exponential part from 6.55 in this case is

$$(\frac{m+n}{2})(\tanh\alpha_b + -e_0^2\delta_2 - \delta_2 - \alpha_b) - m\frac{\tanh\alpha_b - \alpha_b}{2} - m\frac{\alpha_b}{2} + mu_c = \tag{6.60}$$

$$= n\frac{\tanh\alpha_b - \alpha_b}{2} + n\frac{(e_0^2\coth\alpha_b - \coth\alpha_b}{2} + mu_c =$$

$$= -n\frac{\alpha_b}{2} + mu_c = -n\mu_b + mu_c \tag{6.61}$$

The final expression for this part becomes

$$\sim \frac{\sqrt{2}n}{m^{3/2}}\frac{e^{-n\mu_b}}{\sqrt{\pi\tanh\alpha_b}}e^{-mu_c} \tag{6.62}$$

Putting back together expressions 6.58 and 6.62, we can write

$$\Lambda_m^n \sim -\frac{\sqrt{2}n}{m^{3/2}\sqrt{\pi\tanh\alpha_b}}\left(e^{m(2u_b)}e^{-mu_c}e^{n\mu_b} - e^{-n\mu_b}e^{mu_c}\right) \tag{6.63}$$

where the term $(\tanh\alpha_b - \alpha_b) = 2u_b$. Considering the limit as $u_c \to 0^-$ the final expression becomes

$$\Lambda_m^n \sim \frac{\sqrt{2}ne^{-n\mu_b}}{m^{3/2}\sqrt{\pi\tanh\alpha_b}}e^{mu_c} \qquad m \to \infty \tag{6.64}$$

To compute the asymptotic expansion for the columns, $n \to \infty$, is relatively more simple. We make use of the formula (9.3.1), from [Libro], which is

$$J_\nu(z) \sim \frac{1}{\sqrt{2\pi\nu}}\left(\frac{ez}{2\nu}\right)^\nu \qquad \nu \to \infty \tag{6.65}$$

where e is the exponential. Considering that $\nu = (n-m)/2$, the first part of the matrix can be expanded as:

$$e^{-m(u_c-u_b)}\frac{n}{m}(A_m^n - b_m^n) = e^{-m(u_c-u_b)}\frac{n}{m}(-2J_{\frac{m-n}{2}}) \tag{6.66}$$

$$\sim e^{-m(u_c-u_b)}\frac{n}{m}\left[-2(-1)^{\frac{n-m}{2}}\frac{1}{\sqrt{2\pi\frac{(n-m)}{2}}}\left(\frac{e(me_0)/2}{2(n-m)/2}\right)^{\frac{n-m}{2}}\right] \tag{6.67}$$

Using Stirling formula

$$x! \sim \sqrt{2\pi x}\frac{x^x}{e^x} \tag{6.68}$$

the previous expression can be rewritten as

$$\sim e^{-m(u_c-u_b)}\frac{n}{m}\left[-2(-1)^{\frac{n-m}{2}}\left(\frac{me_0}{4}\right)^{\frac{n-m}{2}} \Big/ \left(\frac{n-m}{2}\right)!\right] \tag{6.69}$$

The second part of the matrix, for $n \to \infty$, in the same way is rewritten as

$$e^{-m(u_c-u_b)}\frac{n}{m}(-2J_{\frac{m-n}{2}}) \sim e^{m(u_c-u_b)}\frac{n}{m}\left[2\left(\frac{me_0}{4}\right)^{\frac{m+n}{2}} \Big/ \left(\frac{m+n}{2}\right)!\right] \tag{6.70}$$

Putting back together 6.69 and 6.70, we end up with

$$\Lambda_m^n \sim \frac{n}{m}\left\{e^{-m(u_c-u_b)}\left[-2(-1)^{\frac{n-m}{2}}\left(\frac{me_0}{4}\right)^{\frac{n-m}{2}}\Big/\left(\frac{n-m}{2}\right)!\right]\right. \tag{6.71}$$

$$\left.+e^{m(u_c-u_b)}\left[2\left(\frac{me_0}{4}\right)^{\frac{m+n}{2}}\Big/\left(\frac{m+n}{2}\right)!\right]\right\} \qquad n\to\infty \tag{6.72}$$

Summarizing this last part, we have that matrix entries, along rows, go as

$$\Lambda_m^n \sim \frac{\sqrt{2}ne^{-n\mu_b}}{m^{3/2}\sqrt{\pi\tanh\alpha_b}}e^{mu_c} \qquad m\to\infty \tag{6.73}$$

while along columns, go as

$$\Lambda_m^n \sim \frac{n}{m}\left\{e^{-m(u_c-u_b)}\left[-2(-1)^{\frac{n-m}{2}}\left(\frac{me_0}{4}\right)^{\frac{n-m}{2}}\Big/\left(\frac{n-m}{2}\right)!\right]\right. \tag{6.74}$$

$$\left.+e^{m(u_c-u_b)}\left[2\left(\frac{me_0}{4}\right)^{\frac{m+n}{2}}\Big/\left(\frac{m+n}{2}\right)!\right]\right\} \qquad n\to\infty \tag{6.75}$$

This behavior can be confirmed by plotting together Λ_m^n entries, and the formulas obtained now. Here below are shown for the first row and column, respectively.

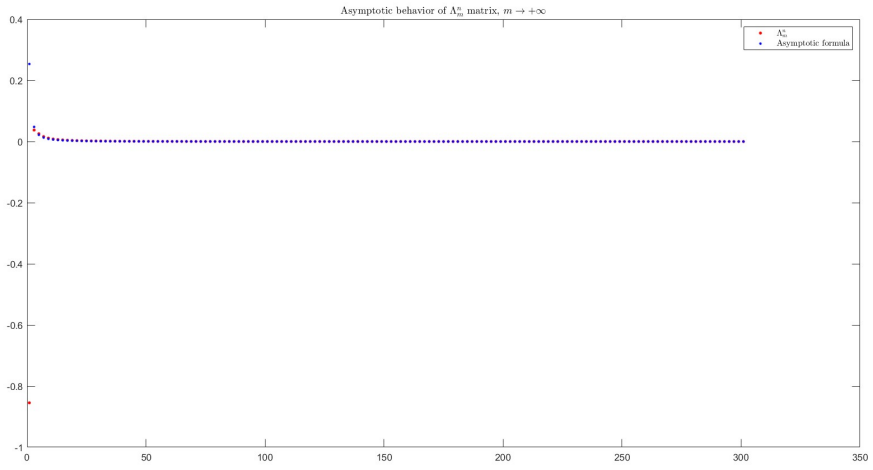

FIGURE 6.2: Asymptotic behavior of Λ_m^n first column for $m\to\infty$

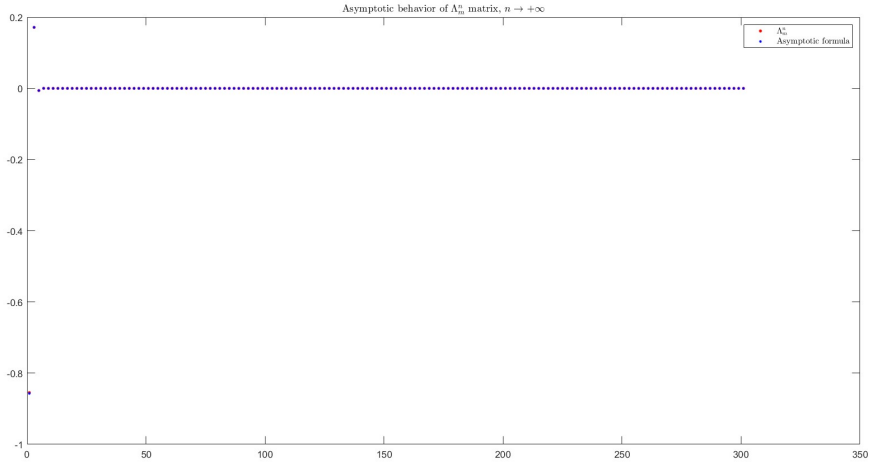

FIGURE 6.3: Asymptotic behavior of Λ^n_m first row for $n \to \infty$

As we can clearly see, matrix entries becomes instantly very small, very close to zero. The fact that the majority of the entries are so small produces a matrix with a lot of columns that are "almost" linear dependent one to each other, where we have made use of the term "almost" in a rough way that will now be clarified. The definition of linear dependence when dealing with finite precision arithmetic is slightly different w.r.t the usual concept in infinite arithmetic precision. Thus, two columns that have entries very close one to each other, cannot be linear dependent in infinite arithmetic, because they are different, but can instead be considered as linear dependent when working with finite arithmetic precision, because below a certain tolerance they cannot be distinguished anymore, thus producing computational inaccuracies. This linear dependence is a problem when dealing with matrix inversion, as it has a lower rank w.r.t. its dimensions, leaving us to deal with the problem of not unique and/or low accurate solutions.
To have a measure of how "bad" our matrix is performing the **condition number**, of matrix Λ^n_m, is one of the most useful quantities. This latter can be analytically defined as

$$\mathbf{K}_{(\mathbf{\Lambda})} = ||\Lambda||||\Lambda^{-1}|| \tag{6.76}$$

It gives an indication of the accuracy of the results from matrix inversion and the linear equation solution. Large condition numbers indicate that a small change in the coefficients of matrix $\mathbf{\Lambda}$ can lead to larger changes in the output $\mathbf{b}$. It spans value from one, the best case, up to infinity, that is the extreme case when the matrix is so poorly conditioned that it is singular and so has no inverse, and the linear equation has no unique solution.
In the table below are reported condition numbers of matrix Λ^n_m for different values of e_0 and $u = u_c$, and for different truncation numbers of $m = m_{max}$.

u_c	$e_0 = 0.05$	$e_0 = 0.1$	$e_0 = 0.2$
-1	1	1	1
-0.1	2.1991e+05	7.2293e+03	275.3813
-0.01	1.4444e+58	4.6533e+43	1.5171e+30

TABLE 6.1: Condition number for $m_{max} = 1/|u_c|$

u_c	$e_0 = 0.05$	$e_0 = 0.1$	$e_0 = 0.2$
-1	1.9484	1.0586	1.9959
-0.1	1.5252e+16	5.9953e+11	4.2505e+07
-0.01	3.3426e+167	1.2071e+124	7.3078e+81

TABLE 6.2: Condition number for $m_{max} = 3/|u_c|$

u_c	$e_0 = 0.05$	$e_0 = 0.1$	$e_0 = 0.2$
-1	7.7690	1.0909	7.3527
-0.1	3.0567e+32	5.6221e+23	3.9755e+15
-0.01	NaN	2.0443e+236	4.9408e+150

TABLE 6.3: Condition number for $m_{max} = 6/|u_c|$

As we can see, increasing m_{max} leads to a worst condition number because the matrix is getting larger and larger and more linear dependent columns are added. But on the contrary, a low number of terms will not be able to accurately represent the series. The truncation number turned to be a problem of compromise, where we want to choose a large m in order to correctly represent our series, but not too large to avoid loss of accuracy from matrix inversion.

6.3 Residual and error analysis

After this first analysis of matrix's entries, we can now proceed to solve the linear system 6.43. Due to the linear dependence problem illustrated above we have to deal with a rank deficient matrix and so with a system admitting not unique solution. One way to deal with our problem is to solve the linear system using the pseudoinverse matrix, or Moore-Penrose inverse (see D). Using this approach we are basically searching among all the solutions the one that minimizes the square of the norm, i.e. $||\mathbf{b} - \mathbf{\Lambda g}||^2$. The solution of our linear system can thus be written analytically as

$$g_n = (\Lambda_m^n)^\dagger b_m = \Lambda_n^{m\dagger} b_m \tag{6.77}$$

Speaking now about how this is performed practically, Matlab provides a simple command (pinv), and compute the pseudoinverse through the singular value decomposition of our matrix. It is also possible to increase the minimum tolerance under which singular values of Λ_m^n, that are smaller than that tolerance, are considered zero. Increasing the tolerance will produce more accurate results, in particular for very small values of $u = u_c$, but at the same time the computed solution deviate from the original one, so we are not going to consider it.
After the inversion of the matrix we can now compute the relative residual, expressed as

$$r_{rel} = \frac{||\mathbf{r}||}{||\mathbf{b}||} = \frac{||\mathbf{b} - \mathbf{\Lambda g}||}{||\mathbf{b}||}, \tag{6.78}$$

where $\mathbf{r}$ is the residual. Different plots of r_{rel} as function of u_c are shown here below, for different e_0 values.

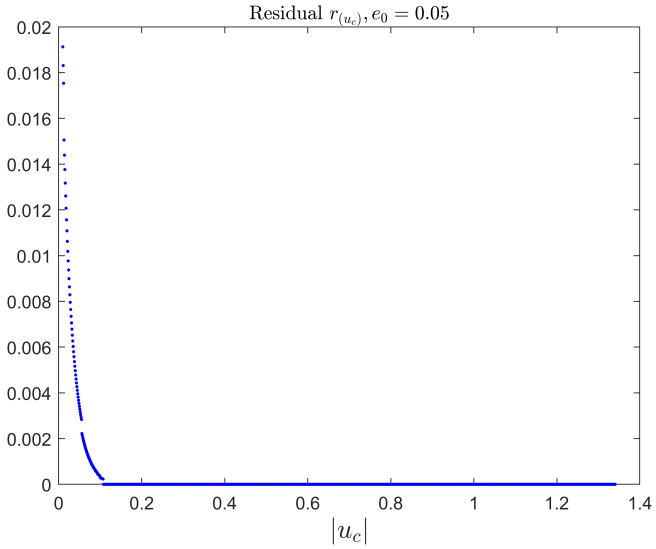

FIGURE 6.4: Residual for $e_0 = 0.05$

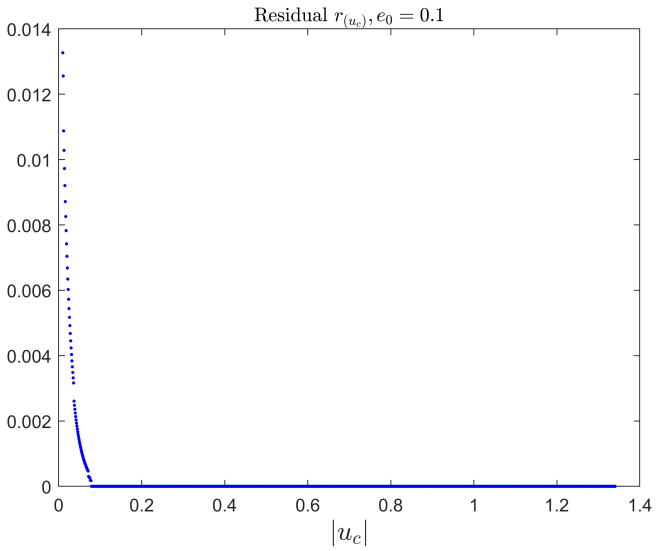

FIGURE 6.5: Residual for $e_0 = 0.1$

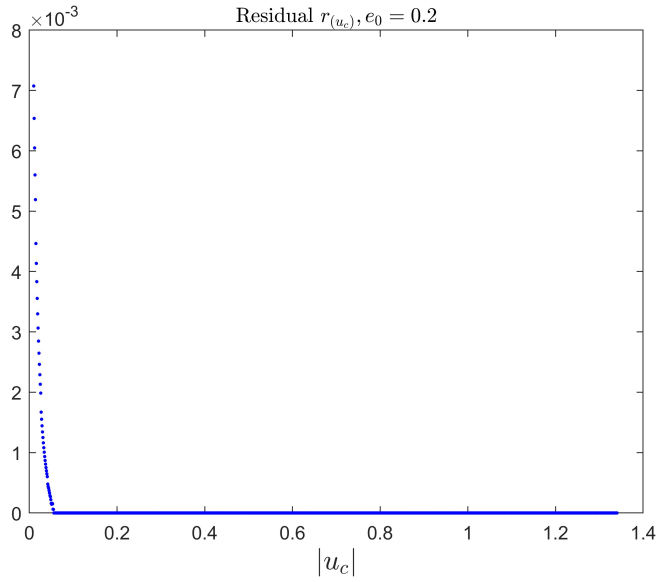

FIGURE 6.6: Residual for $e_0 = 0.2$

Here below is reported the table with the values of the residuals for different e_0, w.r.t a truncation value of $m_{max} = 3/|u_c|$.

$\|u_c\|$	$e_0 = 0.05$	$e_0 = 0.1$	$e_0 = 0.2$
0.5	1.5805e-16	6.5396e-16	5.8990e-16
0.1	3.6511e-04	8.1615e-16	6.8976e-16
0.08	8.6595e-04	8.5971e-16	7.5397e-16
0.06	1.9e-03	8.4055e-04	1.0050e-13
0.05	3.4e-03	1.4e-03	2.0680e-04
0.03	7.3e-03	4.2e-03	1.3e-03
0.009	0.02	0.014	7.7e-03

TABLE 6.4: Relative Residual

Increasing the ellipticity increases the number of points that we can use inside our analysis, thus we can compute values of δW for smaller $|u_c|$ using a larger e_0, but we have to be careful, we have previously said that by increasing ellipticity we have also to increase the m_{max} in order to avoid severe truncation errors. Using $m_{max} = 3/|u_c|$ is reasonable only for e_0 up to 0.1, we will see later that for larger values of e_0 keeping the same number of the maximum harmonics will produce errors.
It is also very important to analyze the maximum error that our system is producing. Considering $\mathbf{g}$ our computed solution, $\mathbf{g}_{ex}$ the exact solution of our system and $\mathbf{e} = \mathbf{g}_{ex} - \mathbf{g}$ the error of our solution w.r.t the exact one, we can write

$$\begin{aligned} ||\mathbf{e}|| &= ||\mathbf{g}_{ex} - \mathbf{g}|| \\ &= ||\mathbf{\Lambda}^{-1}\mathbf{b} - \mathbf{g}|| \\ &= ||\mathbf{\Lambda}^{-1}\mathbf{b} - \mathbf{\Lambda}^{-1}\mathbf{\Lambda}\mathbf{g}|| \\ &= ||\mathbf{\Lambda}^{-1}(\mathbf{b} - \mathbf{\Lambda}\mathbf{g})|| = ||\mathbf{\Lambda}^{-1}\mathbf{r}|| \leq ||\mathbf{\Lambda}^{-1}||||\mathbf{r}|| \end{aligned}$$

The general inequality induced by the norm for a linear system is written as $||\mathbf{b}|| \leq ||\mathbf{\Lambda}||||\mathbf{g}||$. Thus, dividing $||\mathbf{e}||$ by $||\mathbf{g}||$ we end up with

$$\frac{||\mathbf{e}||}{||\mathbf{g}||} \leq \frac{||\mathbf{\Lambda}||}{||\mathbf{b}||}||\mathbf{\Lambda}^{-1}||||\mathbf{r}|| = \mathbf{K}_{(\Lambda)}\frac{||\mathbf{r}||}{||\mathbf{b}||} \tag{6.79}$$

where $\mathbf{K}_{(\Lambda)} = ||\mathbf{\Lambda}||||\mathbf{\Lambda}^{-1}||$ is the condition number of matrix $\mathbf{\Lambda}$. From 6.79 we can see how a small residual does not always imply a small error on our solution. Considering $m_{max} = 3/|u_c|$, the table below shows the maximum relative error $e_{rel-max} = \mathbf{K}_{(\Lambda)}||\mathbf{r}||/||\mathbf{b}||$, for different e_0 and u_c.

$\lvert u_c\rvert$	$e_0 = 0.05$	$e_0 = 0.1$	$e_0 = 0.2$
0.5	2.3581e-14	1.2519e-14	1.5833e-15
0.4	4.9532e-14	8.7653e-15	1.1806e-16
0.3	7.0426e-12	2.5388e-13	8.2460e-15
0.2	5.6998e-09	1.8958e-11	9.3126e-14
0.1	5.5688e+12	4.8931e-04	2.9319e-08
0.09	1.4361e+14	4.2e-03	2.4447e-07
0.08	4.8703e+16	0.2570	2.4905e-06
0.07	2.2557e+20	6.1841e+13	1.7336e-04
0.06	1.5461e+25	3.4571e+17	6.0938

TABLE 6.5: Maximum Relative Error, $m_{max} = 3/|u_c|$

We can see now that some points that have a small relative residual carry instead a large relative error; e.g. for $e_0 = 0.1$ at $|u_c| = 0.08$ we have $r_{rel} \sim 10^{-16}$ but $e_{rel} \leq 0.2527$.
The same results are shown for the other two values of m_{max}:

$\lvert u_c\rvert$	$e_0 = 0.05$	$e_0 = 0.1$	$e_0 = 0.2$
0.5	8.0498e-16	1.6772e-15	2.0453e-16
0.4	3.5386e-17	2.4659e-17	6.5251e-17
0.3	1.6228e-15	1.1317e-15	1.2470e-17
0.2	4.6389e-14	1.0184e-15	2.2238e-15
0.1	9.4754e-10	3.7703e-12	8.9538e-14
0.09	9.3496e-10	4.0779e-12	2.5563e-13
0.08	1.1585e-08	4.7160e-11	7.7012e-13
0.07	1.4457e-07	2.8588e-10	2.8165e-12
0.06	1.0777e-05	2.3693e-09	2.6797e-11

TABLE 6.6: Maximum Relative Error, $m_{max} = 1/|u_c|$

$\lvert u_c\rvert$	$e_0 = 0.05$	$e_0 = 0.1$	$e_0 = 0.2$
0.5	7.6277e-12	5.2292e-13	3.7669e-15
0.4	2.0363e-10	5.6301e-12	2.5506e-14
0.3	2.4532e-07	6.2311e-10	3.6966e-12
0.2	5.4376e+09	4.0751e-05	2.2509e-09
0.1	1.3471e+29	6.0916e+19	1.8703e+10
0.09	6.8373e+32	4.6940e+22	3.4868e+12

TABLE 6.7: Maximum Relative Error, $m_{max} = 6/|u_c|$

As expected, increasing m_{max} will also increase the maximum relative error, and vice versa. We now have an idea of the minimum point $|u_c|$ up to which the perturbed energy can be computed. Below this value the error carried by the coefficients results to be too large to be taken in consideration.

Chapter 7

Locating the marginal stability flux surface

This last chapter will be devoted to show the results obtained from the numerical computation of the δW expression. We recall here that what we want to obtain is a curve for δW as a function of u_c, for a fixed value of e_0 and so of u_b, the convenient elliptical surface. The work done up to now is crucial as the problem of stability has been reduced to determine the sign of the perturbed potential energy. Thus, we can now build our curve starting from the elliptical surface $u = u_b$ and up to the last closed magnetic flux surface, $u = u_X$. In chapter 4 has been shown that in these two case studies plasma behavior changes significantly due to the nature of the current sheets forming along the separatrix, acting as a passive stabilization system. Practically, we expect that the δW curve, which starts from $u = u_b$ and is extended up to $u \to 0$, will cross the axis in the point where marginal stability occurs, that we have called $u = u_{marginal}$, i.e. where $\delta W = 0$ and so $\gamma^2 = 0$, remembering that γ is the growth rate.
We will show in a moment that this conclusion cannot be achieved only considering the results of our problem. As has been shown in the previous chapter, the closer we get to the separatrix, the more harmonics will be needed in order to correctly represent the perturbed solution $\tilde{\psi}$ and $\tilde{\phi}$, and so larger the matrix Λ^n_mwill become, thus producing bad conditioned results with large errors on the coefficients needed to represent the δW harmonic contributions. So, calculations for $\delta W(u = u_c)$ can be done up to a minimum value of u_c, which is given by tables 6.6, 6.5 and 6.7, after that point the obtained results are matched to large errors and cannot be taken as correct points to construct the final curve. Unfortunately, will be shown later that the minimum u_c up to which calculations can be made is not smaller enough in order to locate the marginal stability point, $u = u_{marginal}$, thus the last part of the chapter will be devoted to illustrate some curves obtained through extrapolation, using non linear models.

7.1 δW curve

The plots shown below in figures 7.2 and 7.3, are related to the cases with $e_0 = 0.1$ and $e_0 = 0.2$ where the value for m_{max} has been taken as $m_{max} = 6/u_c$. This value of m has been used also for $e_0 = 0.2$, as only a small error is introduced for $|u_c| > 1$. Thus, for the minimum value of u_c we refer to table 6.7. While for $e_0 = 0.05$, shown in figure 7.1, the truncation value has been taken as $m_{max} = 3/|u_c|$, so we will refer to table 6.5 to take the minimum u_c. In every result for the different e_0s, the final curve doesn't arrive to cross the axis. Because of the fact that δW value at the separatrix, i.e. at $u = 0$, must be positive (we recall here that the perturbed plasma

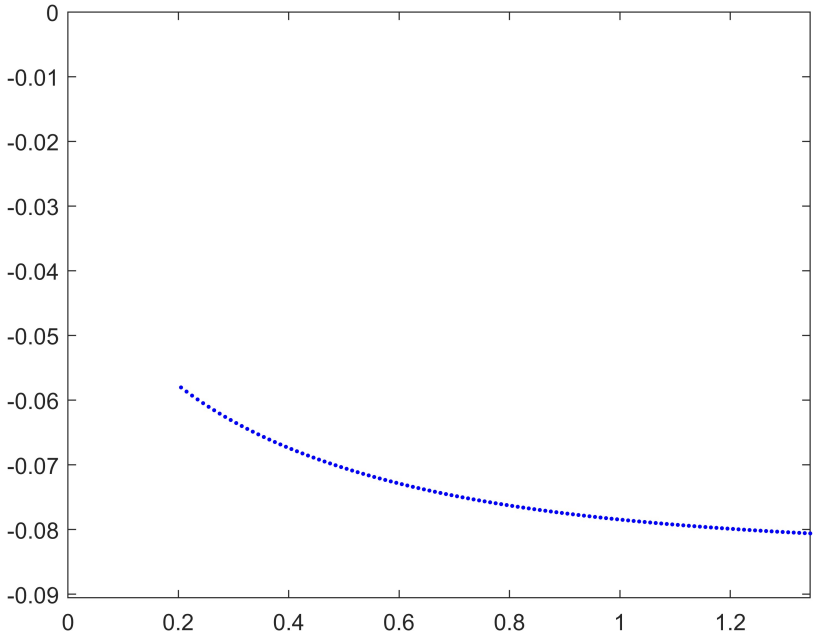

FIGURE 7.1: δW curve for $e_0 = 0.05$

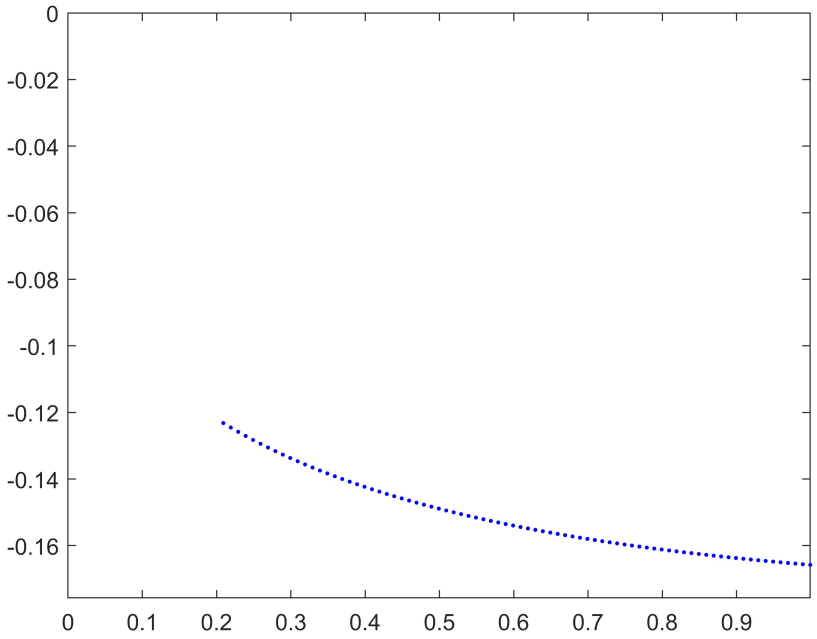

FIGURE 7.2: δW curve for $e_0 = 0.1$

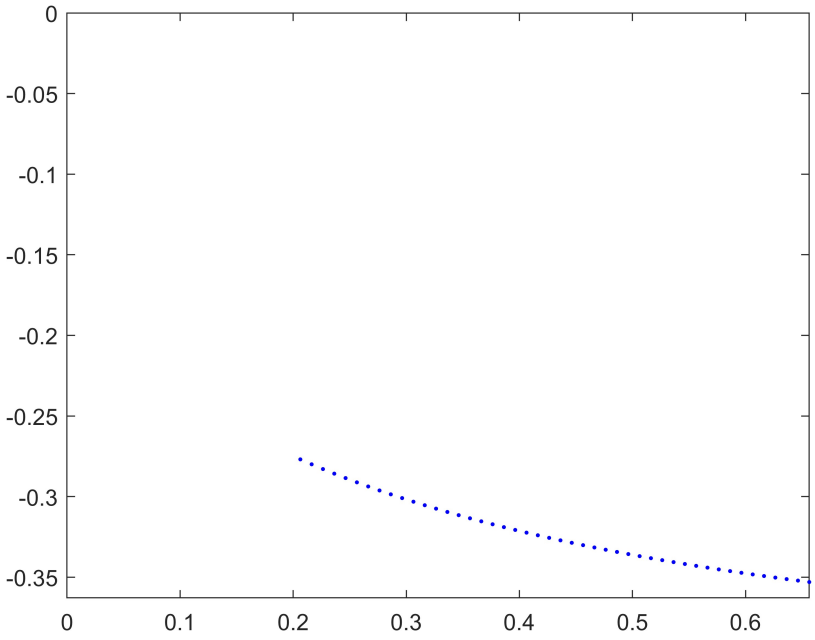

FIGURE 7.3: δW curve for $e_0 = 0.2$

should have a stable behavior at $u_c = u_X = 0$), we should expect a rapid increase in the slope of the curve in the final part. Furthermore, the fact that the curve could not be computed for such small values of u_c, is indicative of the fact that for these small coordinates the δW expression, together with the series representing the perturbed solutions, is very sensitive to computational errors, as the smaller contributions that sum up in the series increase.

7.2 Fit and extrapolation

The final step is to extrapolate the last part of the curve in order to have an idea of the position of the marginal stability surface, u_{marg}. Due to the fact that we are dealing with a physical quantity, i.e. the perturbed energy, the behavior of the system as a function of u_c must be justified. Since there are no reasons that lead us to think that the last unknown part of the curve has a drop or some wiggling behavior, it is reasonable to seek out a model that allows the curve to increase for $u \to 0$. The searched model must be obtained from the fit of the curve, on the previously evaluated points.
For all the cases that will follow, the chosen model is written through the following non linear expression:

$$\delta W_{(u_c)} = \sum_i a_i |u_c|^i + \ln\left(|u_c| + h\right) \tag{7.1}$$

where $i = \{0, \frac{1}{2}, 1, 2, 3, 4\}$, and a_i, h are the coefficients computed by fitting the curve, with $h > 0$. The polynomial up to grade 4 is justified by the fact that lower degrees would not fit the curve perfectly as this model does; values of the fit evaluation parameters will be given in the next subsections, as those in tables 7.2 and 7.6. Also, higher values of the polynomial make the computation of the coefficients imprecise, thus leading to large error bounds. The logarithmic term and the grade $1/2$ of the

polynomial are there in order to correctly represent the rapid increase in the slope of the curve in the final part.
Furthermore, in chapter 4 the case where plasma is extended up to the magnetic separatrix has been illustrated, with the final result of a stable behavior under small perturbations. From the expression of γ^2 is possible to compute the value of δW at $u_c = u_X = 0$, as shown in Appendix E. Here below the cases for $e_0 = 0.05$ and $e_0 = 0.1$ are derived, both under two different circumstances. In the first scenario the computed value of $\delta W_{(u_c=0)}$ at the separatrix is not used as a point inside the fitting dataset, while in the second one this value is instead considered. A comparison between the two scenarios is presented for both the e_0s cases, in order to understand if the model described by 7.1 is suitable to represent the behavior even in the case where $\delta W_{(u_c=0)}$ is unknown.
An additional case with $e_0 = 0.2$ is then presented, but we will see that the obtained results carry too large error bounds to make any conclusion about it.

7.2.1 Case $e_0 = 0.05$

No additional point at the separatrix

The first case is the one related to a value of the ellipticity parameter as $e_0 = 0.05$. Referring to figure 7.4, the red curved overlap almost perfectly the data points, in fact it is quite difficult to see the red curve passing for all the different blue points and also the error bounds that are almost null. Matlab toolbox for the CurveFit allows also to compute the prediction bounds, obtained from the calculations of coefficients a_i and h. Figure 7.5 show the residuals of the blue points from the red curve, that is taken as the zero reference, while table 7.2 shows some important parameters that are useful in order to understand the goodness of the fit, even if a good indication comes from the graph analysis.
We report here a brief description of these latter parameters, which can be found in the Matlab website: Evaluating Goodness of the Fit.

- SSE (Sum of Squares Due to the Error): it measures the total deviation of the response values from the fit to the response values. Values near zero indicates a small random error component.
- RSquare: it measures how well the fit is in explaining the variation of the data points. It can take value between 0 and 1, a greater value means that the model is taking into account a great portion of the variance.
- Adjrsquare (Degrees of Freedom Adjusted RSquare): it uses the R-square and adjusts it based on the residual degrees of freedom. The residual degrees of freedom is defined as the number of response values minus the number of fitted coefficients estimated from the response values. A good fit must have a value related to this statistic as closer to one as possible.
- RMSE (Root Mean Square Error): it estimates the standard deviation of the random component in the data. A small value is indicative of a good fit.

From the explanation of the different statistic parameters made previously, table 7.2 shows very good result of the produced fit. Also, analyzing the extrapolated curve, figure 7.6, is possible to locate the value of the marginal stability at around $|u_{marg}| \approx 0.039$, while the value of the relative perturbed energy at the separatrix is $\delta W_{(u_c=0)}/\xi_1^2 = 0.5482$. Calculations from Appendix E show that the value at the separatrix is instead $\delta W_{(u_c=0)}/\xi_1^2 = 0.280$.

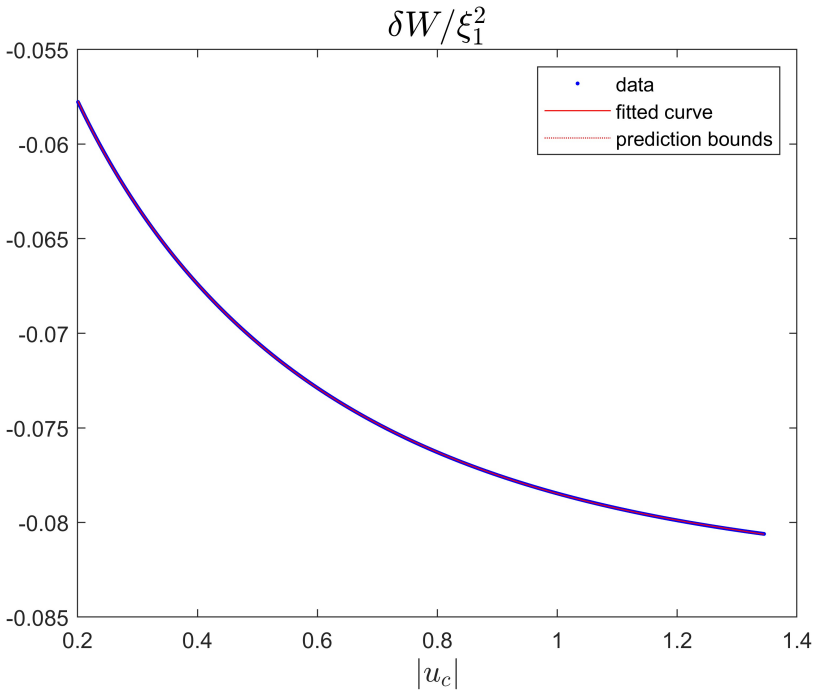

FIGURE 7.4: Curve fit for $e_0 = 0.05$

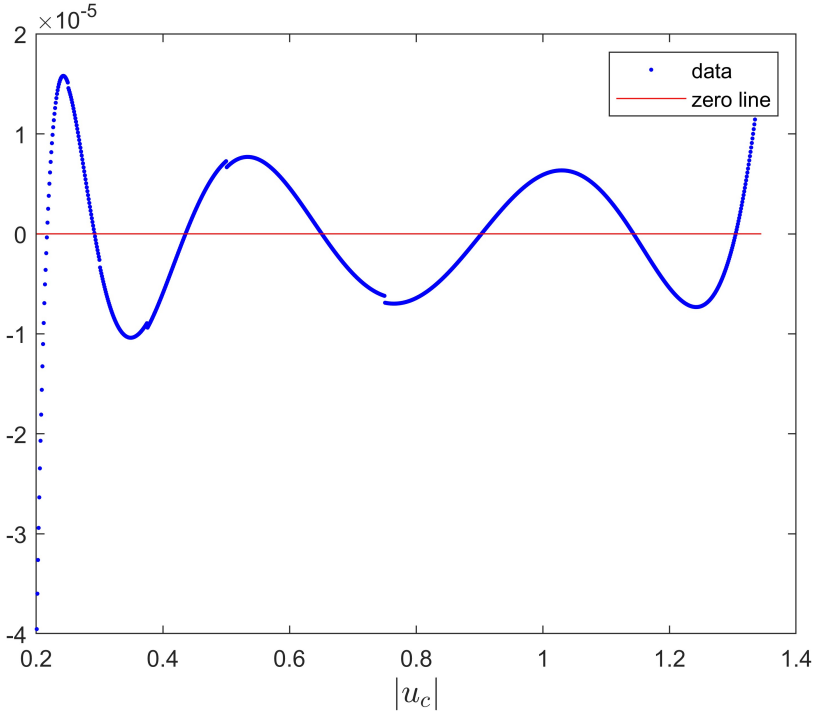

FIGURE 7.5: Residuals for $e_0 = 0.05$

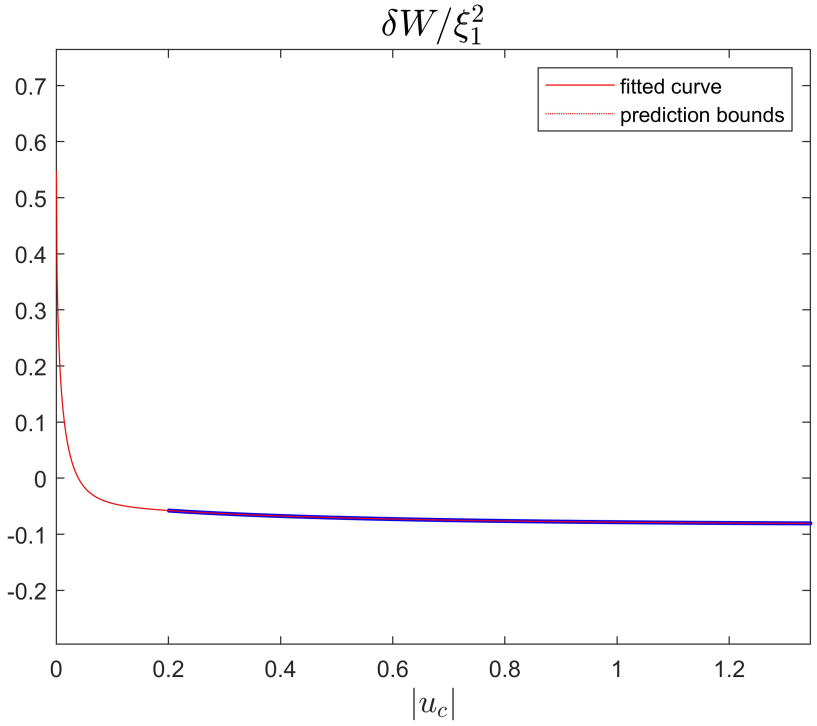

FIGURE 7.6: Extrapolated curve for $e_0 = 0.05$

Coefficients	Value (95% confidence bounds)
a	3.367 (3.363, 3.371)
b	-5.892 (-5.904, -5.88)
c	2.929 (2.917, 2.94)
d	-0.7163 (-0.7221, -0.7105)
e	0.2077 (0.2052, 0.2102)
f	-0.03141 (-0.0319, -0.03091)
h	0.05966 (0.05941, 0.05991)

TABLE 7.1: Model's coefficients for $e_0 = 0.05$

sse	4.9137e-08
rsquare	1.0000
adjrsquare	1.0000
rmse	6.5710e-06

TABLE 7.2: Curve fit evaluation parameters, $e_0 = 0.05$

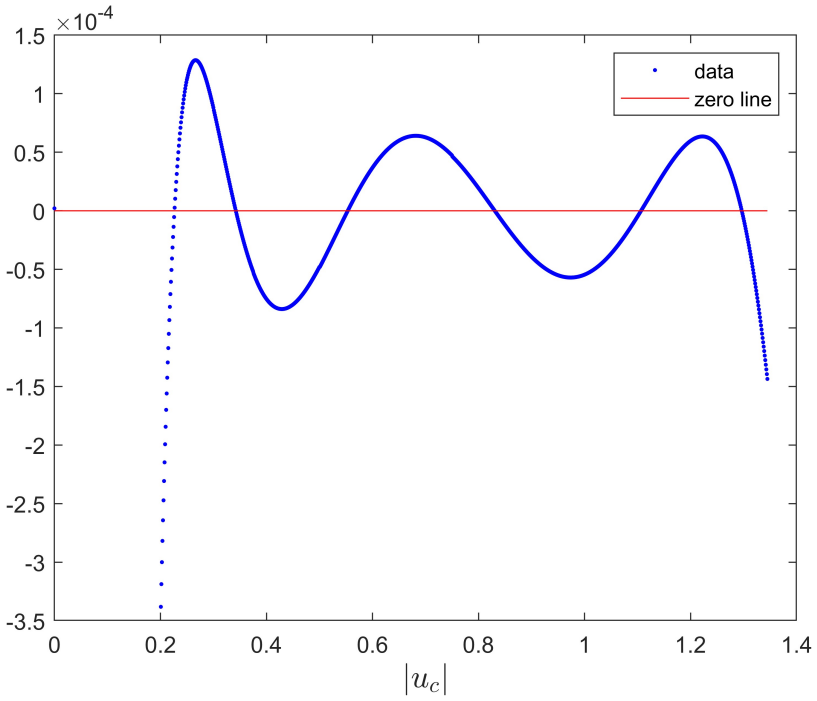

FIGURE 7.7: Residuals with the additional point, $e_0 = 0.05$

Coefficients	Value (95% confidence bounds)
a	1.887 (1.881, 1.892)
b	-2.193 (-2.198, -2.187)
c	-0.3652 (-0.3675, -0.3629)
d	0.6806 (0.674, 0.6872)
e	-0.3401 (-0.3449, -0.3353)
f	0.06968 (0.06841, 0.07095)
h	0.2006 (0.1995, 0.2016)

TABLE 7.3: Model's coefficients with additional point at the separatrix, $e_0 = 0.05$

Additional point at the separatrix

The graphs that follows are instead the second case scenario, i.e. produced considering inside the fitting data set the value of $\delta W/\xi_1^2$ at the separatrix (maintaining the same non linear model for the extrapolation).

Here the curve crosses the axis at around $|u_{marg}| \approx 0.047$. Considering the value obtained in previous scenario, i.e. $|u_{marg}| \approx 0.039$, the marginal stability surface is obtained in both cases for values that are very close one to each other. The same cannot be said for the value of the perturbed energy at the separatrix, as the two differs of $|\delta W/\xi_1^2| = 0.2682$. This discrepancy is not surprising if we consider the overall situation, i.e. we are dealing with a problem where a suitable truncation number m_{max} must be chosen in order to reduce the errors, and at the same time to not produce a too much large number of harmonic contributions. Also, the curve used for the extrapolation is not the correct analytic representation of the δW behavior, but only an approximated one, and must also be taken in consideration that we are missing an important range of points inside which the curve should have a significant slope increase.

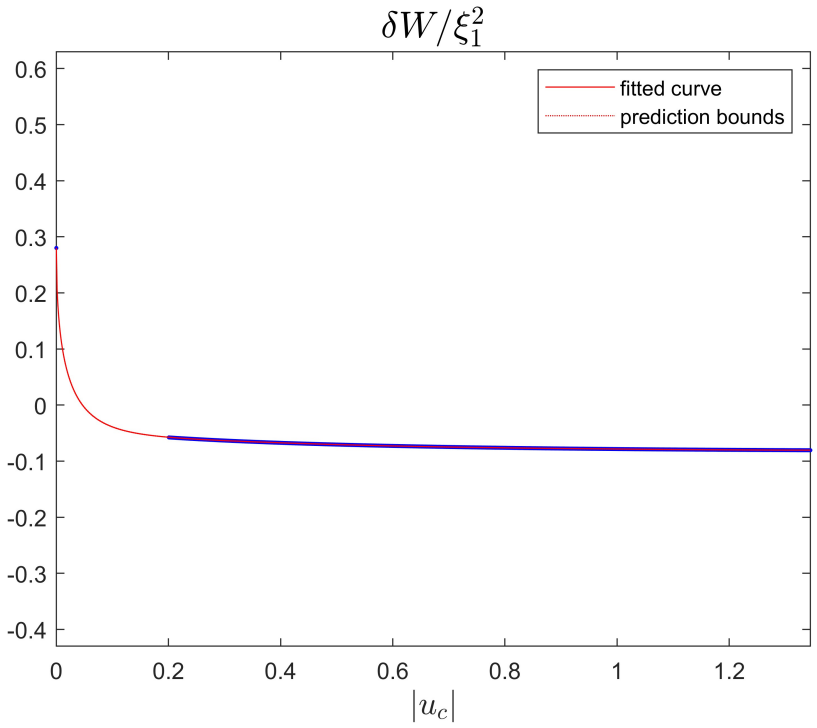

FIGURE 7.8: Fitted curve with additional point at the separatrix ($u = 0$), for $e_0 = 0.05$

sse	4.1991e-06
rsquare	1.0000
adjrsquare	1.0000
rmse	6.0718e-05

TABLE 7.4: Curve fit evaluation parameters with additional point at the separatrix, $e_0 = 0.05$

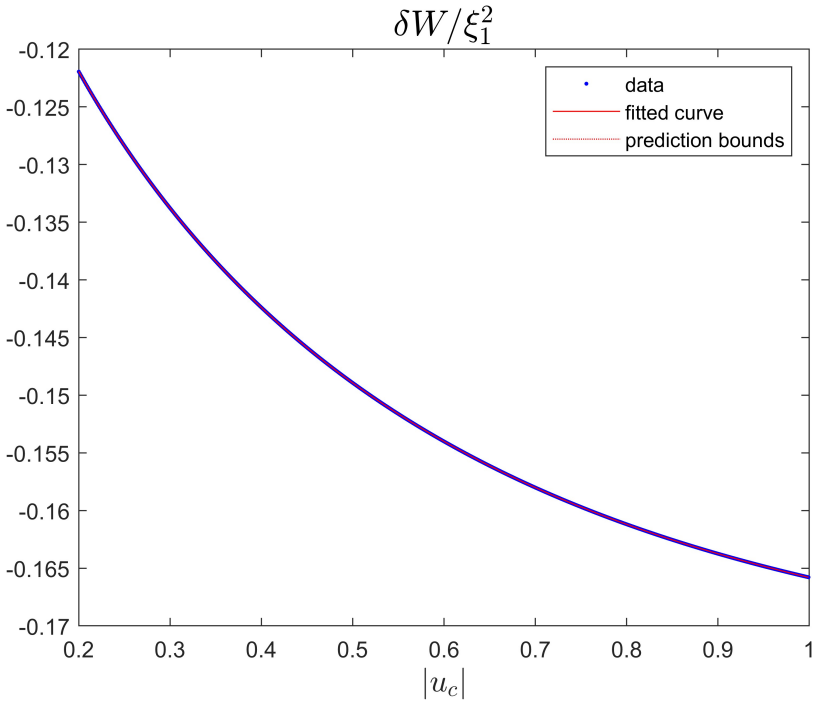

FIGURE 7.9: Curve fit for $e_0 = 0.1$

Coefficients	Value (95% confidence bounds)
a	3.512 (3.508, 3.517)
b	-6.522 (-6.535, -6.509)
c	3.526 (3.512, 3.54)
d	-1.028 (-1.036, -1.019)
e	0.3652 (0.3607, 0.3697)
f	-0.06899 (-0.0701, -0.06788)
h	-0.05045 (-0.05065, -0.05024)

TABLE 7.5: Model's coefficients , $e_0 = 0.1$

7.2.2 Case $e_0 = 0.1$

From table 6.7, the last suitable point that can be used for the fit is also $|u_c| = 0.2$.

Here the axis is crossed at around $|u_{marg}| \approx 0.022$ and the value of the relative perturbed energy at the separatrix is $\delta W_{(u_c=0)}/\xi_1^2 = 0.5256$. The value computed analytically is instead $\delta W_{(u_c=0)}/\xi_1^2 = 0.5627$.

sse	3.8001e-09
rsquare	1.0000
adjrsquare	1.0000
rmse	2.1891e-06

TABLE 7.6: Curve fit evaluation parameters, $e_0 = 0.1$

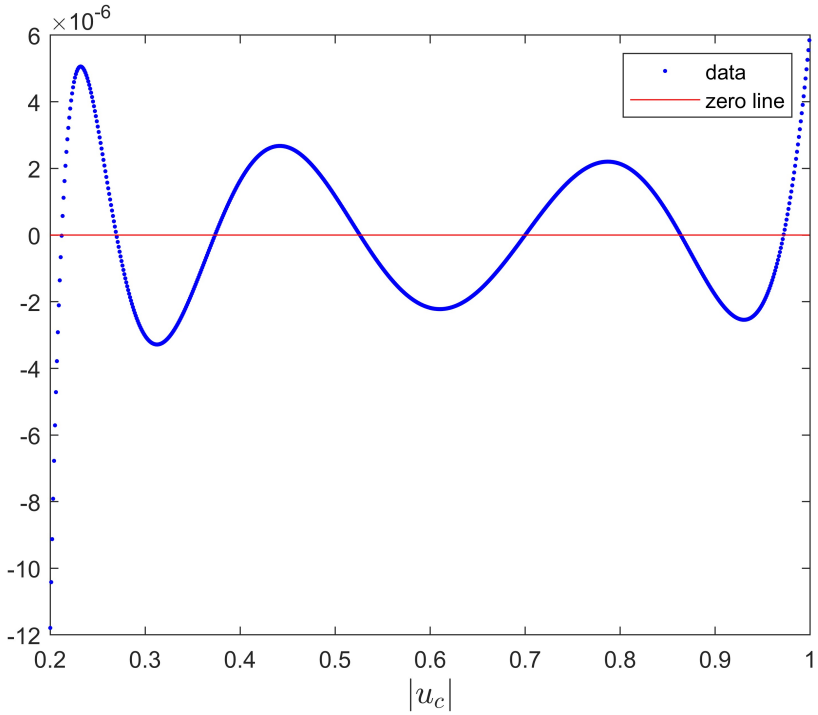

FIGURE 7.10: Residuals for $e_0 = 0.1$

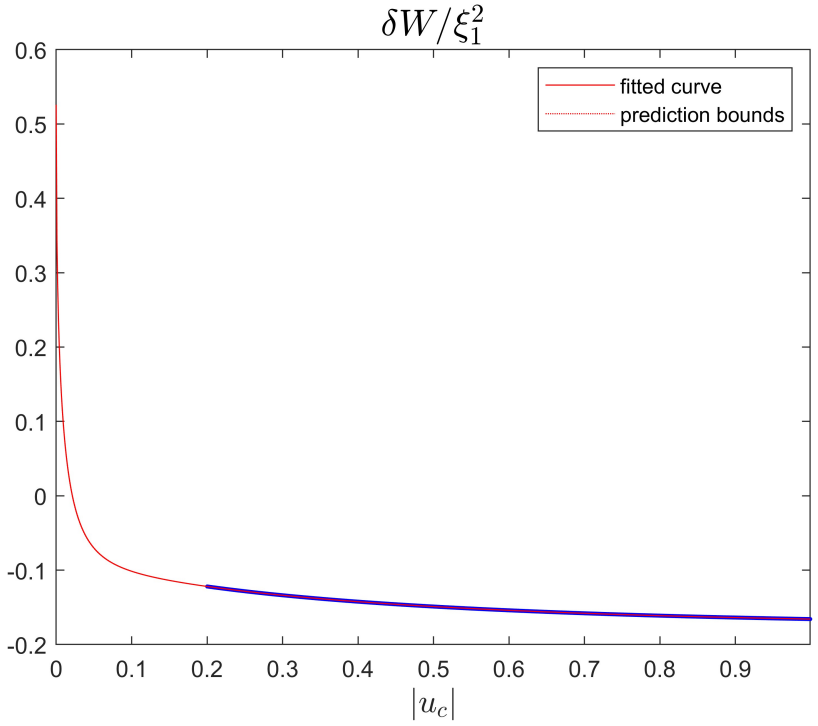

FIGURE 7.11: Extrapolated curve for $e_0 = 0.1$

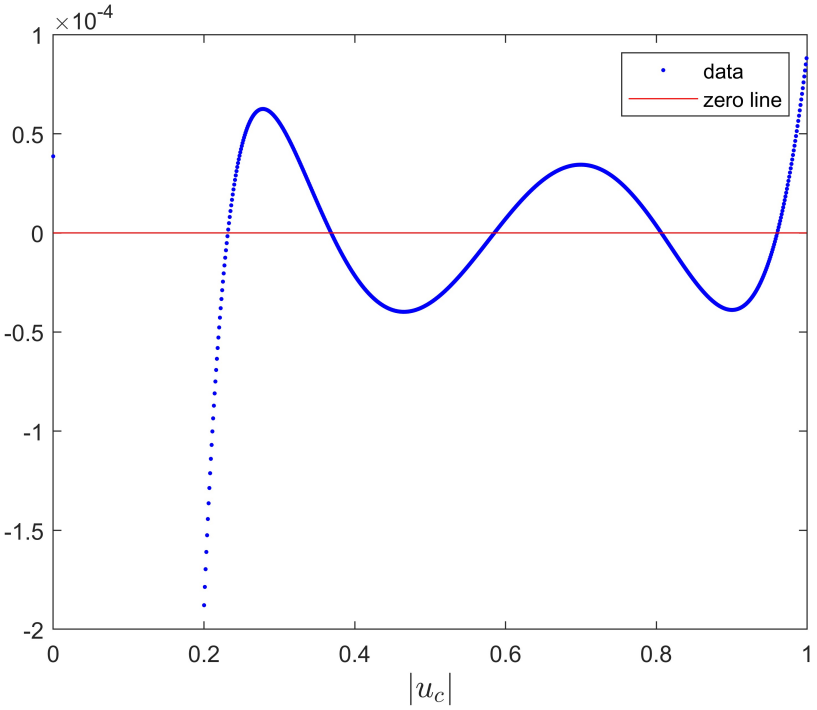

FIGURE 7.12: Residuals for $e_0 = 0.1$, additional point at the separatrix

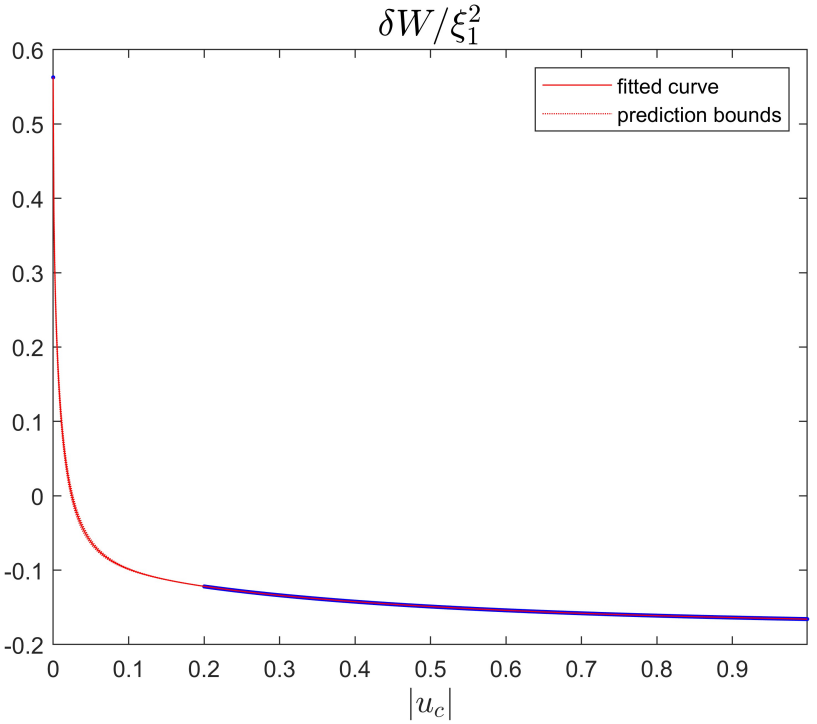

FIGURE 7.13: Fitted curve with the additional point at the separatrix ($u = 0$), for $e_0 = 0.1$

Coefficients	Value (95% confidence bounds)
a	3.533 (3.463, 3.602)
b	-6.666 (-6.885, -6.447)
c	3.777 (3.54, 4.013)
d	-1.292 (-1.432, -1.151)
e	0.5637 (0.4894, 0.638)
f	-0.1311 (-0.1494, -0.1128)
h	0.05131 (0.04773, 0.05489)

TABLE 7.7: Model's coefficients with additional point at the separatrix, $e_0 = 0.1$

sse	1.0747e-06
rsquare	1.0000
adjrsquare	1.0000
rmse	3.6790e-05

TABLE 7.8: Curve fit evaluation parameters with additional point at the separatrix, $e_0 = 0.1$

Additional point at the separatrix

In this scenario, the marginal stability surface can be located around $|u_{marg}| \approx 0.025$. Here both the values of the $|u_{marg}|$ and of $\delta W_{(u_c=0)}/\xi_1^2$ are very close for the two cases, while the fit evaluation parameters remain quite low. This type of non linear model, expression 7.1, seems more suitable for the case of $e_0 = 0.1$ w.r.t $e_0 = 0.05$.

7.3 Case $e_0 = 0.2$

No additional point at the separatrix

The marginal stability surface in this case is located at $|u_{marg}| \approx 0.0085$, while $\delta W_{(u_c=0)}/\xi_1^2 \simeq 0.4648$. For $e_0 = 0.2$ the value analytically computed at the separatrix is instead $\delta W_{(u_c=0)}/\xi_1^2 \simeq 1.1644$; so the two values, computed and extrapolated, differ a lot one from each other. Anyways, expression 7.1 is still a good model to represent our data set of points.

Coefficients	Value (95% confidence bounds)
a	3.685 (3.681, 3.689)
b	-7.559 (-7.573, -7.545)
c	4.542 (4.525, 4.559)
d	-1.663 (-1.676, -1.649)
e	0.7772 (0.7676, 0.7868)
f	-0.198 (-0.2012, -0.1948)
h	0.03994 (0.03978, 0.0401)

TABLE 7.9: Model's coefficients, $e_0 = 0.2$

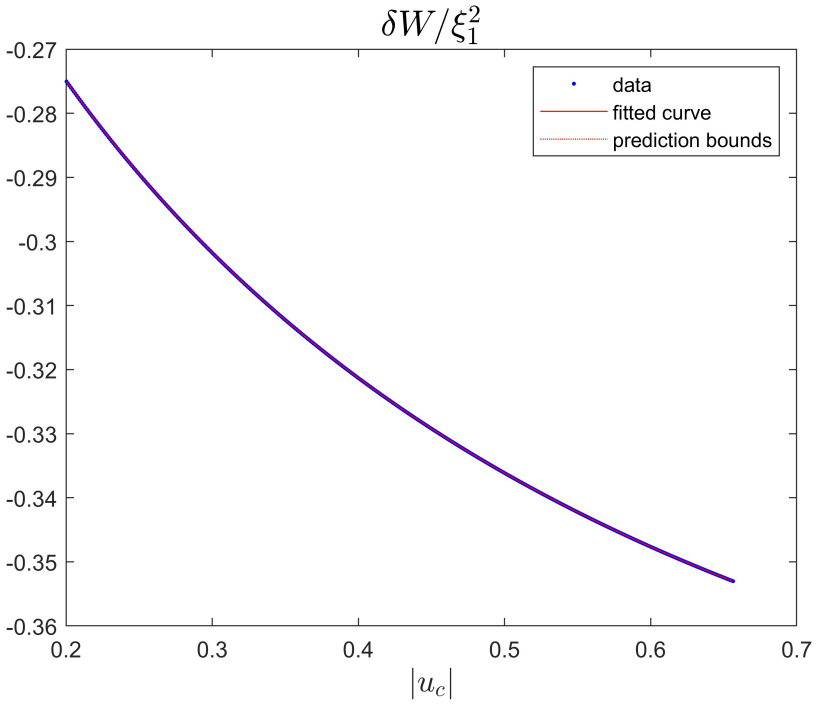

FIGURE 7.14: Curve fit, $e_0 = 0.2$

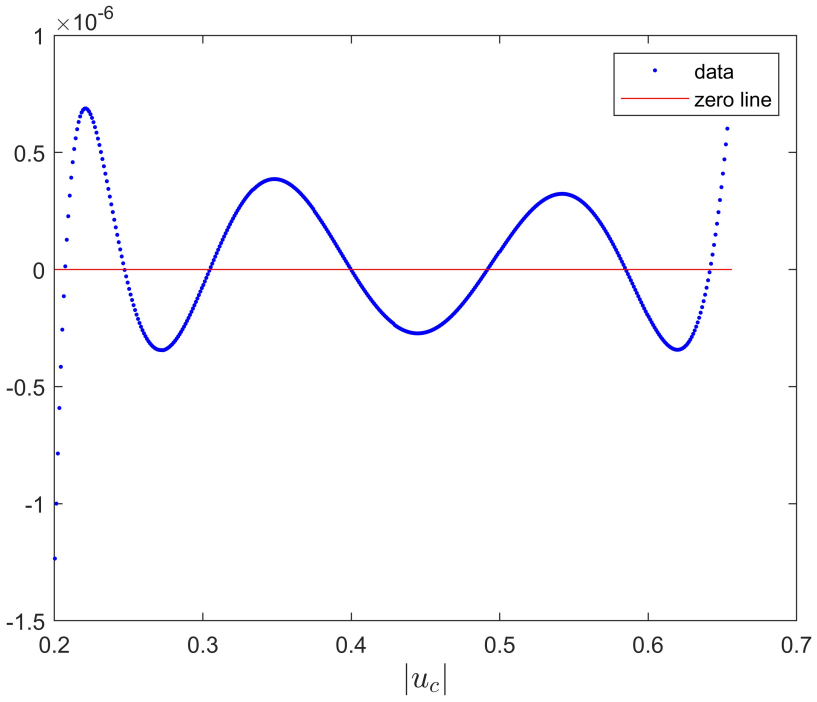

FIGURE 7.15: Residuals, $e_0 = 0.2$

sse	3.8097e-11
rsquare	1.0000
adjrsquare	1.000
rmse	2.9097e-07

TABLE 7.10: Curve fit evaluation parameters, $e_0 = 0.2$

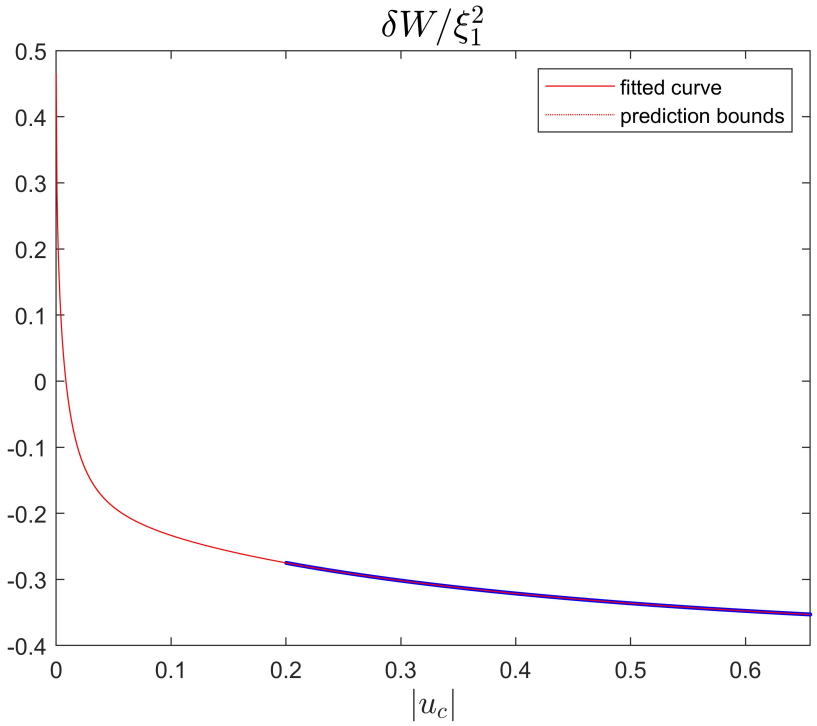

FIGURE 7.16: Extrapolated curve, $e_0 = 0.2$

Coefficients	Value (95% confidence bounds)
a	4.153 (-98.02, 106.3)
b	-10.08 (-362.5, 342.3)
c	8.695 (-412.9, 430.3)
d	-6.672 (-317.5, 304.2)
e	5.631 (-203.5, 214.8)
f	-2.236 (-68.95, 64.48)
h	0.0429 (-4.341, 4.426)

TABLE 7.11: Model's coefficients with additional point at the separatrix, $e_0 = 0.2$

Additional point at the separatrix

Considering instead the additional degree of freedom at $u_c = 0$, the final results become a disaster. Even if a curve can be obtained, the prediction bounds are extremely wide and the same happens with the residuals, see figures 7.17 and 7.18.

7.4 Conclusions

Before making the final considerations is better to briefly recap what has been done up to now. We have started from the problem of understanding stability of a magnetically confined plasma, for a divertor tokamak configuration with two X-points, that we recall are points on the magnetic field lines where the poloidal magnetic field component vanishes and so the final field is purely toroidal. The analysis is carried out in the regime of the reduced ideal-MHD model and in the low-β tokamak ordering. The focus is on VDEs (Vertical Displacement Events), in particular

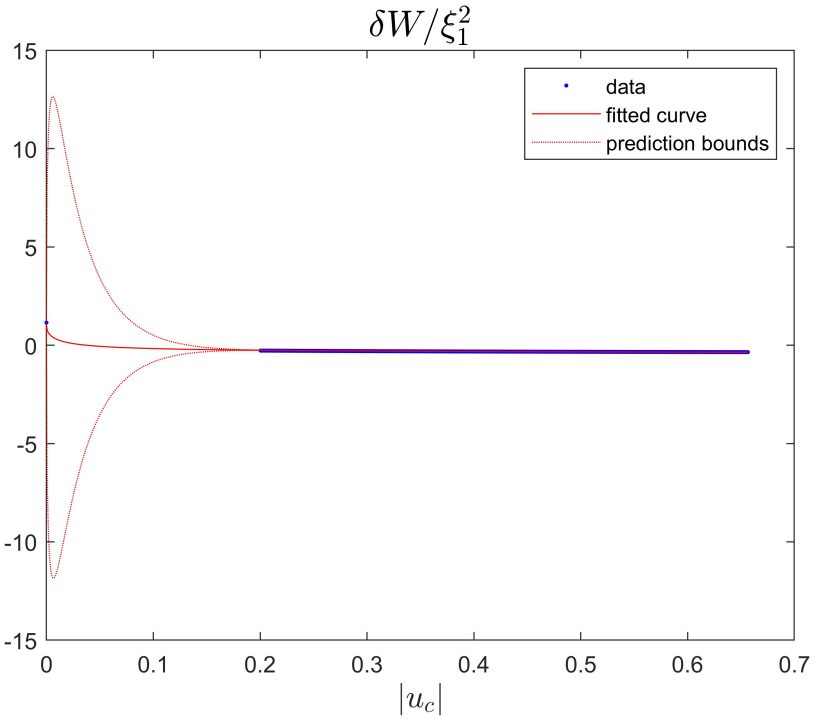

FIGURE 7.17: Curve fit with additional point at the separatrix, $e_0 = 0.2$

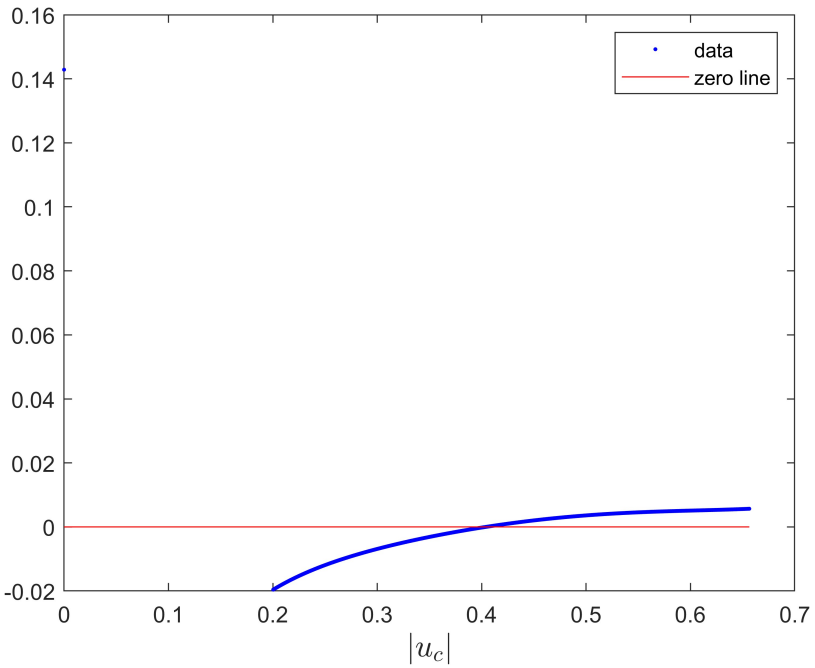

FIGURE 7.18: Residuals with additional point at the separatrix, $e_0 = 0.2$

sse	0.0427
rsquare	0.9820
adjrsquare	0.9818
rmse	0.0097

TABLE 7.12: Curve fit evaluation parameters with additional point at the separatrix, $e_0 = 0.2$

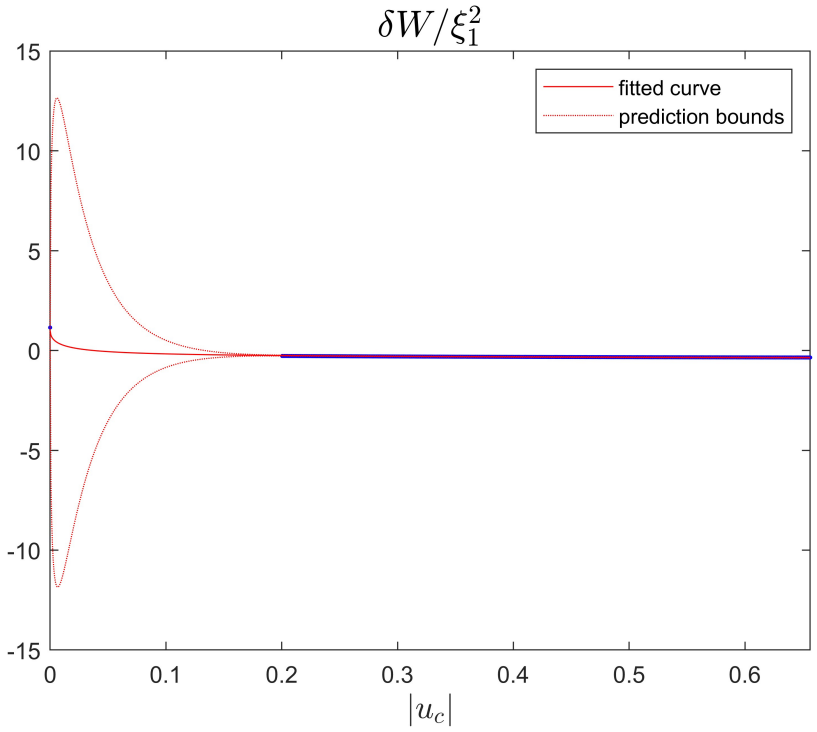

FIGURE 7.19: Extrapolated curve with additional point at the separatrix, $e_0 = 0.2$

the ones with $n = 0$, i.e. an axisymmetric, but not necessary rigid, vertical displacement, with n the toroidal mode number; also, it is possible to restrict the calculations only to a plasma section, as all the quantities that have been defined have toroidal symmetry. The most simple tool to describe how instability works is the heuristic model illustrated in chapter 4, from where has been shown the important result of the independence of the instability mechanism from the current profile, so, only the magnitude of the current carried by the plasma is important. With this conclusion is possible to setup the problem of describing a more realistic model in two different scenarios, where in the first one plasma is confined inside an elliptical flux surface, identified as $u = u_b$, located inside the magnetic separatrix. A current sheet always form at plasma boundary, this is analytically justified by a discontinuity in the first derivative of the perturbed flux function but has also been observed experimentally. The nature of this current sheet, in this first scenario, is responsible for the unstable behavior of the vertical displacement, thus plasma's oscillation grows exponentially in time, on a fast scale identified by the growth rate γ. When instead the plasma's edge is extended up to the magnetic separatrix, identified with the flux coordinate $u = u_X = 0$, the vertical displacement is resonant at the X points, i.e. it is constant along the toroidal field line passing through the X-points, regardless of its poloidal number. The nature of the current sheets is influenced by the harmonics of the perturbed solutions, which become more and more important for $u \to 0$, as has been shown in 5. At the separatrix, currents sheets act as a passive stabilization mechanism, thus changing the nature of the plasma column from unstable to stable.
Because of this change in the plasma behavior, it is reasonable to search the particular magnetic flux surface for which plasma is marginally stable, i.e. $\gamma^2 = 0$. By extending plasma up to a generic magnetic surface u_c, located between the elliptical surface and the separatrix, $|u_b| < |u_c| < |u_X|$, and considering a constant density profile that drops to zero at that specific surface, together with a constant current

density profile which instead drop to zero at $u = u_b$, we proceed to construct a curve of γ^2 as a function of u_c. To solve this problem we make use here of the important Energy Principle and of the variational formulation. The primer tells us that if $\delta W \geq 0$ than the plasma will result to be stable, while if negative, an unstable behavior will be present.
The computation of δW is not so straightforward. After the analytic expression is derived there is the need to compute the unknown coefficients g_n through the resolution of a linear system, that will result to be bad conditioned, i.e. the inversion of the matrix and as a result the final solution will carry an important error due to not unique solutions. One way to deal with this type of systems is to compute the Moore-Penrose inverse matrix, which allow us to find the solution which gives the lowest residual in two norm. This linear system is initially of infinite dimensions, as we are dealing with infinite series of terms summing over odd integers, but, the harmonics contribution goes to zero quite rapidly, thus allowing the truncation of the series and so the resolution of a linear system with dimension $(m_{max} + 1)/2$, as the harmonics contributions take only integer odd values of m, i.e. 1,3,5, and so on. There is an other consideration to take into account, the more harmonics we consider the more correct the series will be represented, but at the same time the linear system will result to be even more bad conditioned. We are then facing a problem of compromise for the right maximum value of m to choose for the series truncation. We have seen the errors produced by the choice of this m_{max}, and also the results that can be achieved.
For all the different cases and choices of m_{max}, we can obtain our δW curve and make the final consideration, i.e. that the searched marginal flux surface $(\delta W_{(u_c=u_{marg})} = 0)$ is too close to the origin w.r.t. the last point up to which we can perform calculations. The remaining tool that we have, in order to locate this marginal flux surface, is the extrapolation. It is somehow not so easy to find a function which describes the last part of a curve where an important change in behavior occurs. We have tried to describe this change of sign through a non linear model which is the combination of a polynomial and a logarithm.

$$\delta W_{(u_c,e_0)} = a_0 + a_{1/2}|u_c|^{1/2} + a_1|u_c| + a_2|u_c|^2 + a_3|u_c|^3 + a_4|u_c|^4 + \ln(|u_c| + h) \quad (7.2)$$

This choice is based on the assumption that there are no plausible physical reasons (known to us) which could justify a drop to more negative values or eventually some oscillatory behavior in the δW curve for $u_c \to 0$. The grade 4 is related to the fact that it provides the best results when analysing the fit evaluation parameters, and at the same time is the maximum grade which can be used in order to have results which make sense. Figure 7.19 is a perfect example of the type of disaster which can result from a bad choice. Furthermore, we have used 7.2 for the cases with $e_0 = 0.05$, $e_0 = 0.1$ and $e_0 = 0.2$, where the truncation value for the last two has been chosen as $6/|u_c|$, while for the primer $m_{max} = 3/|u_c|$. This type of non linear model has resulted to be suitable for all these three cases (not considering the analysis including the additional point at the separatrix), but some other considerations must be done. Firstly, for $e_0 = 0.05$ an additional grade for the polynomial, i.e. up to 5, could also be used, even if the final results are almost identical to what has been shown. We have illustrated the case with the grade 4 because for both $e_0 = 0.1$ and $e_0 = 0.2$ it is the maximum that can be taken in consideration, and since we wanted to have a unique model to compare the three cases this non linear function is the best to do it. A further information have been introduced for each of the listed cases, i.e. the additional point at the separatrix, which contribution has been analytically computed

e_0	u_{marg}
0.2	0.0085
0.1	0.015
0.05	0.039

TABLE 7.13: Marginal flux surface

in appendix E. It is important to specify that this last analysis must be considered very carefully, here is way. The reason behind this work was to locate the marginal flux surface, but at the same time there were some hopes to construct almost the totality the δW curve in order also to confirm, under this different approach, the result obtained for the case of the divertor tokamak scenario in [paper citation], i.e. the stability for a plasma which boundary is extended up to the separatrix. With all the considerations made until now is obvious to conclude that this is not something possible and we are forced to see things from an other prospective.
We take as correct the result of the positive δWvalue which gives us the indication of stability, and then we proceed to compare the curve obtained with and without the additional point at the separatrix, to at least understand if the two curves have some similar features and where the marginal stability surface would be located. For the first two e_0 case studies this approach brings to us interesting results, in particular for the value of u_{marg}, showing small discrepancies between the models with and without the additional point. For $e_0 = 0.2$ things become more complicated. If from one side we have a very good curve which perfectly fits our data, on the other hand, when the additional point is introduced the final results become tragic, leaving us with no so much information.
An other important argument is related to how the marginal surface moves with e_0. Table 7.13 that summarizes the results for different e_0s, is indicative of the fact that for larger ellipticity values the marginal flux surface u_{marg} is localized closer to $u_c = 0$; which is reasonable if we think that increasing e_0 means stretching more the plasma and so allowing the instability to be more difficulty driven.

We recall here table E.1, with the relative perturbed energy for different values of the ellipticity computed analytically:

e_0	$\delta W_{(u_c=0)} / \tilde{\zeta}_1^2$
0.2	1.1644
0.1	0.5258
0.05	0.28

TABLE 7.14: Values obtained from analytical calculations

If instead we look at the values obtained from the extrapolation (not considering obviously the additional value at the separatrix), we have:

e_0	$\delta W_{(u_c=0)} / \tilde{\zeta}_1^2$
0.2	0.4648
0.1	0.5101
0.05	0.5482

TABLE 7.15: Values obtained from extrapolated curve

We notice an important incongruence for the two different set of values of $\delta W_{(u_c=0)}/\xi_1^2$. The computed values increase with e_0 increasing, while the ones obtained from the extrapolation decrease with e_0 getting larger. One possible conclusion is that the range of points that we are missing in all the cases is quite important, so it may be that the extrapolated curve is correctly representing the function only locally, near the last points of the data set, while for values of u_c closer to zero the results could not be accurate at all.
We close our considerations by notice that the main problem of this analysis is the bad conditioned linear system, responsible of producing large errors for $u_c \to 0$. Different solutions have been tried in order to improve matrix Λ_m^n conditioning, without encouraging results; e.g. changing basis or iterative procedures to reduce the computational errors. One possible way to solve this problem is to reduce the dimension of the series. We have seen in chapter 5 that the harmonics contributions decrease very rapidly, as $\sim p/m^{3/2}e^{mu_c}$, but the series is very slow to converge. So, one possibility could be to use some multiplicative factor or an algorithm in order to speed up the convergence. We don't go further as nothing of this has been tried yet, and we will only result to be speculating.

Appendix A

Heaviside step function

The **Heaviside step function** is a piecewise function defined as

$$H_{(x)} = \begin{cases} 1 & , x \geq 0 \\ 0 & , x < 0 \end{cases} \tag{A.1}$$

and can be considered to be the integral of the Dirac delta function

$$H_{(x)} = \int_{-\infty}^{x} \delta(s)\, ds \tag{A.2}$$

Appendix B

Dirac delta function

The **Dirac delta function**, also known as the unit impulse, is a generalized function or distribution over the real numbers, whose value is zero everywhere except at zero, and whose integral over the entire real line is equal to one.
The Dirac delta function is the derivative of the Heaviside function

$$\delta(x) = \frac{d}{dx} H_{(x)} \tag{B.1}$$

Appendix C

First order Bessel function

Bessel functions are canonical solutions of Bessel's differential equation

$$x^2\frac{d^2y}{dx^2} + x\frac{dy}{dx} + (x^2 - \alpha^2)y = 0 \tag{C.1}$$

where for first order Bessel functions $\alpha = 1$. Their integral representation, also called Hansen-Bessel formula, is expressed as

$$J_n(x) = \frac{1}{\pi}\int_0^\pi \cos\left[n\tau - x\sin\left(\tau\right)\right] d\tau \tag{C.2}$$

being n a natural integer.

Appendix D

Moore-Penrose inverse

The **Moore–Penrose inverse** of a matrix is the most widely known generalization of the inverse of a matrix. The pseudoinverse of a matrix A is defined as a matrix $A^\dagger$, with dimensions $m \times n$, satisfying all of the following four criteria, known as the Moore–Penrose conditions:

- $AA^\dagger A = A$
- $A^\dagger AA^\dagger = A^\dagger$
- $(AA^\dagger)^* = AA^\dagger$
- $(A^\dagger A)^* = A^\dagger A$

The pseudoinverse can be expressed through the singular value decomposition (SVD). Any matrix can be decomposed as $A = UDV^*$, where U contains columns spanning the kernel of matrix A, while V contains columns spanning the null space of A. The diagonal positive real matrix D contains instead the singular values. The pseudoinverse can then be written as $A^\dagger = VD^{-1}U^*$.

Appendix E

Perturbed potential energy at the separatrix

The calculations that will follow have been provided by Adil Yolbarsop, which I here thank again for his time.
In order to compute the perturbed potential energy at the separatrix we can make use of the relation

$$\gamma^2 = \frac{\delta W}{\delta K} \tag{E.1}$$

where γ^2 is the one from 4.51, while the associated kinetic energy energy can be expressed as

$$\delta K = \xi^2 \rho \int_V d\nu \tag{E.2}$$

where V is the volume bounded by the magnetic separatrix. Since the area inside the separatrix is symmetric with respect to both x and y axis, is possible to evaluate the area in only the first quadrant and then multiply it by four, $\int d\nu = 4S$ (with S the area of the first quadrant.
Taking a ellipses confocal w.r.t. the separatrix, it is possible to evaluate the two areas S_1 and S_2 separately and then sum them up together as $S = S_1 + S_2$. The confocal ellipses parameter μ_1 can be obtained by solving through Matlab the following expression:

$$\mu_1 - 2\mu_b + \frac{e_0}{2}\sinh\left[2(\mu_1 - \mu_b)\right] + \frac{e_0}{2}\sinh\left(2\mu_b\right) = 0 \tag{E.3}$$

While the first area is computed with the formula for the area of a quarter of ellipses $S_1 = \pi A^2 \cosh\mu_1 \sinh\mu_1/4$. For the second one the integral which gives the area contribution is:

$$S_2 = \frac{A^2}{2}\int_{\mu_1}^{2\mu_b}\int_0^{\theta_{max}} \left[\cosh\left(2\mu\right) - \cos\left(2\theta\right)\right] d\mu\, d\theta \tag{E.4}$$

, where $\theta_{max}(\mu)$ is given by

$$\theta_{max} = \frac{1}{2}\arccos\left(\frac{\mu - 2\mu_b + e_0/2\sinh\left(2\mu_b\right)}{e_0/2\sinh\left[2(\mu - \mu_b)\right]}\right) \tag{E.5}$$

Thus, the final expression for the relative perturbed energy in dimensionless form is

$$\frac{\delta W}{\xi_1^2} = 2\left(\frac{a^2 + b^2}{a^2 b^2}e_0\right)^2 (S_1 + S_2) \tag{E.6}$$

Here below is shown a table with some values as function the ellipticity parameter e_0.

e_0	$\delta W / \xi_1^2$
0.2	1.1644
0.1	0.5627
0.05	0.280

TABLE E.1: Relative perturbed potential energy for $u = 0$

Bibliography

[1] Milton Abramowitz and Irene A Stegun. *Handbook of mathematical functions with formulas, graphs, and mathematical tables*, volume 55. US Government printing office, 1948.

[2] George B Arfken, Hans J Weber, and Frank E Harris. *Mathematical methods for physicists: a comprehensive guide*. Academic press, 2011.

[3] Claudio Chiuderi and Marco Velli. *Fisica del Plasma: Fondamenti e applicazioni astrofisiche*. Springer Science & Business Media, 2012.

[4] Jeffrey P Freidberg. *ideal MHD*. Cambridge University Press, 2014.

[5] Ryszard Gajewski. Magnetohydrodynamic Equilibrium of an Elliptical Plasma Cylinder. *The Physics of Fluids*, 15(1):70–74, 01 1972.

[6] G. Laval, R. Pellat, and J. S. Soule. Hydromagnetic stability of a current-carrying pinch with noncircular cross section. *The Physics of Fluids*, 17(4):835–845, 04 1974.

[7] F Porcelli, A Yolbarsop, T Barberis, and R Fitzpatrick. Resonant axisymmetric modes. *Journal of Physics: Conference Series*, 1785(1):012004, feb 2021.

[8] Franco Porcelli and Adil Yolbarsop. Analytic equilibrium of "straight tokamak" plasma bounded by a magnetic separatrix. *Physics of Plasmas*, 26(5):054501, 05 2019.

[9] Franco Porcelli and Adil Yolbarsop. Analytic equilibrium of "straight tokamak" plasma bounded by a magnetic separatrix. *Physics of Plasmas*, 26(5):054501, 05 2019.

[10] H. R. Strauss. Nonlinear, three-dimensional magnetohydrodynamics of noncircular tokamaks. *The Physics of Fluids*, 19(1):134–140, 01 1976.

[11] A. Yolbarsop, F. Porcelli, and R. Fitzpatrick. Impact of magnetic x-points on the vertical stability of tokamak plasmas. *Nuclear Fusion*, 61(11):114003, oct 2021.

[12] A Yolbarsop, F Porcelli, Wandong Liu, and R Fitzpatrick. Analytic theory of ideal-mhd vertical displacements in tokamak plasmas. *Plasma Physics and Controlled Fusion*, 64(10):105002, aug 2022.